Robust Bode Methods
for Feedback Controller Design
of Uncertain Systems

Jonathan D. Taylor

M.S. Mechanical Engineering, Carnegie Mellon University

M.S and B.S. Physics, Clemson University

B.S. Mechanical Engineering, Clemson University

Carnegie Mellon University

Pittsburgh, PA

August, 2014

This work is dedicated to the memory of my mother and father,

Barbara and Donald Taylor.

-JD

Acknowledgments

I would like to express my utmost gratitude to my advisor, Bill Messner, from whom I have learned so much and whose patience and generosity have been unending. I would like to thank Katie Cattrell for her unwavering support and love, without which none of this would have been possible. I would also like to thank Takenori Atsumi for allowing me to build upon his ideas for robust Bode control, and Iacopo Gentilini for his kind assistance when life's circumstances kept me away from the lab. I would like to thank the Office of Naval Research for their support of this work (Grant #N0001409C0125). Finally, I would like to thank each member of my thesis committee listed below.

Thesis Committee

William Messner (chair)

Bruno Sinopoli

Philip LeDuc

Daniel Opila

Abstract

In this work, we introduce several novel approaches to feedback controller design, known collectively as the "Robust Bode" methods, which adapt classical control principles to a modern robust control (H_∞) framework. These methods, based on specially modified Bode diagrams extend familiar frequency-domain controller design techniques to linear and nonlinear, single–input/single–output (SISO) and multi–input/multi–output (MIMO) systems with parametric and/or unstructured uncertainties. In particular, we introduce the Contoured Robust Controller Bode (CRCBode) plots which show contours (level-sets) of a robust metric on the Bode magnitude and phase plots of the controller. An iterative loop shaping design procedure is then employed in an attempt to eliminate all intersections of the controller frequency response with certain forbidden regions indicating that a robust stability and performance criteria is satisfied.

For SISO systems a robust stability and performance criterion is derived using Nyquist arguments leading to the robust metric used in the construction of the CRCBode plots. For open-loop unstable systems and for non-minimum phase systems the Youla parametrization of all internally stabilizing controllers is used to develop an alternative Robust Bode method (QBode). The Youla parametrization requires the introduction of state-space methods for coprime factorization, and these methods lead naturally to an elegant connection between linear-quadratic Gaussian (LQG) optimal control theory and Robust Bode loop-shaping controller design. Finally, the Robust Bode approach is extended to MIMO systems. Utilizing a matrix norm based robustness metric on the MIMO CRCBode plots allows cross-coupling between all input/output channels to be immediately assessed and accounted for during the design process, making sequential MIMO loop-shaping controller design feasible.

Contents

List of Figures

Chapter 1

Introduction to Robust Bode Methods

1.1 Overview

Control systems are *robust* if they maintain satisfactory stability and performance characteristics in the presence of uncertainty. This uncertainty is unavoidable in any real system and may arise from several sources. For example, mathematical models of physical systems are always inaccurate due to parameter variations, neglected (typically higher-order) dynamics, linearizations, discretizations, and so forth. Also only certain stochastic properties of the *exogenous* inputs to the system are typically known, for instance the expected power spectral density of the noise and disturbance signals [1].

Classical frequency-domain controllers, designed using standard techniques on the Bode, Nyquist, and root-locus diagrams, often exhibit good robustness properties. In fact, a common classical design objective is to maximize the gain and phase margins which represent direct (though simplistic) measures of the robust stability of the closed-loop system. Optimal control approaches, e.g. linear-quadratic-Gaussian (LQG), on the other hand, have been shown in certain cases to be extremely sensitive to model uncertainty [2].

The robustness concerns of time-domain optimal control theory motivated the development of modern H_∞ robust control, and classical single–input/single–output (SISO) control served as the prototype. In particular, the frequency-domain input-output (transfer function) representations fundamental to classical control suggested that the H_∞-norm, representing the maximum "system gain" in any direction, is the relevant metric to consider in multi–input/multi–output (MIMO)

robust control [3]. Using this H_∞ formalism along with the generalized MIMO Nyquist stability theorem, it is possible to define robust stability margins for general uncertain systems which may then be optimized to recover the desirable robustness properties from classical control.

Classical design and analysis techniques are graphical and can be carried out manually using relatively basic design principles. These principles generalize naturally to an H_∞ robust control framework [4,5]. For example, increasing the minimum singular value at low frequencies, relative to the open-loop 0 dB crossover (i.e. minimizing the H_∞-norm of the sensitivity function) is required to improve disturbance rejection and tracking performance, while reducing the maximum singular value at high frequencies (i.e. minimizing the H_∞-norm of the complementary sensitivity function) is necessary to limit the effect of measurement noise and improve stability margins.

1.2   Contributions

In this thesis, several new graphical techniques for robust feedback controller design are introduced known collectively as the "Robust Bode" methods. These approaches combine the advantages of classical loop-shaping feedback controller design on the Bode plots with the formalism of H_∞ robust control theory. As we shall show, Robust Bode methods are both powerful and intuitive and can be applied to a wide variety of different systems: linear or nonlinear, SISO or MIMO, with unstructured and/or parametric uncertainties. Additionally, certain difficulties arising in other control design methods are elegantly resolved by the Robust Bode approach.

Modern H_∞ robust control leverages numerical controller synthesis routines. These algorithmic methods are appealing since they eliminate the traditional trial-and-error design process and generate an optimal controller automatically; however, they also have a number of significant disadvantages. Synthesis algorithms tend to generate controllers which are more complicated (higher-order) than necessary. If a lower-order controller is desired then some order reduction techniques must be applied which can have adverse effects. Also standard synthesis algorithms typically do not generate controllers of fixed structure, e.g. proportional-integral-derivative (PID). Both of these issues are of course resolved when the control law is directly specified by the designer, as in the Robust Bode approach. Other desirable features such as pure integral action and steeper high-frequency roll-off rate (improved noise rejection) which can be difficult to accomplish using automated synthesis algorithms are relatively easy to include in a manual design approach.

Automated approaches also obscure the design process and make it more difficult for an experienced designer to affect a desired outcome. For example, in H_∞ robust control, weighting functions are selected to represent the uncertainty and performance requirements of the system. If these weights are too large, the automated synthesis routines will fail. Unfortunately, it is often not clear how exactly to adjust these weights to resolve these issues. The Robust Bode plots, on the other hand, display the robust metrics explicitly as a function of frequency, so any infeasible regions may be directly assessed and corrected.

Synthesis algorithms also impose additional analytic constraints on the problem. For instance in standard H_∞ robust control, the plant and weighting functions must be proper rational transfer functions matrices, with only the plant possibly open-loop unstable. In cases where the plant model is not representable by a rational transfer function, e.g. nonlinear or time-delayed systems, or in cases when a mathematical model is not readily available, these requirements are cumbersome, requiring the designer to perform several preliminary approximation steps. The Robust Bode methods, on the other hand, only require the frequency response (magnitude and phase) of the plant and weighting functions at a discrete set of frequencies (and operating points in the case of nonlinearities); therefore, Robust Bode methods are especially well suited to "data–driven" design problems in which only empirical frequency response data is available.

Also, as we shall see in subsequent chapters, weighting functions chosen to satisfy typical performance criteria, e.g. zero steady-state error for a step disturbance, are themselves not stable and/or proper. In these cases, the designer must also perform some preliminary "artificial" modifications to the weighting functions so that the automated algorithms will proceed. Robust Bode methods do not share these same constraints, and therefore are can be more straightforward to apply.

Though the Robust Bode methods share many commonalities with classical Bode based controller design methods, there are some very important distinctions. The standard Bode plot and associated stability criteria are given in terms of the "loop transfer function", $L = PK$, i.e. the product of the plant, $P(s)$, and controller, $K(s)$, transfer functions. Often, however, we are interested in designing a single controller for a set of plants, which may result from parametric variations (e.g. HDD benchmark problem [6,7]) or to linearized dynamics of a nonlinear plant about a set of operating points (e.g. case study in Section 2.7). In constructing the Robust Bode plots a robust metric is computed for each member of the uncertain plant set, but only the largest or worst-case

value at each frequency is displayed along with the controller frequency response. In this way, parametric (structured) and unstructured uncertainties are included in a way which is transparent to the control engineer, and loop-shaping is even more straight-forward than traditional Bode design, since the function being "shaped" is displayed directly.

Standard Bode approaches are typically applicable only to single–input/single–output systems. Most attempts to extend classical techniques to multi–input/multi–output systems have failed due to the inability to evaluate and account for cross-coupling in the input/output channels; however, the robust metric displayed on the Robust Bode diagrams is based on a H_∞ matrix norm, and consequently the effects of changes in any channel are immediately apparent in all channels, making manual MIMO design feasible, as explored in Chapter 3.

Classical Bode plots are also best suited to open-loop stable and minimum phase systems, i.e systems with all poles and zeros in the left half-plane. In unstable and/or non-minimum phase systems, the gain and phase margins can be ambiguous and stability difficult to ascertain. The Robust Bode approach, however, is quite versatile and can be modified slightly to facilitate the design of the so called Youla parameter which avoids these difficulties, as discussed at length in Chapter 4. Finally, we note that unlike standard Bode design which can be vague regarding necessary gains, the incorporation of the weighting functions in the Robust Bode approach allows one to identify exactly when specific performance requirements have been achieved in the presence of explicit parametric and unstructured uncertainty bounds.

1.3   Robust Control History and Loop-Shaping Literature

The foundations of classical frequency-domain control theory were laid by Harry Nyquist in his 1932 paper *Regeneration Theory* in which his eponymous stability theorem was proven, [8], and by Hendrik Wade Bode in 1945 book *Network Analysis and Feedback Amplifier Design*, in which he introduced what would come to be known "Bode plots" for controller design and analysis [9].

These early frequency-domain results were essential to many technological advances of the era. However, in the 1960's, problems associated primarily with the "space-race" motivated the development of an alternative state-space formulation of linear systems and control theory focused on solving time-domain optimization problems. Optimal control required numerical linear programming algorithms and so advanced in parallel with the digital computers of the day, eventually

becoming the *de facto* standard in the field of controls. State-space methods were seen as the only viable option for multivariable control systems, and indeed they were very successful at solving the critical aerospace problems of the time.

However, as attempts were made to apply optimal control techniques elsewhere, specifically in the chemical processing industry in which accurate dynamic models of the plant were rarely available, it became apparent that state-space based methods alone were insufficient. Classical controllers, in particular the proportional-integral-derivative (PID) controller, on the other hand, were quite effective in these applications.

During this period, a few researchers, notably Rosenbrock and Macfarlane in the UK and Horowitz in the Israel, committed to formalizing the frequency-domain theory and extending the loop-shaping design techniques to more complicated problems. The majority of the academic controls community remained skeptical. They regarded frequency-domain methods as obsolete and inherently unsuitable for multi–input/multi–output (MIMO) systems [10].

John Doyle (1978) showed by counter-example that linear-quadratic Gaussian (LQG) controllers, the cornerstone of optimal control theory, have no guaranteed robustness margins [11][1]. This result finally motivated a coordinated effort in the controls community to develop a formal approach to robust control. Zames (1981) was influential in this regard, by discovering that the H_∞ matrix-norm was the relevant metric to minimize in order to optimize the robustness of the feedback system. This may be interpreted as minimizing the the worst-case disturbance amplification the closed-loop system over all frequencies, i.e. the closed-loop sensitivity functions. By contrast, LQG minimizes the average performance over all frequencies [12]. Eventually, several impressive solutions to the H_∞ minimization problem were discovered, of note are the Glover-Doyle (1989) algorithm which requires the iterative solution of 2 Algebraic Riccati Equations (ARE) [13] and the linear matrix inequality (LMI) approach (1994) [14,15]. Though the H_∞ problem is formulated in the frequency-domain, efficient solutions are derived in terms of time-domain state-space realizations. This complementary viewpoint remains the dominant paradigm in modern linear systems and control theory, in some sense justifying the early work of those researchers who dared to take an unconventional path.

---

[1]The title of Doyle's paper "Guaranteed margins for LQG regulators" and the abstract "There are none." are somewhat legendary in the controls community.

The "Robust Bode" approaches developed in this thesis are most closely aligned with a body of work in control theory referred to as "robust loop-shaping". Over the years, several approaches to robust loop-shaping have been proposed in the literature. Quantitative Feedback Theory (QFT) introduced by Horowitz [16] displays uncertainty "templates" on the Nichols chart that must be avoided during the design process; however, QFT loop-shaping is complicated by the fact that frequency is an implicit variable on the Nichols chart. Macfarlane and Glover [5] proposed an alternative multi-stage robust loop-shaping method applicable to unstable MIMO systems. The desired open-loop shape is initially obtained via pre and post-compensation of the plant, $W_2 P W_1$, followed by a standard H_∞ synthesis to obtain a stabilizing controller K_∞, and finally the overall controller is obtained from $K = W_1 K_\infty W_2$. Doyle, et al. [17] present a robust loop-shaping approach which is similar to classical SISO loop-shaping, and apply it directly to several different system parametrizations: the loop gain L, the controller C, and the Youla parameter Q. In these approaches, specific low and high-frequency bounds are first formulated in terms of the performance and uncertainty requirements of the system. These bounds are then displayed on the singular value plots of the system[2], and compensator transfer functions are selected to satisfy these bounds. This method is also pursued by, Skogestad [18], and others. These various techniques have also been compiled into a few specialized books, including Braatz's *Robust Loopshaping for Process Control* (1993) [19] and Feyel's *Loop-Shaping Robust Control* (2013) [20].

1.4 Chapter Summary

In Chapter 2, the "Robust Bode" controller design approach for single–input/single–output (SISO) systems is introduced. A robust stability and performance criteria is derived and used to construct the so-called Contoured Robust Controller Bode (CRCBode) plots, a characteristic example of which is shown in Fig. 2.3.

The loop-shaping design procedure using the CRCBode plots is first demonstrated by considering a proportional-integral-derivative (PID) controller tuning example for a 2nd order mass-spring-damper system that must meet specific performance objectives in the presence of explicit parametric and unstructured uncertainties. A detailed case study is then presented in which a flow-rate controller for a nonlinear butterfly valve based liquid cooling system is designed. In this

---

[2]For SISO systems, the singular value and Bode magnitude plots are equivalent.

example, the CRCBode approach to structured uncertainties is presented. The performance of the resulting controller is verified in an experimental test-bed and compared to an automatically synthesized robust H_∞ controller. Finally, an interesting three–dimensional interpretation of the Robust Bode plots is discussed.

In Chapter 3, several important results are derived concerning the robust stability of general MIMO systems. In particular the generalized Nyquist stability theorem is derived, which is then used to derive the small-gain and structured singular value stability theorems. These results form the basis of standard H_∞ control theory, and though readily available in the literature, are presented in a concise manner for completeness, since they are used in developing the more advanced Robust Bode methods of later chapters.

In Chapter 4, the Robust Bode methods are applied to open-loop unstable and non-minimum phase SISO systems. The algebraic and analytical constraints limiting achievable performance in these systems are reviewed. A simple non-minimum phase example is presented, and the Youla parametrization of all internally stabilizing controllers for non-minimum phase systems is introduced. A new Robust Bode method based on loop-shaping the Youla parameter, $Q(s)$, directly is then explored, QBode. Unstable plants are considered next, the Youla parametrization of which requires the introduction of state-space methods for coprime factorization. These methods lead naturally to an elegant connection between linear-quadratic Gaussian (LQG) optimal control theory and Robust Bode loop-shaping controller design. This connection is pursued by conducting an in depth case study of an inverted pendulum system.

Finally in Chapter 5, the Robust Bode approach is extended to nonlinear multi–input/multi–ouput (MIMO) systems. As with SISO systems, MIMO CRCBode plots facilitate an iterative loop-shaping controller design process, but in this case, there are several input/output pair loops which must be tuned independently. Previous similar approaches to this "sequential loop tuning" approach were not particularly successful since cross-coupling between the input/output channels was not accurately represented in the standard Bode or Nyquist (eigenvalue loci) diagrams [10]. However, the new MIMO CRCBode approach overcomes these limitations by displaying contours of a closed-loop matrix norm based robustness metric, Γ_{MIMO}. As a result, any cross-coupling (which is reduced in an initial decoupling step) is immediately visible as changes in the "forbidden regions" of all channels simultaneously, which may be directly accounted for in the manual loop-shaping design process.

Chapter 2

SISO Robust Bode Methods and CRCBode Plots

2.1 Introduction

Classical controller design techniques, using for instance the root-locus, Bode, Nyquist, and Nichols plots, despite being developed nearly a century ago, remain essential to both the pedagogy and practice of modern controls engineering. These classical methods are primarily graphical and require manual interaction by the designer. This generally leads to a more thorough and intuitive understanding of the system and to simpler "minimal-order" controllers, relative to the state-space "optimal" control solutions available, e.g. linear-quadratic Gaussian (LQG) control. The simplicity of the controllers, however, is in no way indicative of poor performance. In fact, it is exactly this simplicity which belies classical control's most important asset: Robustness.

Robustness is the ability of a system to maintain adequate stability and performance in the presence of the inevitable uncertainty present in the system. The sources of this uncertainty are wide and varied, including unknown disturbance and noise signals, uncertain or time-varying model parameters, or unmodeled nonlinear or high-frequency dynamics. It has long been recognized that the basic principles of classical control tend to yield controllers with good robustness properties. In fact, the common classical design objectives of gain and phase margin are direct (though simplistic) measures of system robustness.

Optimal control algorithms tend to over-emphasize the model by selecting a higher-order (at

least equal to the plant) controller which "inverts" the system dynamics, and as a result, they often exhibit poor performance when the model is uncertain. Classical approaches, on the other hand, do not typically exhibit this behavior since the minimal-order structure of the controller can not "over-fit" the model.

Classical control strategies remain a strong viable option for many control problems; however, they are not without their limitations. Standard "loop-shaping" Bode design approaches were developed primarily for single–input/single–ouput (SISO) systems, e.g. motor speed control, but they have traditionally proven difficult to extend to more complicated systems, for example unstable, non-minimum phase, or multi–input/multi–ouput (MIMO) systems. Also classical techniques are not well suited to the problem of meeting *specific* robust stability and performance objectives without some trial-and-error. In these more complicated situations, some automated optimal or robust H_∞ control strategy is almost always adopted; however, this does not have to be the case. As we shall see, it is possible to modify or augment the Bode plots of the system in various ways to address all of these apparent limitations. In particular, by deriving explicit conditions for the robust stability and performance of the system in terms of the controller, it is possible to place bounds on the Bode magnitude and phase plots which guide manual loop-shaping controller design and indicate when certain robustness objectives have been reached.

In this chapter, we will introduce the "Robust Bode" controller design methodology for single–input/single–ouput (SISO) systems. First, we will derive robust stability and performance criteria for SISO systems with unstructured uncertainties. We then define a robust performance metric based on this criteria and use it to construct the so-called Contoured Robust Controller Bode (CRCBode) plots. We proceed in demonstrating the use of these CRCBode plots, by first examining the problem of tuning a PID controller for a 2$^{\mathrm{nd}}$ order mass-spring-damper system that must meet specific performance objectives in the presence of explicit parametric and unstructured uncertainties. We then delve into a detailed case study in which a flow-rate controller for a nonlinear butterfly valve based liquid cooling system is designed using CRCBode techniques. In this example, the CRCBode approach to structured uncertainties is presented, to account specifically for the linearizations of the nonlinear plant. The performance of the resulting controller is then verified in an experimental test-bed and compared to an automatically synthesized robust controller. Finally, we explore an interesting three–dimensional interpretation of the Robust Bode plots which clarifies certain aspects of these new methods.

2.2 Uncertainty Representation

In order to analyze a system's robustness, it is first necessary to identify a mathematical representation of the system uncertainty. For now, we will consider systems with only *unstructured uncertainty*, arising for instance due to unknown noise sources or unmodeled (usually high-frequency) dynamics. Unstructured uncertainties are represented by frequency-dependent complex valued (due to the phase uncertainty) norm-bounded perturbations, $\Delta(j\omega)$. These perturbations are typically normalized via frequency-dependent weighting functions such that, $\|W\Delta\|_\infty < 1$.

For analytical reasons, the uncertain perturbations and weighting functions should be represented by stable transfer functions[1]. This is not restrictive, however, since the perturbations may be introduced into the system model in various configurations, e.g. additive, inverse multiplicative, etc. [12]. Here, we consider an *output multiplicative* uncertainty description, as shown in Fig. 2.1 and (2.1), which is appropriate if the uncertainty does not affect the open-loop stability of the plant, i.e. does not change the number of right half-plane poles.

$$P(j\omega) = (1 + \Delta(j\omega))P_0(j\omega) \tag{2.1}$$

where $P(j\omega)$ is the actual (perturbed) plant frequency response, $P_0(j\omega)$ is the modeled (nominal) plant frequency response, and $\Delta(j\omega)$ is the norm-bounded unstructured multiplicative perturbation.
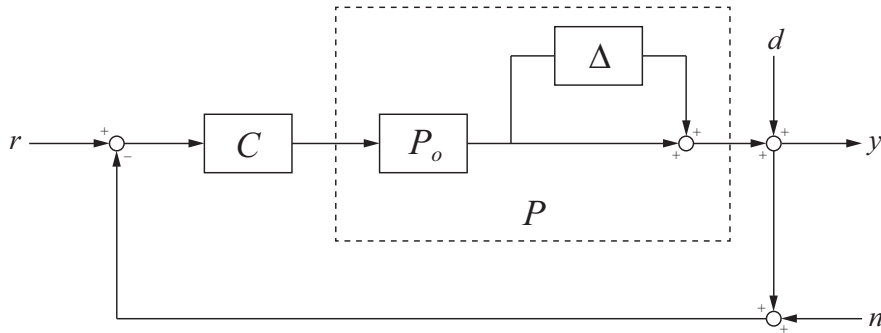
Figure 2.1: Block diagram representing an uncertain feedback system. P_0 is the nominal model, Δ is the output unstructured multiplicative uncertainty, and C is a robust controller.

---

[1]Robust Bode methods do not require rational uncertainty models.

2.3 SISO Robust Stability and Performance Criteria

We proceed in deriving criteria for the robust stability and robust performance of the system presented Fig. 2.1. For this, we will make extensive use of the Nyquist diagrams provided in Fig. 2.2, in which the blue curves are the nominal loop frequency response, $L_0 = P_0 C$, and the circles with radii $|W_1|$ and $|W_3 L_0|$ are known as the performance and uncertainty discs respectively.
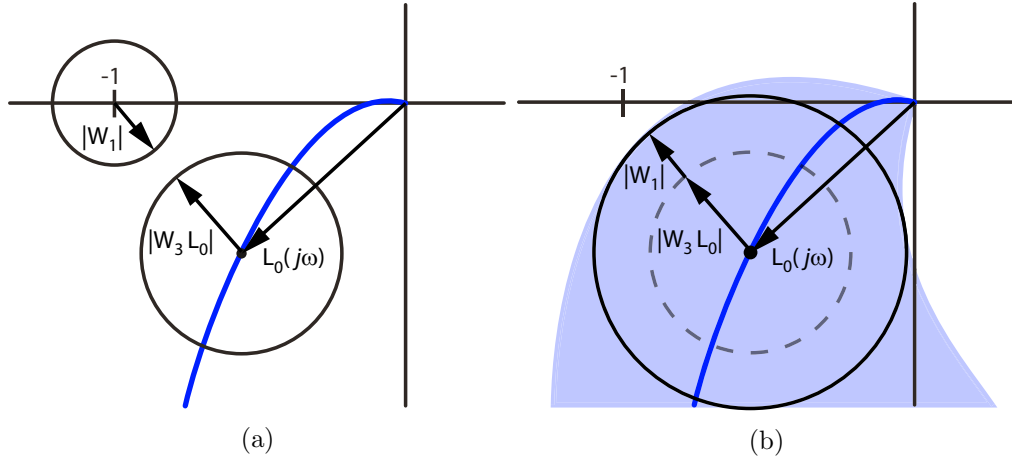
Figure 2.2: (a) The robust criterion, Eq. (2.6), is satisfied if at *each frequency* the uncertainty disc centered at L_n with radius $|W_3 L_n|$ does not intersect the performance disc with radius $|W_1|$ centered at the critical point -1 on the Nyquist diagram. (b) An equivalent alternative interpretation with uncertainty disc expanded by $|W_1|$ defining region over *all frequencies* which should not intersect the critical point -1.

The sensitivity and complementary sensitivity functions are defined in the usual way in terms of the loop transfer function $L = PC$, Eq. (2.2). The nominal sensitivity functions, S_0 and T_0 are obtained by replacing P with P_0.

$$S = \frac{1}{1+L} = \frac{1}{1+PC} \qquad T = \frac{L}{1+L} = \frac{PC}{1+PC} \tag{2.2}$$

2.3.1 Robust Stability

The Nyquist stability theorem states that a SISO system is stable only if the loop frequency-response, $L = PC$, encircles the -1 point on the Nyquist diagram exactly N_p times counter-clockwise as s traverses the Nyquist $\mathcal{D}$ contour[2], where N_p is the number of open-loop unstable (closed right half-plane) poles of the plant.

---

[2]A path traveling up the imaginary axis from $-j\infty$ to $+j\infty$, possibly avoiding any poles on the imaginary axis by displacing the path into right half-plane, and connected by a semi-circular arc with radius $r \to \infty$.

If the magnitude of the uncertain perturbation, $\Delta(j\omega)$, is upper bounded by the weighting function, $W_3(j\omega)$, that is if $|\Delta(j\omega)| \leq |W_3(j\omega)|$, then the perturbed plant, $P(j\omega)$, is contained in the *uncertainty disc* centered at $P_0(j\omega)$ with radius $|W_3(j\omega)P_0(j\omega)|$, as seen in Fig. 2.2.

Robust stability is achieved if for every member of the uncertainty set, $\{P : |P/P_0 - 1| \leq |W_3|\}$, the closed-loop system is stable. The uncertainty set obviously includes the nominal plant, P_0, therefore robust stability requires that the nominal system first be stabilized by some controller, C, so that the nominal loop $L_0 = P_0C$ has exactly N_p counter-clockwise encirclements of the -1 point on the Nyquist diagrams. Robust stability is then achieved if and only if no uncertain perturbation changes the number of encirclements. Graphically this condition states that the unstructured uncertainty disc centered at the nominal open-loop frequency response, L_0, with radius $|W_3L_0|$ must not intersect the critical -1 point on the Nyquist diagram at any frequency, because otherwise there would exist at least one plant in the uncertainty set that destabilizes the closed-loop system.

The distance from the nominal frequency response to the -1 point is $|L_0(j\omega) - (-1)|$. Therefore, for robust stability, the radius of the uncertainty disc must be less than this distance at all frequencies, $|W_3(j\omega)L_0(j\omega)| < |1 + L_0(j\omega)| \ \forall \ \omega$. This result is typically restated in terms of the nominal complementary sensitivity function, $T_0 = L_0(1 + L_0)^{-1}$, (2.3).

$$|W_3(j\omega)T_0(j\omega)| < 1 \quad \forall \quad \omega \tag{2.3}$$

2.3.2 Robust Performance

The performance of a system (e.g. disturbance rejection, bandwidth, etc.) may be characterized by the magnitude of its sensitivity function as a function of frequency, and thus a wide variety of different performance objectives may be put in the following standard form, Eq. (2.4).

$$|W_1(j\omega)S(j\omega)| < 1 \quad \forall \quad \omega \tag{2.4}$$

For instance, if the error should have magnitude $e < \epsilon$ for a unit sinusoidal disturbance at frequency ω, then the weighting function $|W_1(j\omega)| > 1/\epsilon$. More generally, if the desired sensitivity function is known, then the performance weighting function should be chosen such that $|W_1(j\omega)| > |S(j\omega)|^{-1}$ for all ω. If all members of the uncertainty set satisfy Eq. (2.4), then the system exhibits

robust performance. To determine this condition, we substitute the perturbed model, Eq. (2.1), into Eq. (2.4):

$$|W_1 S| = \left| \frac{W_1}{1 + (1 + \Delta)L_0} \right| = \left| \frac{W_1 S_0}{1 + \Delta T_0} \right| < \frac{|W_1 S_0|}{|1 - W_3 T_0|} \qquad (2.5)$$

Therefore the following condition on the nominal sensitivities, $|W_1 S_0|/|1 - W_3 T_0| < 1$, is required for robust performance of all plants in the uncertainty set, $|W_1 S| < 1$. Rearranging, we obtain the standard form of the robust performance condition, (2.6).

$$|W_1(j\omega)S_0(j\omega)| + |W_3(j\omega)T_0(j\omega)| < 1 \quad \forall \quad \omega \qquad (2.6)$$

From this result, we note that if a system exhibits robust performance then it must also be robustly stable ($|W_1 S_0| + |W_3 T_0| < 1 \Rightarrow |W_3 T_0| < 1$), or equivalently robust stability is necessary for robust performance.

2.3.3 Graphical Interpretation

The standard graphical interpretation of the robust performance criterion, (2.6), is that at each frequency the uncertainty disc must not intersect with the performance disc centered at the critical point -1 with radius $|W_1|$, Fig. 2.2a. An equivalent alternative interpretation is that the (shaded) region containing the uncertainty discs expanded by $|W_1|$ at all frequencies must not intersect the point -1 as shown in Fig. 2.2b. This latter approach may be more useful since it combines information at all frequencies into a single graph.

2.4 SISO Robust Metric

Robust performance, (2.6), implies ($\Rightarrow$) robust stability, (2.3). Therefore, to ensure that the closed-loop system is both robustly stable and exhibits robust performance, we need only verify the inequality in (2.6) holds at all frequencies. To this end, we define the SISO robust performance metric, $\Gamma_{\text{SISO}}(\omega)$, as in (2.7), equal to the left hand side of (2.6).

$$\Gamma_{\text{SISO}}(\omega) \overset{\text{def}}{=} |W_1(\omega)S_0(\omega)| + |W_2(\omega)T_0(\omega)| \qquad (2.7)$$

Clearly then, the robust stability and performance criteria, (2.6), is satisfied if and only if (2.8) holds at all frequencies.

$$\Gamma_{\text{SISO}}(\omega) < 1 \ \forall \ \omega \quad \Leftrightarrow \quad \text{(robust stability and performance)} \qquad (2.8)$$

2.5 Contoured Robust Controller Bode Plots

Contoured Robust Controller Bode (CRCBode) plots show contours (level sets) of the robust stability and performance metric, $\Gamma_{\text{SISO}}(\omega)$, (2.7) on the Bode magnitude and phase plots of the controller. A characteristic CRCBode plot is provided in Fig. 2.3, cf. Section 2.6.
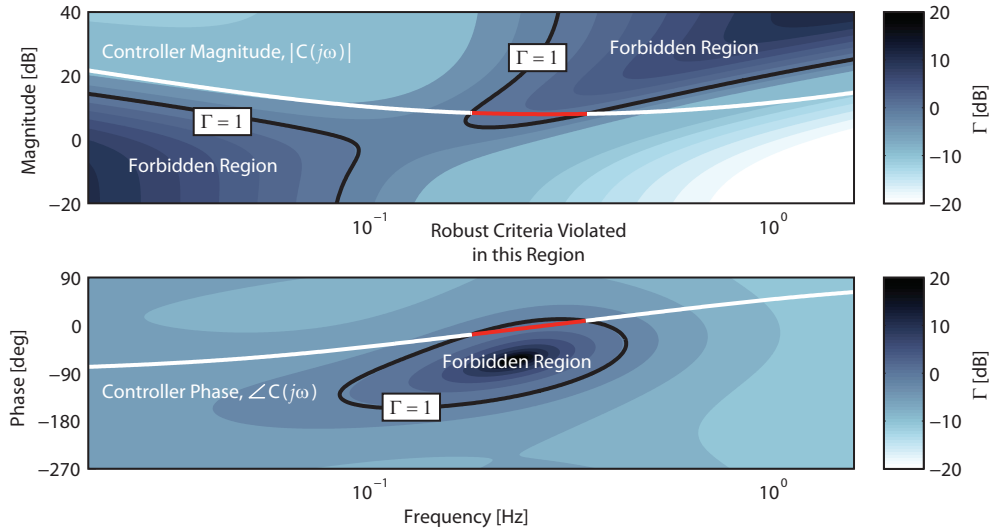
Figure 2.3: Example CRCBode Plot for a 2nd order system (K_{DC}=1, ζ=0.8, ω_n=1 rad/s) with weighting functions $W_1 = (10s + 1000)/(2000s + 100)$ and $W_2 = (0.3s + 0.18)/(0.006s + 0.6)$ and PID controller (K_P=2.5, K_I=1.5, K_D=0.5). The robust performance condition, Eq. (2.6), is violated over the frequency range ($0.18 - 0.35$ Hz) as indicated by the intersections (shown in red) of the controller frequency response with the forbidden regions $\Gamma \geq 1$. Any intersections are always consistent (i.e. occur over the same frequency range) on both the CRCBode magnitude and phase plots. For this problem, all intersections can be avoided by changing the controller parameters to (K_P=1.5, K_I=1.0, K_D=0.5) – not shown.

If the controller frequency response, $C(j\omega)$, does not intersect the so-called "forbidden regions", defined by ($\Gamma_{\text{SISO}}(\omega) \geq 1$), at any frequency, then the robust stability and performance criteria is satisfied, (2.6). Also lower values of $\Gamma_{\text{SISO}}(\omega)$ correspond to increased system robustness, and higher contour density indicate regions more sensitive to system perturbations.

Visualizing the Γ_{SISO} contours on the CRCBode plots allows the designer to manually and approximately optimize the system robustness (i.e. minimize the $H_\infty-$ norm of the closed-loop system) using an iterative loop-shaping controller design procedure. CRCBode plots provide the same low and high frequency design boundaries as other robust loop-shaping approaches [5] but additionally provide guidance in the 0 dB cross-over region determining system stability. In this "CRCBode approach", the designer also has the freedom to directly apply other improvements to the compensator (for instance higher roll-off rate) without necessarily altering the weighting functions as is necessary in automated H_∞ synthesis methods.

Also, unlike automated synthesis routines, the CRCBode approach *does not* require realizable transfer function representations of either the plant or weighting functions, a fact indicated in (2.7) by the use ω instead of $j\omega$. Thus the CRCBode approach is extremely well suited to systems in which only empirical frequency-response data is available at a finite set of frequencies and systems not represented by rational transfer functions (e.g. time delay).

2.5.1 CRCBode Approach to Structured Uncertainty

The formulation of the robust stability and performance criteria, (2.6), assumed that the uncertainty was completely unstructured, i.e. only gain information was available. For nonlinear systems or systems with uncertain or time varying parameters, unstructured uncertainty bounds are usually excessively conservative. It is advantageous in these cases to consider the uncertainty as a structured set of plants which have both gain and phase information at each frequency. For instance, the structured set can be distinct physical plants with parameter variations (e.g. the HDD benchmark problem [6, 7]) or the linearized dynamics of a nonlinear plant about a set of operating points (e.g. the butterfly valve system presented in the case study in Section 2.7).

The CRCBode plot is well suited to the design of a single controller which is robust over a structured set of plants since the bounds are on the controller, C, instead of the open-loop frequency response, $L = PC$. For any finite structured uncertainty set $\{P_n(\omega) : P_n \in \mathcal{P}_N, n = 1, ..., N\}$, we may simply evaluate the robust metric of the controller, C, and each member of the set independently, $\Gamma_{\text{SISO}}(C, P_n; \omega)$, displaying only the maximum over all plants when constructing the CRCBode plot for the system. Then, if the controller frequency response, $C(j\omega)$, remains within the allowed region, $\max_n(\Gamma_{\text{SISO}}(C, P_n; \omega)) < 1$ at all frequencies, then the robust stability and performance criteria, (2.6), is satisfied for all uncertain plants in the set.

15

In some cases, the variation of the structured set may be too large, and the CRCBode plot generated using the above procedure yields bounds which cannot be satisfied by a single controller. In these cases, we can either relax the performance requirements (i.e. alter the weighting functions) or apply additional pre-compensation, G. The role of G is to "collapse" the frequency responses of the structured set, for instance using the nominal inverse of the plant model. This operation requires knowledge of the current operating point, and may thus be considered a gain scheduled controller [21]. Now if the CRCBode plot of the single controller C is always in the allowed region, $\max_n(\Gamma_{\text{SISO}}(C, GP_n; \omega)) < 1$ then the combined controller CG is robust over the entire set of plants.

Since each member of the structured uncertainty set is included explicitly in the CRCBode plot, the multiplicative uncertainty weighting function, W_3, need only be large enough to account for the discrete sampling of the plant set, measurement errors (sensor accuracy), and noise. This approach results in a less conservative design (i.e. smaller forbidden regions) than if a larger unstructured uncertainty weighting function is chosen to account for the variation of all the structured plants about a single nominal model [22].

2.5.2 Constructing CRCBode Plots

CRCBode plots are constructed in the following way: *CRCBode Magnitude:* Fix the controller phase and for each plant evaluate $\Gamma(\omega)$ over a range of controller magnitudes. *CRCBode Phase:* Fix the controller magnitude and for each plant evaluate $\Gamma(\omega)$ over a range of controller phases. Plot contours of the maximum Γ over all plants along with the controller frequency response.

Algorithm $CRCBode(\bar{\omega}, \{P_n\}, \tilde{C}, W_1, W_3)$

Input: Vector of test frequencies: $\bar{\omega}$, Set of nominal (possibly pre-compensated) plant frequency response vectors (magnitude and phase): $\{P_n(\bar{\omega}) : P_n \in \mathcal{P}_N, n = 1, ..., N\}$, Proposed controller frequency response vector (magnitude and phase): $\tilde{C}(\bar{\omega})$, Weighting function vectors (magnitude): $W_1(\bar{\omega})$ and $W_3(\bar{\omega})$.

Output: CRCBode plot of system.

1. **Define:** Controller magnitude and phase test vectors, $|\bar{C}|$ and $\angle\bar{C}$ (Sets limits and resolution of ordinate axes)

2. **for each** $P_n \in \mathcal{P}_N$

3.   **for each** $\omega_i \in \bar{\omega}$

4.   **for each** $|C_j| \in |\bar{C}|$

5.   **Evaluate:** $\Gamma_{\text{mag}}[n](|C_j|\angle\tilde{C}(\omega_i), P_n(\omega_i), W_1(\omega_i), W_3(\omega_i))$ from Eq. (2.7) using proposed controller phase and each test controller magnitude.

6.   **for each** $\angle C_j \in \angle \bar{C}$

7.   **Evaluate:** $\Gamma_{\text{phase}}[n](|\tilde{C}(\omega_i)|\angle C_j, P_n(\omega_i), W_1(\omega_i), W_3(\omega_i))$ from Eq. (2.7) using proposed controller magnitude and each test controller phase.

8. **CRCBode Magnitude:** Contour plot of $20\log(\max_n(\Gamma_{\text{mag}}))$ [dB] and overlay proposed controller magnitude response, $|\tilde{C}(\bar{\omega})|$ [dB]

9. **CRCBode Phase:** Contour plot of $20\log(\max_n(\Gamma_{\text{phase}}))$ [dB] and overlay proposed controller phase response, $\angle \tilde{C}(\bar{\omega})$ [deg]

2.6   CRCBode Controller Design: PID Tuning Example

We now explore how the CRCBode approach may be used to tune a robust proportional-integral-derivative (PID) controller for the stable 2nd–order mass-spring-damper system shown in Fig. 2.4 with transfer function given in (2.9).
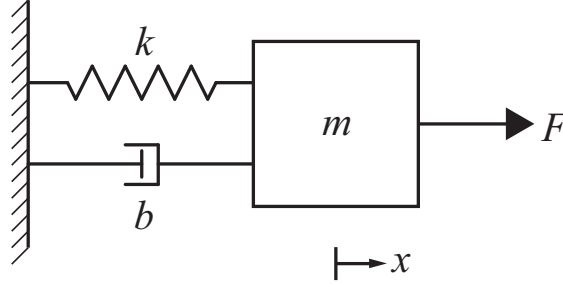
Figure 2.4: Schematic of mass-spring-damper system.

The nominal parameters of the system are: $m_0 = 1$ [kg], $b_0 = 1.6$ [N/m/s], $k_0 = 1$ [N/m] corresponding to a DC gain: $K_{DC,0} = 1$, damping ratio: $\zeta_0 = 0.8$, and undamped natural frequency: $\omega_{n,0} = 1$ [rad/s].

$$P(s) = \frac{X(s)}{F(s)} = \frac{K_{DC}\,\omega_n^2}{s^2 + 2\zeta\omega_n s + \omega_n^2} = \frac{1}{ms^2 + bs + k} = \frac{1}{s^2 + 1.6s + 1} \tag{2.9}$$

Performance Specifications

We are interested in finding a robust controller which achieves the following closed-loop performance specifications:

(1) Maximum sensitivity, $S_{\max} = 10$ [dB] – Max disturbance amplification

(2) Loop bandwidth, $\omega_b = 2$ [rad/s] – Frequency at which $T = -3$ [dB]

(3) Zero steady-state error for a step disturbance – System type $= 1$

(4) High-frequency roll-off rate $= 2 \times 20$ [dB/dec]

Performance Weighting Function Selection

The performance weighting function, $W_1(\omega)$, should be selected to correspond roughly to the inverse of the desired closed-loop sensitivity, which we see from the robust performance condition, $|W_1 S| < 1 \Leftrightarrow |W_1| < |S^{-1}|$. A simple formula to aid in the selection of the performance weighting functions is provided in (4.6), which includes a number of pure integrators equal to the desired system type. The parameters of this formula are determined using performance specifications (1)-(3).

$$W_1(s) = S_{\max}^{-1} \left(\frac{s + \omega_b}{s} \right)^{\text{sys type}} = \frac{0.316(s + 2)}{s} \tag{2.10}$$

Note that performance weighting functions in the form of (4.6) can not be used directly with numerical H_∞ synthesis routines since they are unstable due to the poles at $s = 0$. They are typically made stable by shifting the poles slightly into the left half-plane; however, this results in controllers which do not have the pure integral action necessary for zero steady-state error. The manual Robust Bode approaches do not have these same analytical constraints, and so (4.6) is perfectly acceptable.

Uncertainty Specifications

In order for the controller to be robust, it must ensure closed-system stability and meet the stated performance objectives in the presence of the following parametric and unstructured uncertainties:

(1) $\pm 10\%$ uncertainty in the mass: $m = m_0(1 \pm 0.1)$

(2) $\pm 50\%$ uncertainty in the damping: $b = b_0(1 \pm 0.5)$

(3) $\pm 20\%$ uncertainty in the stiffness: $k = k_0(1 \pm 0.2)$

(4) Gaussian white measurement noise – zero mean with standard deviation, $\sigma = 0.01$

Fig. 2.5 shows the plant frequency response with the nominal parameters (blue curve), and several responses corresponding to different random samples of the uncertain plant parameters with wide-band (white) Gaussian noise added, ($\mu = 0, \sigma = 0.01$) (light gray curves).

The uncertain damping factor is immediately apparent from Fig. 2.5. Also, it is clear how the relative error increases with frequency despite the noise signal having a constant power spectrum. For this reason the uncertainty (complementary sensitivity) weighting function must increase with frequency in order to limit the undesirable transmission of this noise.
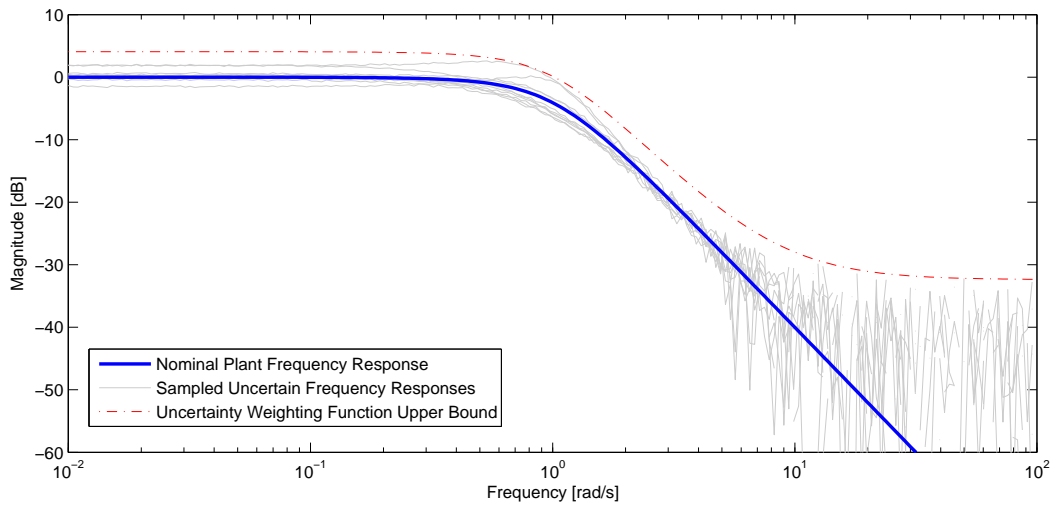
Figure 2.5: Frequency response of nominal mass-spring-damper plant and several sampled responses from the uncertain parameter set with additive Gaussian white measurement noise.

Uncertainty Weighting Function Selection

A simple formula to aid in the selection of the uncertainty weighting function, $W_3(\omega)$, is provided in (4.7). The unstructured uncertainty weighting function should be chosen to overbound the relative (multiplicative) error between the sampled and nominal plant responses at all frequencies. The parameters of (4.7) were adjusted until a relatively tight upper bound on the errors was found: $\Delta_{DC} = 0.6$, $\omega_b = 5$ [rad/s], roll-off rate $= 2$.

$$W_3(s) = \Delta_{DC} \left(\frac{s + \omega_b}{\omega_b} \right)^{\text{roll-off}} = 0.024(s+5)^2 \tag{2.11}$$

Uncertainty weighting functions in the form of (4.7) are improper (order of numerator ¿ order of denominator), and so, like the performance weighting functions introduced previously, are not appropriate for use with automated numerical synthesis routines, which require stable proper transfer function representations. Of course, the weighting function can be made proper by adding sufficiently high-frequency poles; however, this may have other unintended effects on the synthesized controller. The manual Robust Bode techniques, which lack these analytical constraints, therefore offer a more straightforward means of representing the system performance and uncertainty specifications directly.

The performance and uncertainty weighting functions selected for the mass-spring-damper system are shown in Fig. 2.6. Note W_1 and W_3 are not both greater than unity at any frequency since in that case, the robust performance condition $|W_1 S| + |W_3 T| < 1$ would not have a solution.
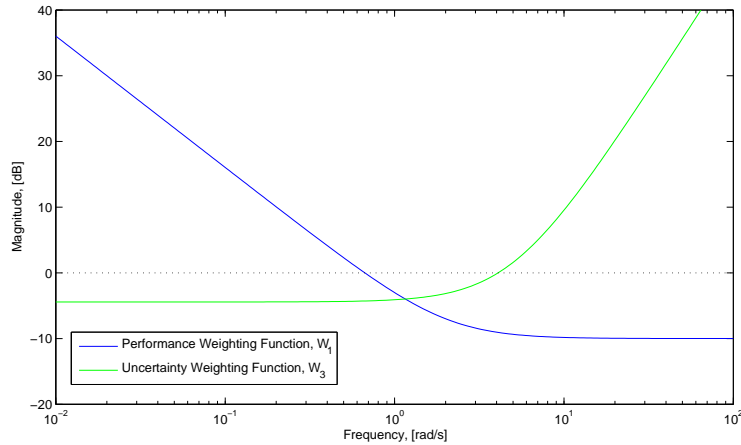
Figure 2.6: Performance and uncertainty weighting functions for the mass-spring-damper system.

20

2.6.1 CRCBode PID Tuning Iterations

It is often the case that the structure of the controller is pre-determined for a particular application. For example existing software may implement a control architecture which can not be easily altered. More often a given control structure is preferred because it has been proven over time and is understood by the operating engineers. In the vast majority of control systems in existence, the proportional-integral-derivative (PID) controller is standard.

Most numerical control synthesis procedures generate high-order controllers of arbitrary structure. This fact is a major reason why "modern" (optimal, robust, etc.) control strategies have not seen more wide-spread adoption in industrial applications in general. Fortunately, a primary benefit of the CRCBode approach is that the form of the controller is explicitly set by the designer, and thus CRCBode methods are especially well suited this type of fixed control structure "tuning" problem.

The PID controller transfer function is typically given by, $C(s) = K_p + K_i/s + K_d s$; however, it is easy to verify that this transfer function is improper (2 zeros/1 pole), and in order to obtain a realizable controller, the derivative term must be rolled-off at some frequency. A PI plus 1st–order filtered derivative controller accomplishing this is provided in (2.12).

$$C(s) = K_p + \frac{K_i}{s} + \frac{K_d s}{T_f s + 1} \tag{2.12}$$

Additionally, for the mass-spring-damper system considered here, the filtered PID controller in (2.12) is necessary for another reason. Since the plant already has a relative degree of 2, in order to achieve the performance specification of -40 dB high-frequency roll-off, the controller must not decrease the relative degree of the loop and so must be at least strictly proper.

Iteration 0

We begin the iterative PID tuning procedure by generating a CRCBode plot based on a unity gain feed-back controller, shown in Fig. 2.7. We see that this unity feed-back controller intersects a large low-frequency forbidden region on the CRCBode plots. This intersection is due to inadequate loop-gain at low frequencies, i.e. lack of integral action.
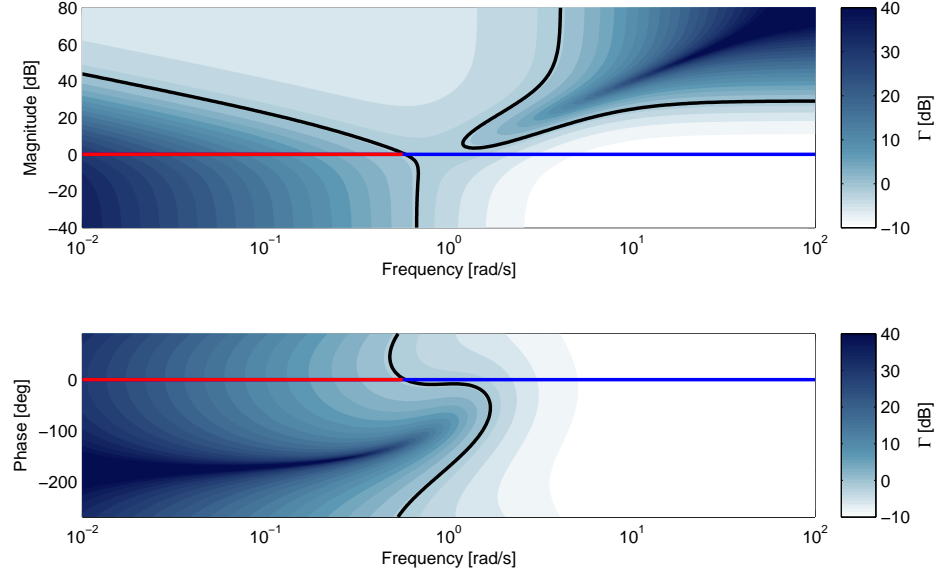
Figure 2.7: CRCBode PID Tuning Iteration 0: $C_0(s) = 1$, (2.13).

$$K_p = 1, \ K_i = 0, \ K_d = 0, \ T_f = 0 \quad \Rightarrow \quad C_0(s) = 1 \tag{2.13}$$
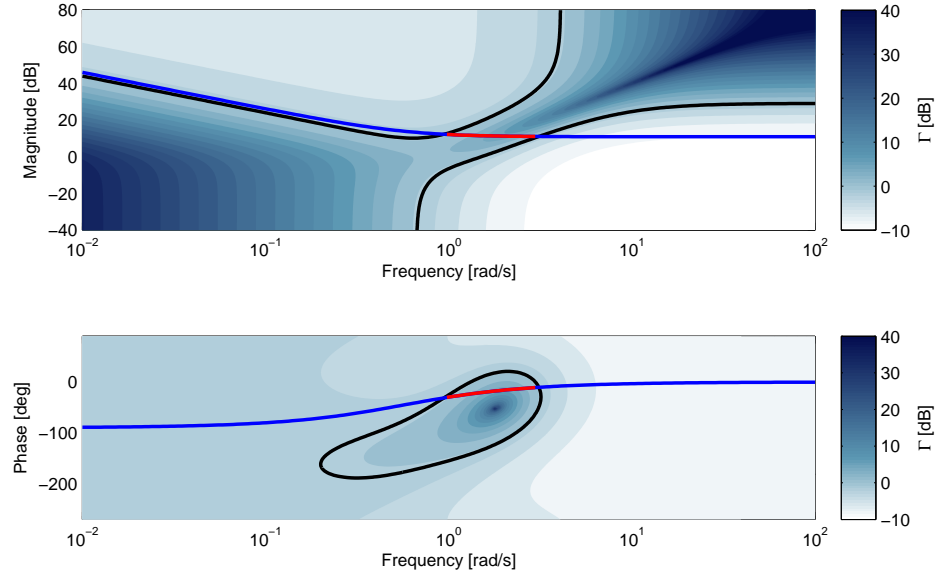
Figure 2.8: CRCBode PID Tuning Iteration 1: $C_1(s)$, (2.14).

$$K_p = 3.5, \ K_i = 2, \ K_d = 0, \ T_f = 0 \quad \Rightarrow \quad C_1(s) = \frac{3.5(s + 0.57)}{s} \tag{2.14}$$

Iteration 1

Generally in the CRCBode loop-shaping design process, we proceed from low to high frequencies combining controllers in an attempt to avoid each of the forbidden regions sequentially. With this in mind, we introduce an integral term into the controller (PI control) and tune the gains so that the controller frequency response just avoids the low-frequency forbidden region as shown in Fig. 2.8. The low-frequency forbidden region is now avoided; however, a mid-frequency intersection has been introduced, which is indicative of inadequate stability margins.

Iteration 2

The proximity of the controller frequency response to the top of the phase forbidden region suggests that adding some additional phase lead near $\omega = 1$ [rad/s] may improve the margins and resolve this issue. Noting that derivative action introduces phase lead, for the next design iteration, we include the filtered derivative term into the controller (PID). The derivative gain and time constants were then tuned simultaneously until the phase forbidden region was entirely avoided as shown in Fig. 2.9.

We see in Fig. 2.9 that the filtered PID controller with tuned parameter values is indeed sufficient to avoid all intersections with the forbidden regions on the CRCBode plots, and therefore, this controller meets all the stated robust stability and performance objectives. We can verify this by examining the sensitivity and complementary sensitivity functions as shown in Fig. 2.10. We see that the desired bandwidth is achieved and the peaking of the sensitivity functions is minimized, indicating well damped responses.

We may also evaluate the performance of this controller by computing the step response of the nominal system and several random samples of the uncertain system, as shown Fig. 2.11. We see that the PID controller designed here is robust to the given uncertainties, since both the nominal system and the sampled uncertain systems exhibit well behaved step responses.
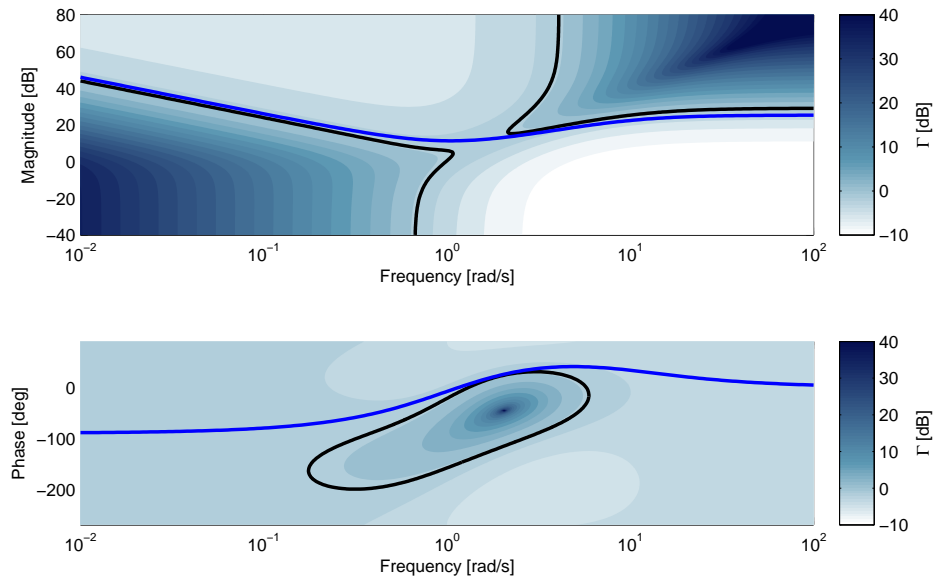
Figure 2.9: CRCBode PID Tuning Iteration 2: $C_2(s)$, (2.15).

$$K_p = 3.5, \ K_i = 2, \ K_d = 1.5, \ T_f = 0.1 \quad \Rightarrow \quad C_{\text{final}}(s) = C_2(s) = \frac{18.5(s^2 + 2s + 1.1)}{s(s + 10)} \quad (2.15)$$
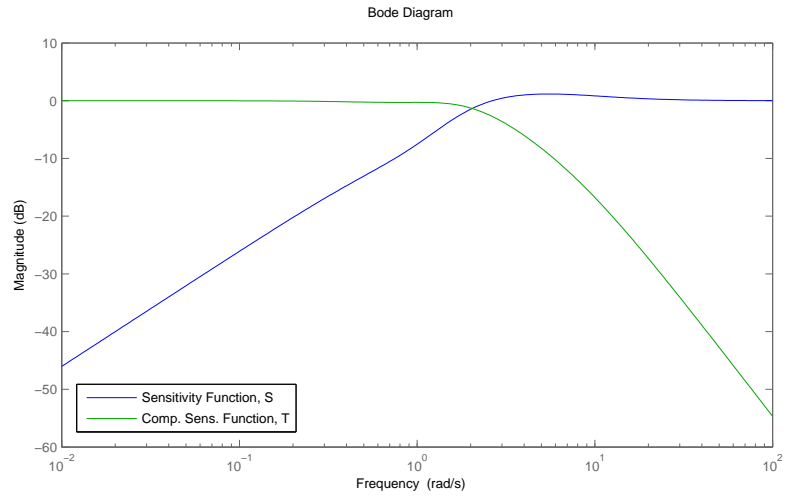
Figure 2.10: Closed-loop sensitivity and complementary sensitivity functions with PID controller, $C_2(s)$, (2.15).
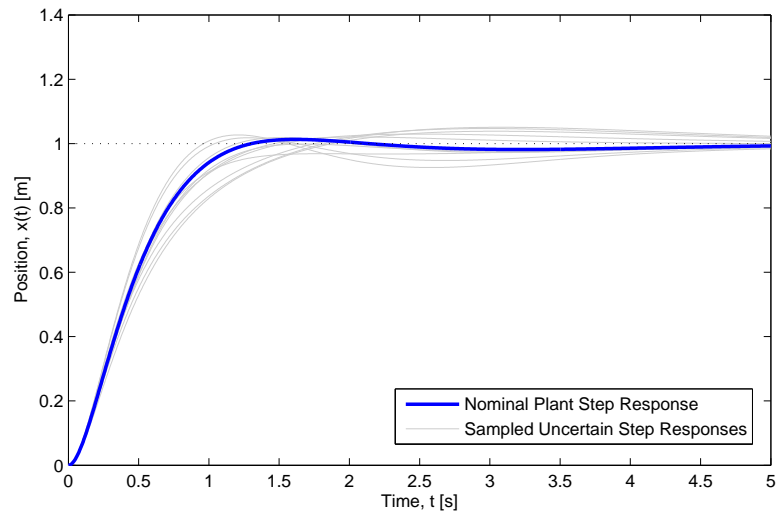
Figure 2.11: Response of PID compensated closed-loop mass-spring-damper system to step command. Both nominal (blue) and sampled uncertain (light gray) responses are shown.

2.7 CRCBode Experimental Case Study –
Nonlinear Valve Flow-Rate Control System

Fluid flow-rate control is an important practical problem encountered in a wide range of applications, including chemical processing, irrigation, HVAC, etc. In particular, we consider the liquid cooling of large-scale electronic systems (e.g. data-centers). A successful control strategy for this system must ensure sufficient flow-rates to each thermal load (CPUs), minimize overall power consumption, and be robust to topological changes in the network both intentional (added loads) and unintentional (leaks). The control actuators investigated in this case are butterfly valves chosen due to their relatively quick response and wider throttling range; however, implementation is complicated by the fact that flow-rate is a highly nonlinear function of valve angle. In the following sections, the CRCBode approach is used to design a controller based on frequency response data from a liquid cooling experimental test-bed which meets specific performance requirements and is robust to the valve nonlinearity and other flow disturbances. The CRCBode approach is preferred in this case since the linearizations of the nonlinear plant about several operating points are considered a set of structured uncertainties for design purposes [23, 24].

2.7.1 Experimental Test-Bed

(a)   (b)
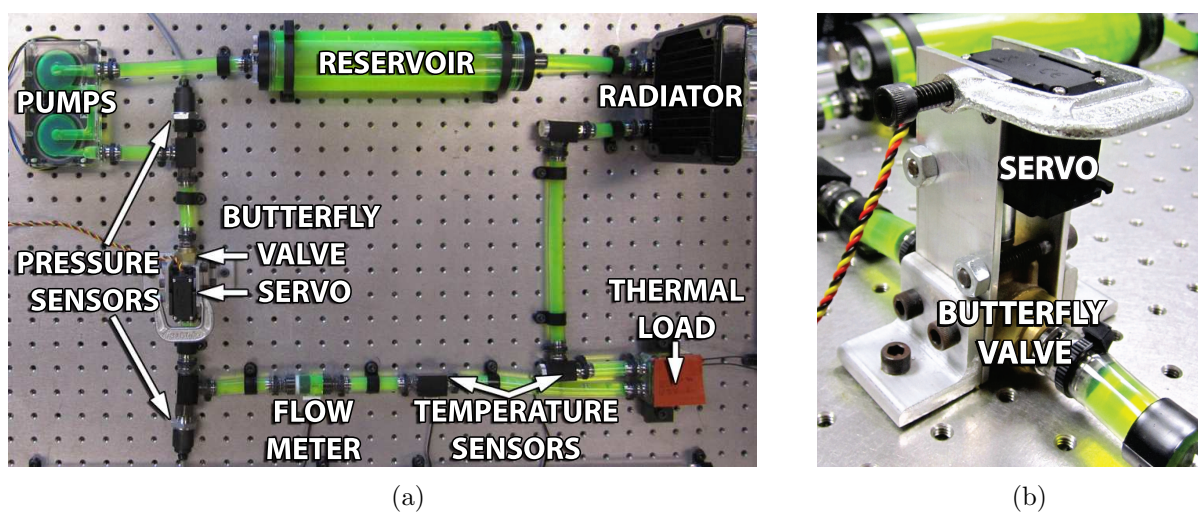
Figure 2.12: (a) Experimental fluid test-bed system. (b) Detail of servo actuated butterfly valve.

We constructed an experimental fluid test-bed in order to study the fluid dynamic, thermodynamic, and control issues arising in a real electronic liquid cooling system. The test-bed, comprising a single flow loop or series connection of elements, consisted of the following components as shown in Fig. 2.12a: a rotary vane flow-rate sensor, a heat exchanger and resistive heating strip to simulate the electronic heat load, thermistor temperature sensors, a combination radiator/fan to dissipate heat to the environment, a fluid reservoir, two small form factor centrifugal pumps connected in series to increase available pressure head, and MEMS gauge pressure sensors to measure valve pressure drop. The control actuator, Fig. 2.12b, consists of a 1/4" butterfly valve directly connected to a metal geared digital servo motor (Hitec HS-5645MG). A standard PWM command signal is provided to the servo which through an internal feedback mechanism sets the valve angle and consequently determines the flow-rate. The entire system is controlled by an Arduino micro-controller. Also, for this project software was developed to transfer system data while in operation from the micro-controller to a PC running MATLAB® for storage, visualization, and analysis.

2.7.2   Butterfly Valve Model and Fluid Resistance
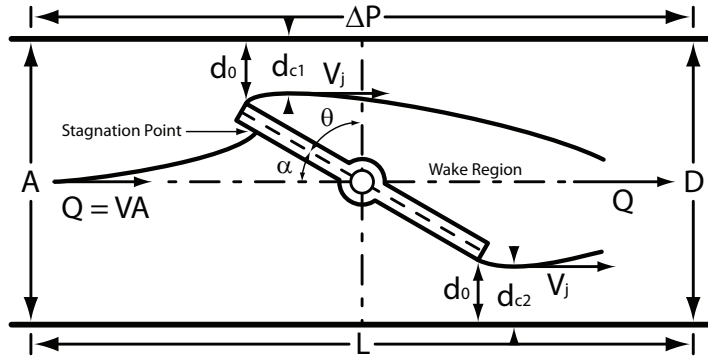
Figure 2.13: Schematic Diagram of Butterfly Valve Flow.

Fig. 2.13 shows a schematic of a typical butterfly valve. The nonlinear relationship between pressure drop across, ΔP, and steady-state volumetric flow-rate through, Q, a butterfly valve as a function of valve opening angle, θ, is provided in Eq. (2.16) [25–27].

$$\Delta P_{\text{valve}} = \zeta_e \, \frac{\rho}{2} \left(\frac{Q}{A} \right)^2 \tag{2.16}$$

where $A = \pi(D/2)^2$ is the valve cross-sectional area, ρ is the fluid density, and ζ_e is the dimensionless pressure coefficient due to viscous losses in the valve, Eq. (2.17).

$$\zeta_e = \left(\frac{2}{(C_{c1} + C_{c2})(1 - \cos(\theta))} - 1 \right)^2 \tag{2.17}$$

where $C_{c1} = d_{c1}/d_0$ and $C_{c2} = d_{c2}/d_0$ are the coefficients of contraction [25, 27].

The nonlinearity of the butterfly valve with respect to valve opening angle, θ, is clear from Eq. (2.17). Note that $\theta = 0°$ corresponds to a closed valve with no flow and $\theta = 90°$ to an open valve with maximal flow. The well-known Darcy-Weisbach equation, Eq. (2.18), models the pressure drop across the other elements of the flow loop, generically referred to as pipes.

$$\Delta P_{\text{pipe}} = f \frac{L}{D} \frac{\rho}{2} \left(\frac{Q}{A} \right)^2 \tag{2.18}$$

L and D are the pipe length and internal diameter respectively, and f is the dimensionless friction factor which depends on the relative roughness of the pipe, ϵ/D, and the Reynolds number of the flow, $\text{Re} = \rho Q D/(\mu A)$, which may be found from the Moody Diagram. For the laminar case, the friction factor takes on the simple form, $f = 64/\text{Re}$. The fluid resistances, i.e. the ratio of pressure drop to volumetric flow rate, $R = \Delta P/Q$, are:

$$R_{\text{valve}} = \frac{\zeta_e \rho Q}{2A^2} \qquad R_{\text{pipe laminar}} = \frac{8\pi\mu L}{A^2} \tag{2.19}$$

The fluid resistances of the series connected elements of the flow loop add and (excluding the valve) may be combined into a single equivalent resistance. The flow-rate may then be calculated from the fluid analog of Kirchoff's Voltage Law, $\Delta P_{\text{pump}} = \Delta P_{\text{valve}} + \Delta P_{\text{pipe equivalent}}$. Note that both R_{valve} and the pump pressure head ΔP_{pump} depend on the flow-rate, Q, so Eq. (2.20) is implicit.

$$Q = \Phi(\theta) = \Delta P_{\text{pump}}(R_{\text{valve}} + R_{\text{pipe equivalent}})^{-1} \tag{2.20}$$

Fig. 2.14 shows the flow-rate as measured in the experimental system along with the laminar model, Eq. (2.20). Note that the x-axis is the commanded position to the servo and not the actual measured angle. The simplified model of Eqs. (2.16)–(2.20) is not entirely adequate since it does not account for turbulence or the servo dead-band; however, this is not an issue since the CRCBode control strategy utilizes only the experimental data and not the model directly.
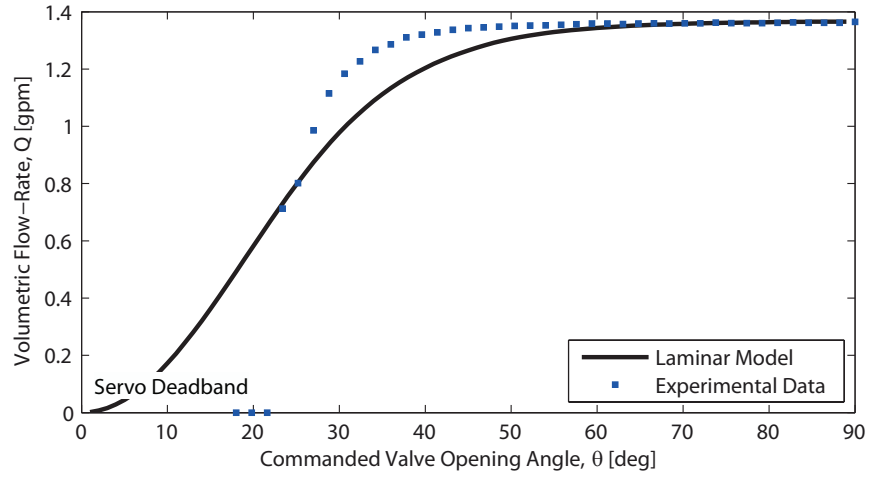
Figure 2.14: Volumetric flow-rate vs butterfly valve (commanded) opening angle.

2.7.3 Servo Model

The linear dynamics of a geared DC electric motor (such as found in the servo) is given by the following transfer function, Eq. (2.21).

$$M(s) = \frac{\Theta(s)}{V(s)} = \frac{NK_\tau}{s[(Js+b)(Ls+R) + (NK_\tau)^2]} \tag{2.21}$$

where Θ is the output shaft angle, V is the applied voltage, N is the gear ratio, $K_\tau = K_\omega$ is the motor torque/speed constant, J and b are the mechanical inertia and damping, and L and R are the terminal motor inductance and resistance respectively. Additionally, the servo has an internal position feedback compensator which is not known; however it is reasonable to assume a proportional-integral (PI) controller, $C_{\text{servo}} = K_P + K_I/s$, resulting in a 4th order system which agrees well with experimental measurements, cf. Section 2.7.9.

2.7.4 Empirical Frequency Response Data

The empirical uncompensated plant frequency responses, $P_n(\omega)$ = flow-rate (output)/servo position command (input) about $N = 4$ operating points (valve angles) were measured, Fig. 2.15. The static valve nonlinearity introduces variations in the gain corresponding to the slope of the curve in Fig. 2.14, and in particular we see that the flow is significantly more sensitive to valve angle when the valve is nearly closed and contributing more to the total system fluid resistance.
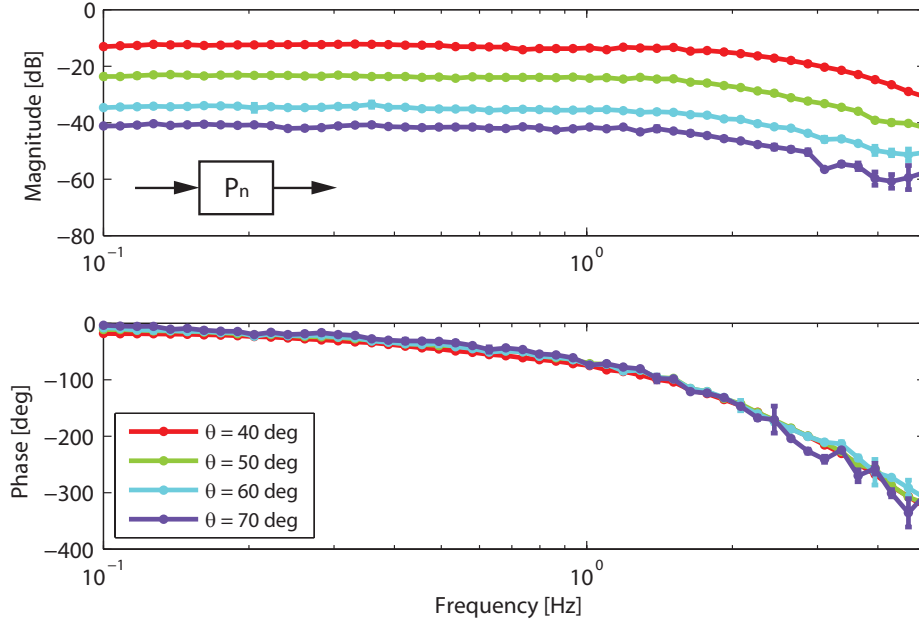
Figure 2.15: Frequency responses of the uncompensated system about N=4 operating points (valve angles).

2.7.5 Performance Specifications

There are several factors making this seemingly benign system somewhat challenging to control, for instance the valve nonlinearity, stiction and saturation effects of the valve, large magnitude low frequency disturbances arising from entrained air pockets in the fluid, and the relatively low bandwidth and poor phase characteristics of the servo/valve assembly. We found that the following specific requirements yield adequate closed-loop system performance: (1) Zero steady-state error for constant disturbance. (2) Disturbance attenuation of at least -3 dB below 2 Hz. (3) Maximum 6 dB disturbance amplification above 10 Hz.

2.7.6 Pre-compensation

The CRCBode plot facilitates the design of a single robust controller for a structured set of uncertain plants. For this system, however, the gain variation of the linearized plant frequency responses is too large over the operating range for a single controller to satisfy the stability and performance requirements for all members of the set simultaneously. We have two options, either relax the performance requirements or alter the frequency responses through pre-compensation to be more manageable.
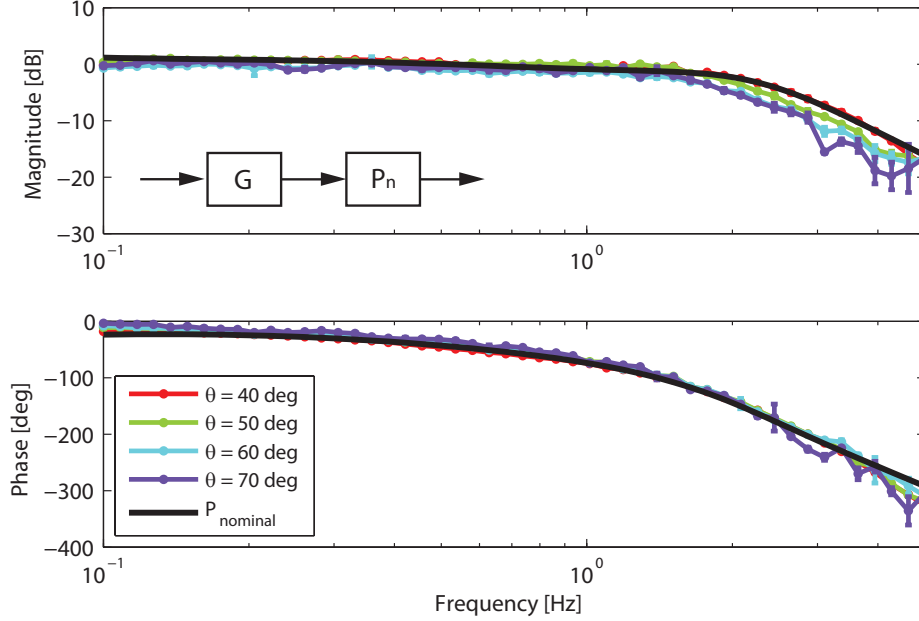
Figure 2.16: Frequency responses of the pre-compensated ($G = (d\Phi/d\theta)^{-1}$) system about four operating points (valve angles) along with the best fit 4th order nominal transfer function model, Eq. (2.31).

In this case we choose the latter approach and pick a gain pre-compensator which corresponds to the inverse slope of the flow-rate/angle relation ($G = (d\Phi/d\theta)^{-1}$), cf. Eq. (2.20). Specifically, we use the experimental data and compute a numerical derivative rather than using the inaccurate laminar model. Using this approach, the frequency responses at each of operating points can be made to generally overlap, as shown in Fig. 2.15, and the robust controller design problem becomes feasible.

2.7.7 Weighting Functions

The second and third performance specifications define bounds on the sensitivity function of the compensated system. Referring to Eq. (2.4), we choose the following sensitivity weighting function to meet those requirements.

$$W_1(\omega) = 0.5 \frac{\sqrt{\omega^2 + 5^2}}{\omega} \tag{2.22}$$

The weighting function for the complementary sensitivity function, W_3, has two roles: uncertainty robustness and noise rejection. In the CRCBode approach, the maximum over all measured

frequency responses is directly evaluated; therefore, for $\omega < 2$ Hz, the only unstructured uncertainty is due to a small (1%) measurement error, so we choose $W_3 = -40$ dB at these frequencies. Above 2 Hz the noise becomes significant, and we choose a W_3 which increases at 60 dB/dec. [3] The performance (sensitivity) weighting function, W_1, and uncertainty (complementary sensitivity) weighting function, W_3, are shown in Fig. 2.17.
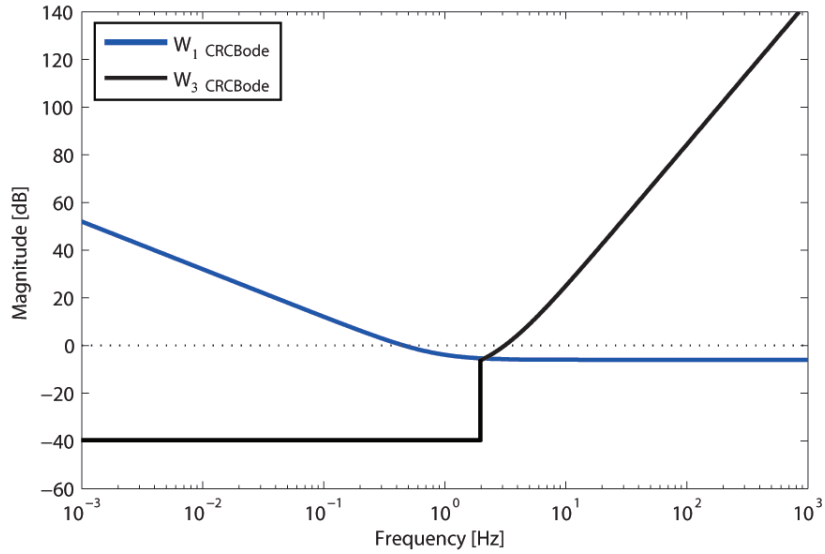
Figure 2.17: Performance and uncertainty weighting functions used in the CRCBode design of the flow-rate control system.

$$W_3(\omega) = \begin{cases} 0.01 & : \quad \omega \leq 2 \text{ Hz} \\ 6.6 \times 10^{-5}(\omega^2 + 15^2)^{3/2} & : \quad \omega > 2 \text{ Hz} \end{cases} \tag{2.23}$$

2.7.8   Loop-Shaping Design Iterations

In this section, we describe the loop-shaping steps required to design a robust compensator for the flow-rate control system using CRCBode plots.

---

[3]When choosing the weighting functions it is important to recall that a necessary condition for a solution to exist is that $W_1 < 1$ or $W_3 < 1$ at each ω.

Iteration 0

We begin the design process by examining the unity gain feedback controller. The CRCBode plot based on this controller and the gain pre-compensated experimental frequency response data is shown in Fig. 2.18. In this case, there are both low $(0.1 - 0.2$ Hz$)$ and high $(2.0 - 3.6$ Hz$)$ frequency intersections of the controller with the forbidden regions $(\Gamma \geq 1)$, indicating that this controller violates the robust performance criteria over these frequencies. Generally we proceed from low to high frequency and cascade compensators in order to avoid these forbidden regions.

Iteration 1

To meet the performance requirement of zero steady-state error for a step disturbance, we include an integrator. The gain is chosen to avoid the forbidden region at the lowest frequencies as shown in Fig. 2.19; however, for this controller two intersections remain between $(0.2 - 1.1$ Hz$)$

Iteration 2

To address the small intersection near 0.2 Hz in Fig. 2.19, we use the Asymmetric Complex Lead (ACL) compensator, [28] to lift the magnitude of the controller over the forbidden region at this frequency.

The general formula for the ACL compensator is given in Eq. (4.5).

$$C_{\mathrm{ACL}}(s) = \frac{\omega_p^2}{\omega_z^2} \left(\frac{s^2 + 2\zeta_z\omega_z s + \omega_z^2}{s^2 + 2\zeta_p\omega_p s + \omega_p^2} \right) \tag{2.24}$$

where $\omega_z = \omega_c(-\zeta_z \tan(\phi_c - \delta) + \sqrt{\zeta_z^2 \tan^2(\phi_c - \delta) + 1})$ and $\omega_p = \omega_c(\zeta_p \tan(\phi_c + \delta) + \sqrt{\zeta_p^2 \tan^2(\phi_c - \delta) + 1})$. ω_c is the frequency (not necessary of maximum phase) where the phase contribution is $2\phi_c$, and $|\delta| < 90° - |\phi_c|$ is the skew parameter. The parameters used here are $\delta = 0$, $2\phi_c = 20°$ at $\omega_c = 0.19$ Hz and damping ratio $\zeta_z = \zeta_p = 0.05$, shown in Fig. 2.20. The CRCBode plot for this step, Fig. 2.21, illustrates that this choice eliminates one intersection; however, the 0 dB cross-over region still exhibits a large intersection.

33
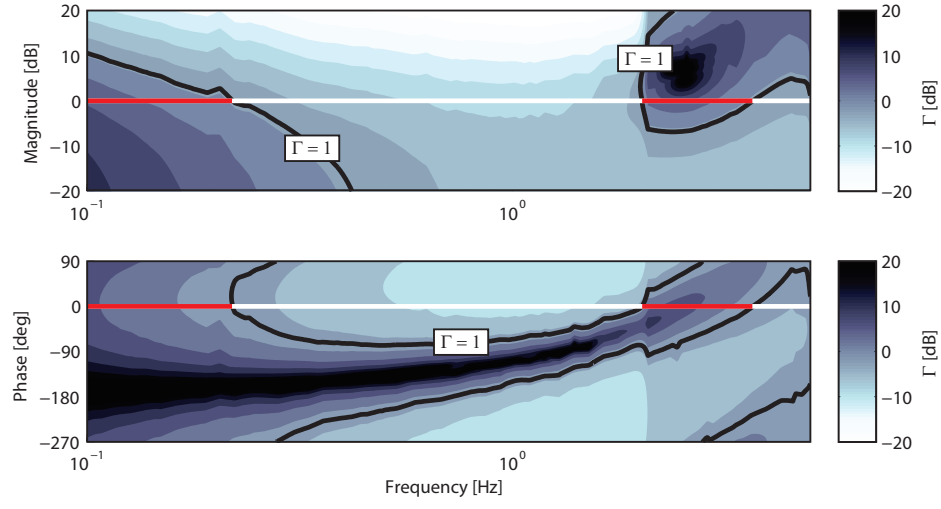
Figure 2.18: Iteration 0: CRCBode plot for the system with proposed compensator C_0, (2.25).

$$C_0 = 1 \tag{2.25}$$
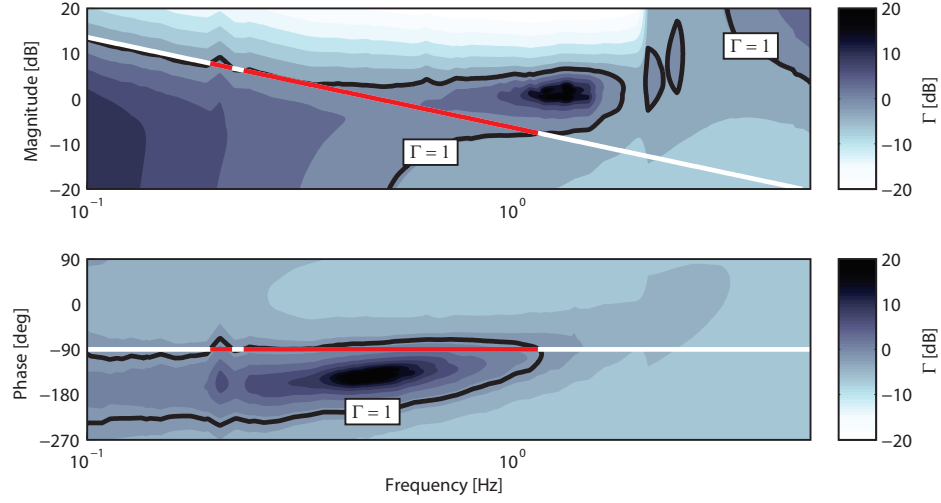
Figure 2.19: Iteration 1: CRCBode plot for the system with proposed compensator C_1, (2.26).

$$C_1 = \frac{3}{s} \tag{2.26}$$
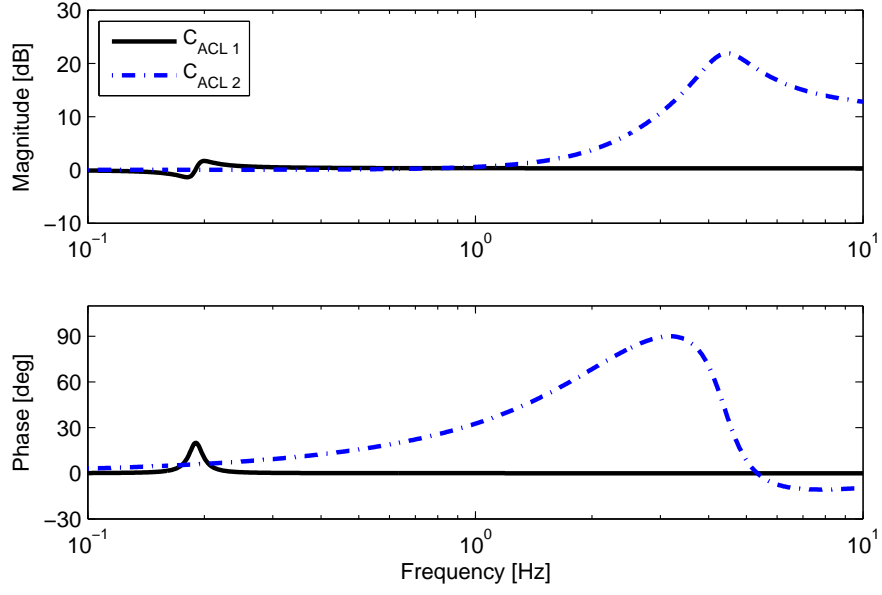
Figure 2.20: Asymmetric Complex Lead (ACL) compensators used in the CRCBode flow-rate controller.
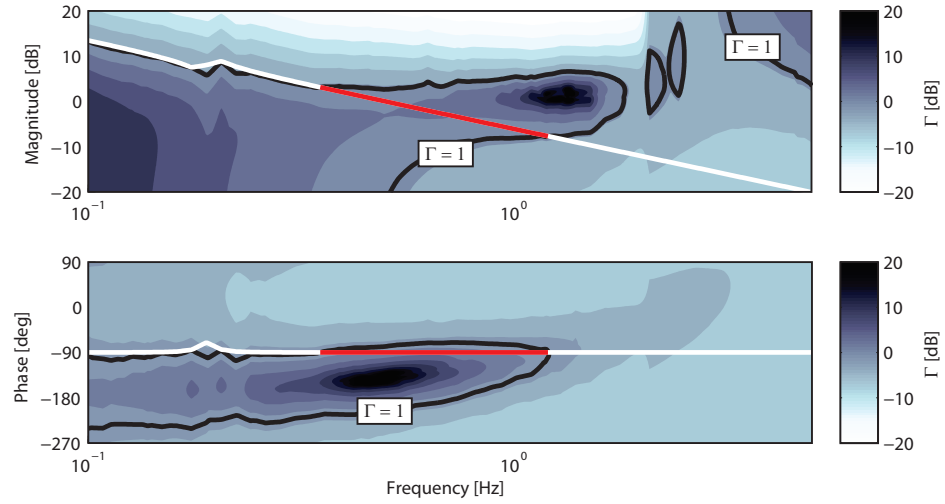
Figure 2.21: Iteration 2: CRCBode plot for the system with proposed compensator C_2, (2.27).

$$C_2 = C_1 \cdot C_{\text{ACL 1}} = C_1 \cdot 1.04 \left(\frac{s^2 + 2 \cdot 0.05 \cdot 1.18s + 1.18^2}{s^2 + 2 \cdot 0.05 \cdot 1.20s + 1.20^2} \right) \qquad (2.27)$$

Iteration 3

The large intersection in the 0 dB cross-over region of Fig. 2.21 is indicative of an inadequate phase margin. It is not immediately obvious how to alter the magnitude to avoid this intersection; however, the phase plot suggests that it may be possible to use an additional compensator providing phase lead to lift the controller frequency response over the phase forbidden region. Fortunately, since the intersections with the forbidden regions are always consistent on both the magnitude and phase plots, either may be used as convenient. Again we use an ACL compensator, Eq. (4.5), shown in Fig. 2.20. In this case, it is somewhat more difficult to select the parameters than in the previous step since ω_c is not centered in the forbidden region of Fig. 2.21. Nevertheless a straightforward trial-and-error process yields parameters which eliminate all intersections on the CRCBode plot, Fig. 2.22: $\delta = 0°$, $2\phi_c = 90°$ at $\omega_c = 3.2$ Hz, $\zeta_z = 0.7$, and $\zeta_p = 0.15$.
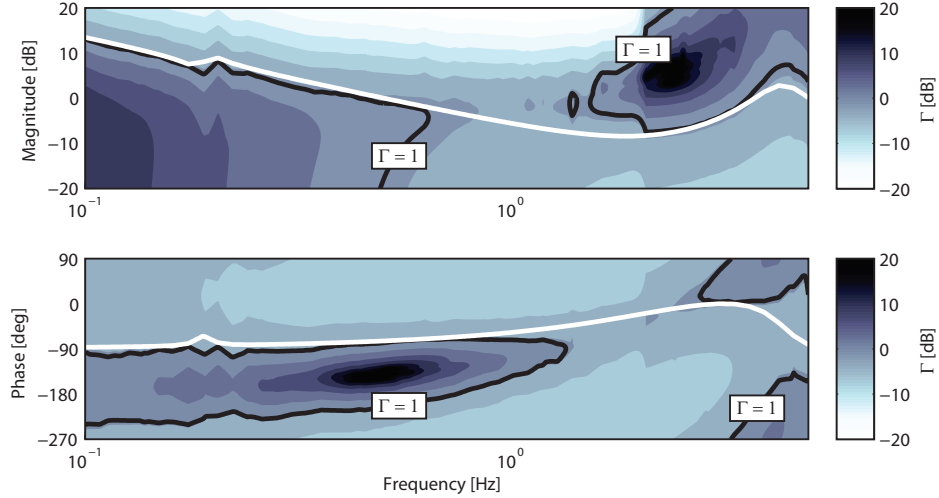
Figure 2.22: Iteration 3: CRCBode plot for system with proposed final compensator $C_{\text{final}} = C_3$, (2.28).

$$C_3 = C_2 \cdot C_{\text{ACL 2}} = C_2 \cdot 3.58 \left(\frac{s^2 + 2 \cdot 0.7 \cdot 14.5s + 14.5^2}{s^2 + 2 \cdot 0.15 \cdot 27.5s + 27.5^2} \right) \tag{2.28}$$

$$C_{\text{final}} = C_3 = \frac{11.12(s^2 + 0.1183s + 1.4)(s^2 + 20.33s + 210.9)}{s(s^2 + 0.1204s + 1.451)(s^2 + 8.24s + 754.5)} \tag{2.29}$$

The CRCBode plot for the final cascaded compensator, Eq. (2.29), is shown in Fig. 2.22. All intersections have been removed and the most sensitive regions (i.e. those with large gradients in Γ) have been avoided. This 5th order controller achieves a gain margin $G_M = 3.7$ (11.4 dB) and phase margin $\phi_M = 62°$ and is of lower order than that produced through the automated H_∞ synthesis described in the following section.

2.7.9 Comparison to Automated H_∞ Synthesis

The weighting functions used in the preceding are standard in the mixed sensitivity robust control problem, so it is straightforward to compare compensators designed using modified Bode methods with those generated using H_∞ automated synthesis tools.

To use the automated H_∞ optimal synthesis tools, it is necessary to choose a nominal plant model and two weighting functions each of which must be represented by a realizable transfer function. Only the nominal plant may be unstable. The weighting functions chosen for the CRCBode approach are clearly not suitable since W_1 is not stable (due to the pole at zero), Eq. (2.22), and W_3 cannot be represented by a realizable transfer function (due to the discontinuity), Eq. (2.23). The performance weighting function can easily be modified to meet the requirements by shifting the pole slightly into the left half plane as shown in Eq. (2.30).

$$W_{1\ \text{auto}}(s) = 0.5 \left(\frac{s + 5}{s + 0.1} \right) \tag{2.30}$$

Determining an appropriate uncertainty weighting function, $W_{3\ \text{auto}}$, requires more analysis. We proceed by first fitting a nominal 4th order transfer function model to the pre-compensated frequency response data (corresponding to the PI compensated servo mechanism with I/O time delay). The best fit transfer function, obtained using the MATLAB$^\circledR$ function `tfest`, is given in Eq. (2.31) and shown along with the pre-compensated frequency response data in Fig. 2.16.

$$P_{\text{nominal}} = 1.45 \times 10^4 \frac{(s + 4.41)}{(s + 84.5)(s + 2.86)(s^2 + 17.8s + 228)} e^{-0.08s} \tag{2.31}$$

The multiplicative errors of the pre-compensated frequency responses from this nominal model, Δ_n, are evaluated and shown in Fig. 2.23. Over the experimental frequency range, the uncertainty weighting function, $W_{3\ \text{auto}}$, Eq. (2.32), is chosen to over-bound the experimental errors, resulting in a 27 dB larger weighting function than that used in the CRCBode approach over this range.
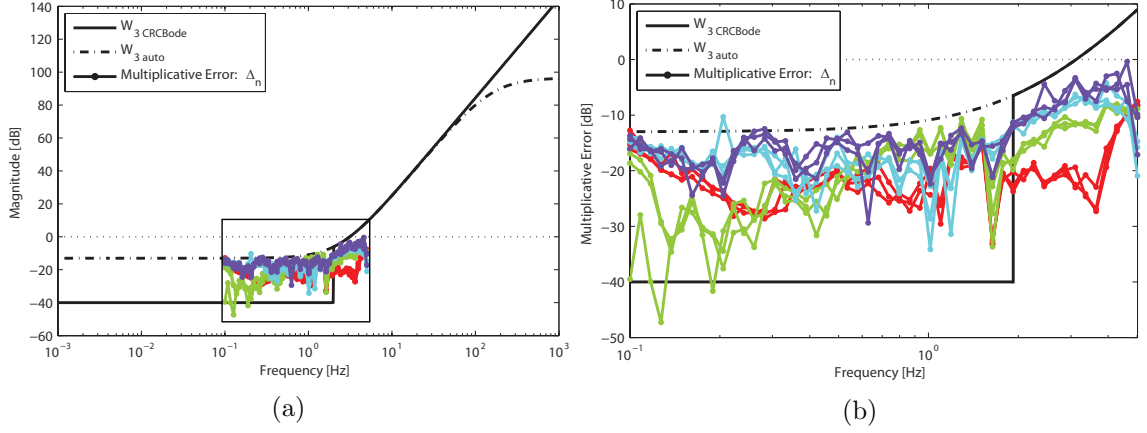
Figure 2.23: (a) Experimental uncertainty of the pre-compensated plant frequency responses about the nominal model, Δ_n, Eq. (2.31), the uncertainty weighting function used in the CRCBode (manual) design process, $W_{3\ \text{CRCBode}}$, Eq. (2.23), and the uncertainty weighting function used in the automated H_∞ synthesis algorithm, $W_{3\ \text{auto}}$, chosen to over-bound the experimental multiplicative uncertainty, Eq. (2.32). (b) Inset showing only measured frequency range (0.1 − 5 Hz)

This is representative of the fact that each measured plant response is included directly in the construction of the CRCBode plot, so the weighting function $W_{3\ \text{CRCBode}}$ must only bound the small measurement error of each response, whereas $W_{3\ \text{auto}}$ must bound all the responses about a single nominal model. Outside of the measurement range, we choose $W_{3\ \text{auto}}$ to generally match $W_{3\ \text{CRCBode}}$ except for the high frequency roll-off since the transfer function must be proper.

$$W_{3\ \text{auto}}(s) = 6.6 \times 10^4 \left(\frac{s + 15}{s + 1000} \right)^3 \tag{2.32}$$

The weighting functions used in the CRCBode and automated H_∞ synthesis approaches are compared in Fig. 2.24. Those used in the automated algorithm roll-off as necessary in order to remain stable and proper. Eq. (2.33) shows the 10th order sub-optimal robust controller, K_{auto}, determined with the MATLAB® command `hinfsyn` based on the weighting functions given in Eq. (2.30) and Eq. (2.32) and the nominal model of Eq. (2.31) with a 2nd order Pade approximation for the time delay (since the plant must be rational). The controllers designed using the CRCBode approach and the automated H_∞ synthesis algorithm are compared in Fig. 2.25.

$$K_{\text{auto}} = 10.6 \times 10^4 \frac{(s + 8.07 \times 10^{-8})(s + 1000)^3(s + 4.27)}{(s + 0.1)(s + 0.171)(s + 6.9)(s + 188)} \quad \times \tag{2.33}$$

$$\frac{(s^2 + 15.3s + 205)(s^2 + 75s + 1880)}{(s^2 + 18.3s + 1080)(s^2 + 114s + 4430)(s^2 + 1.37 \times 10^5 s + 9.35 \times 10^9)}$$
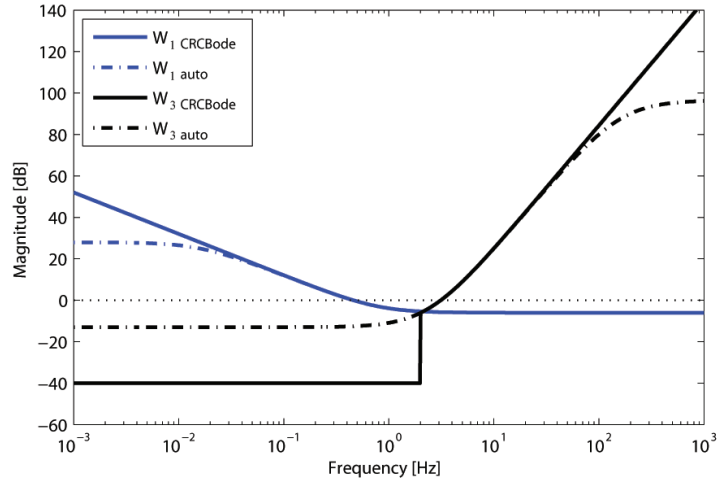
Figure 2.24: Comparison of weighting functions used in the CRCBode and automated H_∞ synthesis approaches. The latter roll-off as necessary in order to remain stable and proper as required by the automated algorithm.

Both controllers exhibit similar trends (e.g phase lead) over the experimental frequency range $(0.1 - 5$ Hz); however, outside of this frequency range, the compensators differ considerably since the weighting functions had to be altered for the automated algorithm. In particular, K_{auto} does not have a pole at zero, so the steady-state error to a step disturbance will be non-zero, and at high-frequencies K_{auto} does not roll-off at the same rate resulting in poorer noise rejection. The higher-order automated controller may be more difficult to implement, although order reduction may mitigate this issue.
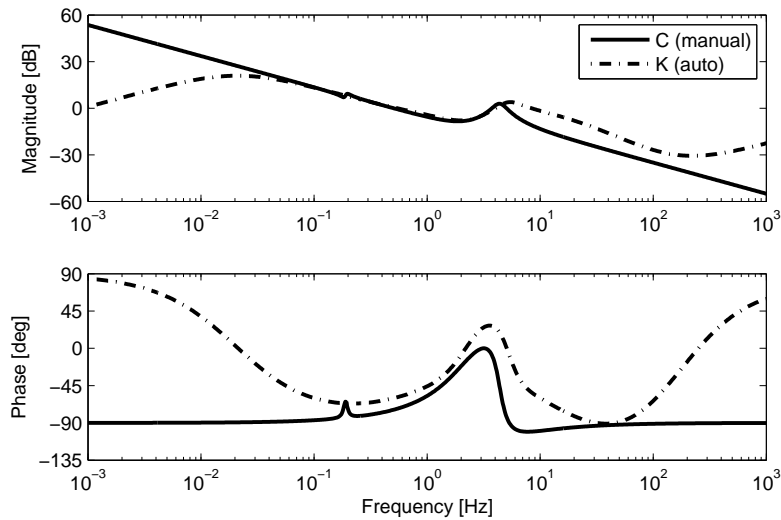
Figure 2.25: Comparison of manual CRCBode and automatically synthesized controller frequency responses.

Fig. 2.26 shows the CRCBode plot based on the automatically synthesized controller, K_{auto}, the weighting functions $W_{1\ \text{auto}}$ and $W_{3\ \text{auto}}$, and the nominal plant model, P_{nominal}. In Eq. (3.22), it was shown that $\gamma \leq 1/\sqrt{2}$ is necessary to ensure robust stability and performance, i.e. $\Gamma_{\text{SISO}} < 1$. In this example, the minimal $\gamma = 0.759 > 0.707$ achieved by the automated controller is not sufficient to meet this bound as evidenced by the intersections of the controller frequency response with the forbidden regions (highlighted in red), though it is met by the manual CRCBode controller. In order to meet this requirement using automated methods, the weighting functions would need to be reduced, effectively "detuning" the controller, demonstrating that the general mixed sensitivity metric, Γ_{MIMO} can be overly conservative.
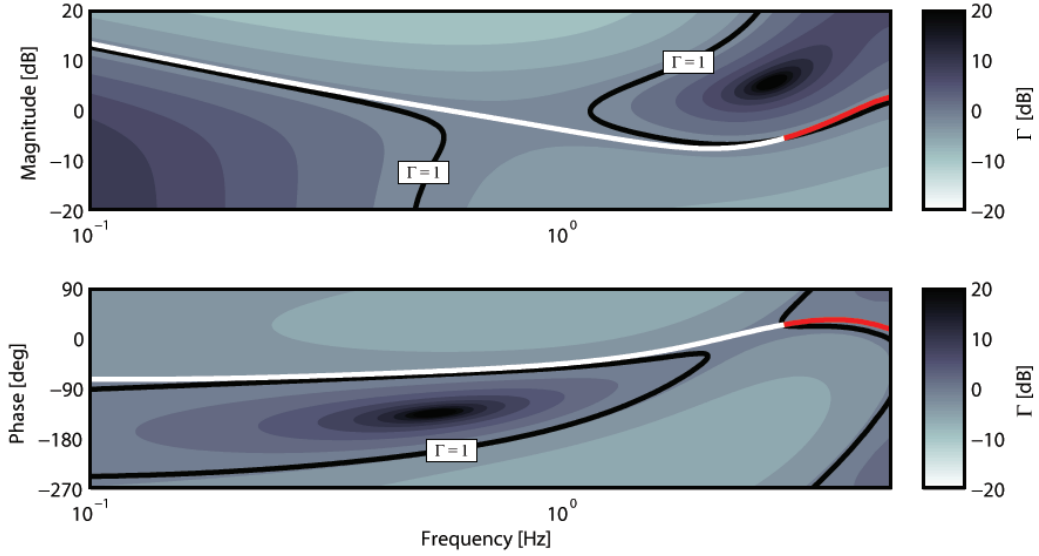
Figure 2.26: CRCBode plot of the automated controller, K_{auto}. In this case, the minimal value achieved by the automated synthesis algorithm, $\gamma = 0.759 > 1/\sqrt{2}$, is insufficient to meet the SISO robust stability and performance bound, $\Gamma_{\text{SISO}} < 1$ over all frequencies, indicated by the intersections of the controller frequency response with the forbidden regions.

2.7.10 Controller Implementation

The CRCBode controller, C_{final}, Eq. (2.29), discretized using a zero-pole matching method with sample rate $T_s = 50$ ms, was implemented in the liquid cooling test-bed. The measured flow-rate response of the compensated closed-loop system to a step change in reference flow-rate is shown in Fig. 2.27a, along with the commanded valve angle input to the servo, Fig. 2.27b.
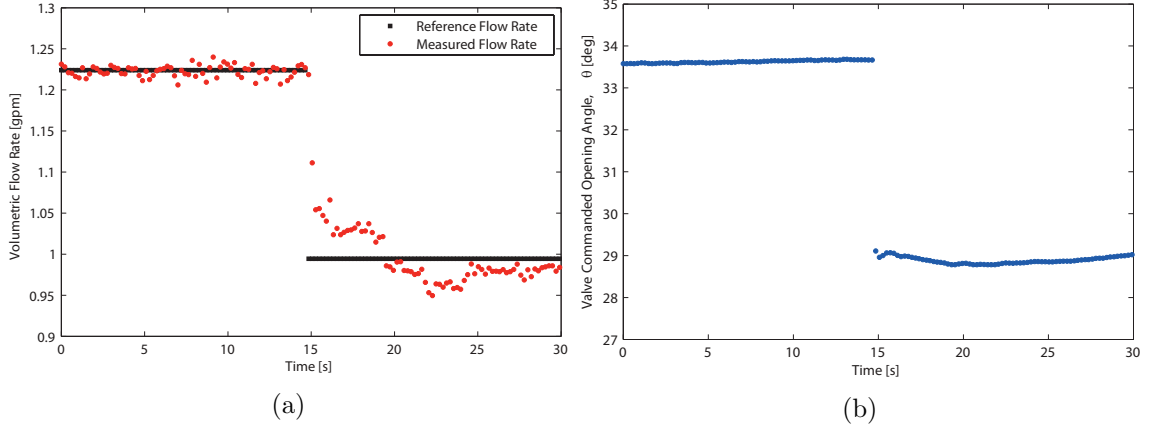
Figure 2.27: ((a) Experimental flow-rate response to step change in reference input. (b) Corresponding commanded valve angle response.

Prior to the step $t < 15$ s, the system exhibits good tracking of the constant reference signal in the presence of high frequency turbulent flow dynamics (resulting in the apparent measurement noise). At $t = 15$ s, the reference signal steps down from 1.23 gpm to 0.99 gpm and the commanded input to the servo exhibits a discrete change due to the feed-forward compensator $F = \Phi^{-1}$ setting a new nominal operating point. The discrepancy between the nominal model Φ and the actual system results in a flow rate which is initially too high. The error remains relatively constant for a time 15 s $< t < 20$ s due to stiction in the valve during which time the controller integrator winds up. At $t \approx 20$ s, the valve breaks free of the stiction and the flow rate suddenly undershoots the desired level. The flow rate remains too low as the integrator winds back down then begins to converge to the correct value but is limited again by stiction. For $t > 25$ s the commanded input is again seen to wind-up due to the small residual error and will eventually break free again and overshoot slightly.

The experimental results demonstrate that the CRCBode designed compensator is effective. The speed of response, however, is primarily limited by the stiction in the valve. Finally, we note that at the step, the pre-compensator gain is reduced according to $G = (d\Phi/d\theta)^{-1}$, since the system is more sensitive to changes in valve angle at lower flow rates, cf. Fig. 2.14. In this example, the gain pre-compensation is in fact essential since the system becomes unstable if the gain is not reduced appropriately.

41

2.8   3D Robust Bode Interpretation

Each of the Robust Bode plots developed in this work is constructed from the following basic procedure: Explicitly evaluate a robust metric, Γ, over a fixed range of independent magnitude and phase perturbations of some frequency-response ($L(j\omega)$, $C(j\omega)$, or $Q(j\omega)$), and verify that the frequency-response remains within the regions in which $\Gamma < 1$ over all frequencies, indicating that a robust performance criteria is satisfied.

Consider the Robust Bode (RBode) plots, based on the loop-transfer function $L = PC$. In constructing the Robust Bode plots the magnitude and phase perturbations are always evaluated independently. Therefore, general perturbations with simultaneous magnitude and phase components are not readily available. To investigate these general perturbations, it is useful to construct a new Robust Bode diagram which exists in the three-dimensional frequency-magnitude-phase perturbation space. We shall denote this diagram as 3DRBode from here on.

An example 3DRBode diagram is presented in Fig. 2.28. As in the standard RBode approach, the robust performance metric, $\Gamma = W_1 S + W_3 T$, is explicitly evaluated over a range of perturbations; however, in this case, the test points constitute a 3D grid inn the frequency–phase–magnitude space. The boundary surface corresponding to $\Gamma = 1$ is computed and visualized along with the nominal loop transfer function, $L_0(j\omega)$.
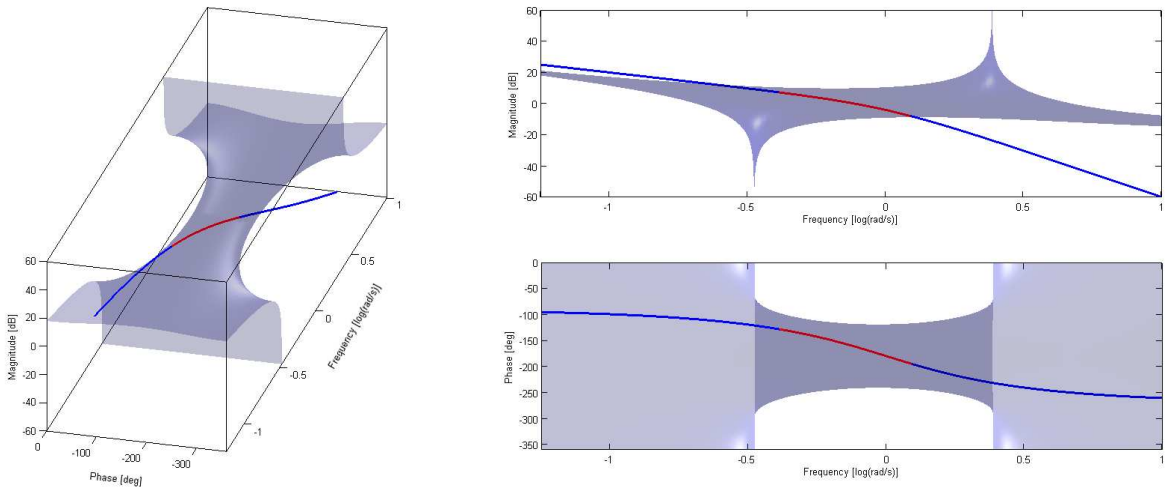
Figure 2.28: Example 3DRBode diagrams.

The robust stability and performance criteria ($\Gamma < 1$), is satisfied if and only if the nominal loop transfer function, $L_0(j\omega)$, does not intersect the 3D boundary surface at any frequency.[4] We have previously observed how controller design using the Robust Bode plots is generally an iterative procedure, since each modification to the proposed controller changes the shapes of the magnitude and phase forbidden regions. This is, however, just a byproduct of how the robust Bode plots are constructed, and not otherwise fundamental to the problem. To fully appreciate this fact, we must investigate how the RBode diagrams are embedded in the higher-dimensional space.
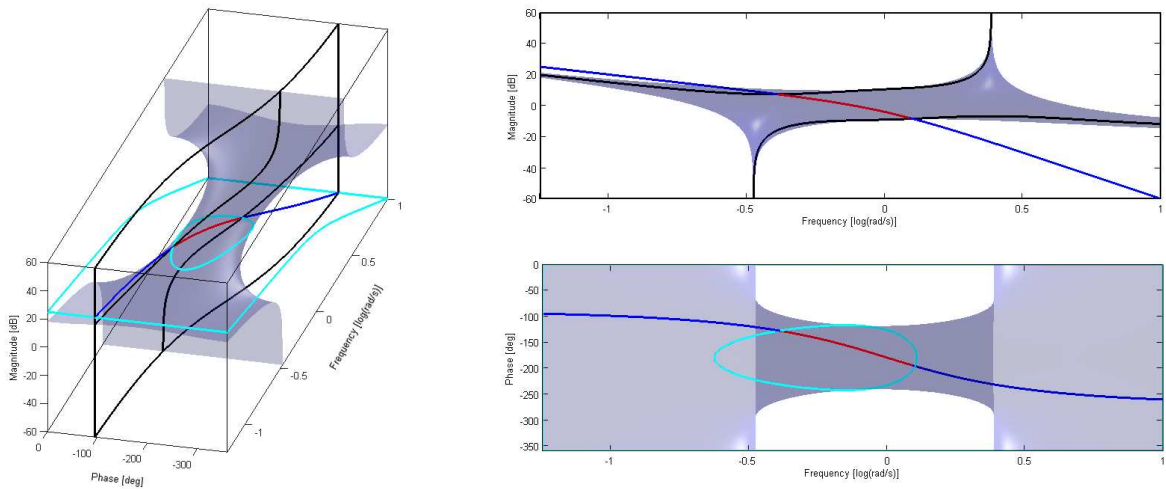
Figure 2.29: 3DRBode diagrams with 2D RBode magnitude (black) and phase (cyan) slices.
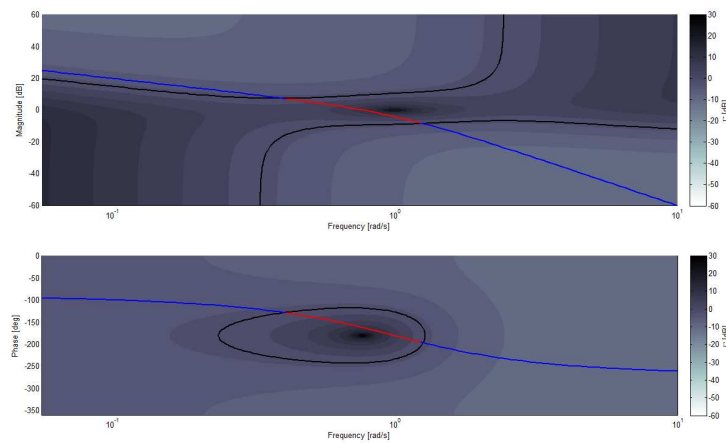
Figure 2.30: Standard contoured RBode plot corresponding to the 3DRBode example of Fig. 2.29.

[4]Intersections are always shown in red.

The RBode magnitude plots assume that phase is constrained at each frequency to that of the nominal system. This corresponds to a vertical slice of the 3D perturbation space following the nominal phase over the frequency range. Similarly, the RBode phase plots assume magnitude is constrained, and thus correspond to a horizontal slice of the perturbation space following the nominal magnitude. Now each of these 2D slices may intersect the 3D boundary surface. These intersections are identical to the forbidden regions displayed on the standard RBode plots. An illustration of these results is presented in Fig. 2.29 and Fig. 2.29 with the RBode magnitude slice shown in black and the phase slice in cyan.

The example presented thus far is a 2nd order system with $K_{DC} = 1, \omega_n = 10$, $\zeta = 0.8$, and a pure integral controller, $C_0 = 1/s$. The loop transfer function is therefore given by:

$$L_0 = P_0 C_0 = \frac{1}{s(s^2 + 1.6s + 1)} \tag{2.34}$$

This system clearly exhibits an intersection with the forbidden region over a limited frequency range. Examining Figs. 2.29 and 2.29, it seems reasonable that a controller providing phase lead over the frequency range (0.5 3 rad/s) may allow the loop transfer function to swing around the forbidden regions. In fact this may be achieved simply with a proportional-integral-derivative (PID) controller, $C_1 = (K_D s^2 + K_P s + K_I)/s$, with the following parameters $K_P = 1.5$, $K_I = 1.0$, $K_D = 0.5$, as seen in Fig. 2.31.
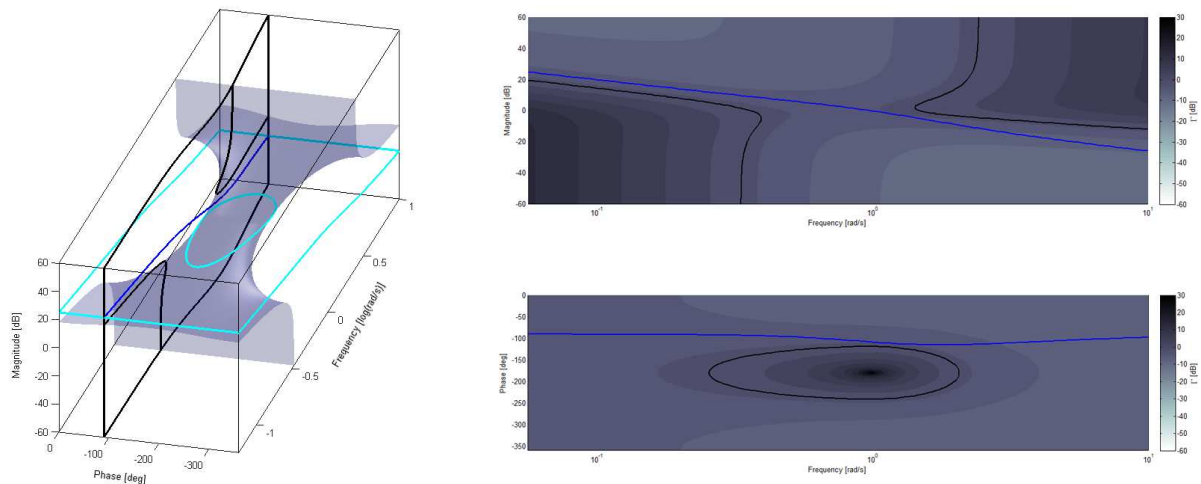
Figure 2.31: 3DBode and corresponding RBode plots showing no intersections with forbidden regions.

The forbidden region boundary surface remains unchanged on 3DRBode diagrams despite variations in the loop frequency-response. The reason for this is that the robust metric, Γ, is explicitly evaluated at each (frequency-phase-magnitude) gridded test point as if the perturbed system actually occupied this point. Neither the nominal frequency response nor the relative size of the perturbation enters in this calculation, and thus the surface is invariant to changes in the nominal response.

Noting the invariance of the boundary surface, a natural question then is why do the forbidden regions change on the standard RBode plots when different controllers are selected? The answer is that though the boundary surface is constant, the magnitude and phase slices which sample the 3D perturbation space do depend on the nominal frequency response in the manner discussed in the preceding sections. This is most clearly demonstrated by showing multiple slices on the same 3DBode plot as in Fig. 2.32, using C_0 (dashed) and C_1 (solid) respectively.
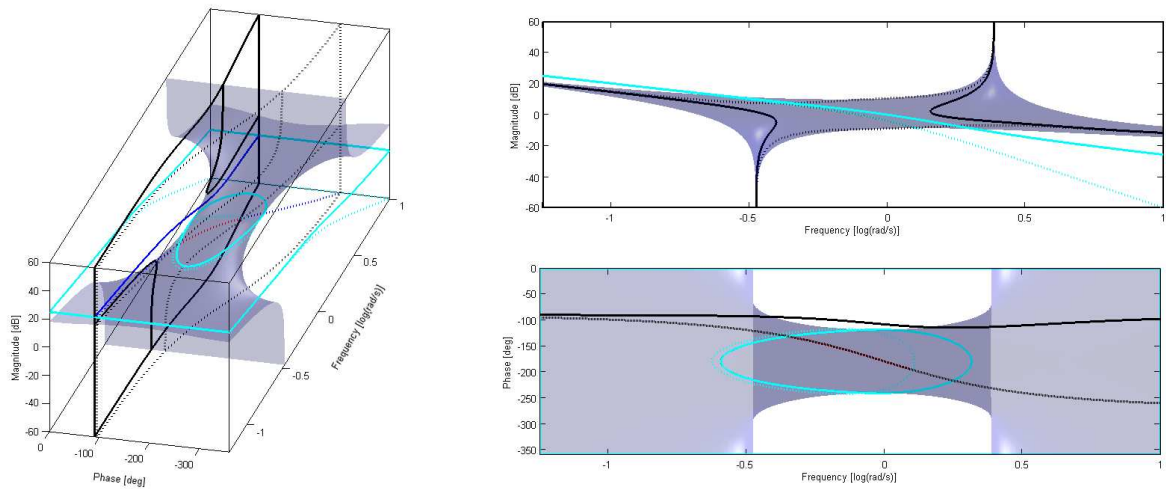
Figure 2.32: 3DBode diagrams showing magnitude and phase slices corresponding to C_0 (dashed) and C_1 (solid).

45

Chapter 3

Robust Stability and Performance Analysis

3.1 Introduction

In this chapter, we review a number of mathematical results regarding the robust stability and performance of general uncertain multi–input/multi–output (MIMO) feed-back systems. The content of this chapter is well-known in the robust control literature, but is included here for completeness. We will use these results in our subsequent development of more advanced Robust Bode methods. More exposition on any of these topics may be found in the following excellent references [1, 12, 18].

3.2 Internal Stability

Consider the generalized feed-back system in Fig. 3.1.
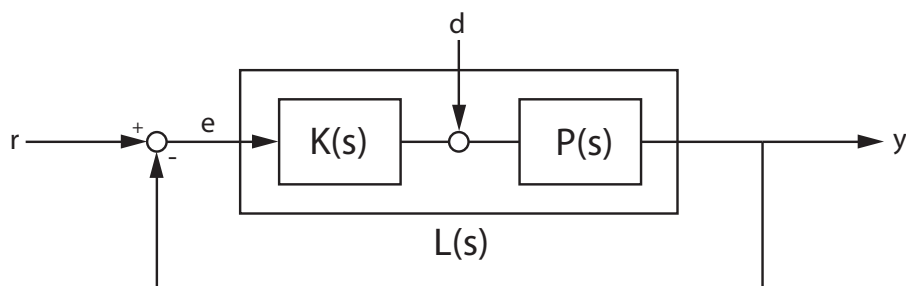
Figure 3.1: General feed-back interconnection structure for internal stability analysis.

where G(s) ad K(s) are arbitrary stable or unstable transfer function matrices of compatible dimensions, represented by the transfer function matrix given in (3.1).

$$\begin{bmatrix} e_1(s) \\ e_2(s) \end{bmatrix} = \begin{bmatrix} H_{11}(s) & H_{12}(s) \\ H_{21}(s) & H_{22}(s) \end{bmatrix} \begin{bmatrix} u_1(s) \\ u_2(s) \end{bmatrix} \tag{3.1}$$

where

$$H_{11}(s) = [I - K(s)G(s)]^{-1} \tag{3.2}$$

$$H_{12}(s) = [I - K(s)G(s)]^{-1}K(s) \tag{3.3}$$

$$H_{21}(s) = G(s)[I - G(s)K(s)]^{-1} \tag{3.4}$$

$$H_{22}(s) = [I - G(s)K(s)]^{-1} \tag{3.5}$$

The system is said to be **internally stable** if e_1 and e_2 are bounded for all bounded inputs u_1 and u_2. This is the case if and only if all four transfer functions $H_{ij}(s)$ are asymptotically stable, that is they must have no poles in the closed right half-plane (CRHP).

3.3   Generalized Nyquist Stability Theorem

The Nyquist stability theorem is fundamental to classical control theory. In particular, it provides the mathematical foundation on which Bode analysis and design principles are based. In previous sections, we have utilized the SISO Nyquist stability theorem to develop a robust stability and performance criteria which formed basis of the CRCBode design method. As in the SISO case, the MIMO generalization of the Nyquist theorem is significant since it provides criteria for the stability of the closed-loop system based only on the open-loop frequency response. As we shall see, the generalized Nyquist theorem also plays a critical role in the structured singular value approach to uncertainty analysis.

To begin, consider the negative feed-back system presented in Fig. 3.1, where $K(s)$ and P(s) are the controller and plant transfer function matrices respectively, and $L(s) = K(s)P(s)$ is the strictly proper loop transfer function matrix. The MIMO Nyquist Stability Theorem is then stated in Theorem 3.6.

Theorem 3.6 (MIMO Nyquist Stability Theorem) $-$ The closed-loop system in Fig. 3.1 is internally stable if and only if:

(1) The image of $\det(I + L(s))$ as s traverses the Nyquist $\mathcal{D}$ contour encircles the origin exactly P_o times counter-clockwise, where P_o is the number of open-loop unstable poles of $L(s)$.

(2) There are no unstable pole/zero cancellations between the plant and controller when forming the product $L(s) = P(s)K(s)$.

The loop transfer function has a right matrix fraction description (MFD), $L(s) = K(s)P(s) = N(s)D(s)^{-1}$, where $N(s)$ and $D(s)$ are polynomial (not rational) coprime matrices, i.e. they share no common factors. For any MFD, z is a system (transmission) zero if and only if the numerator polynomial matrix $N(s)$ loses rank at $s = z$, and p is a system pole if and only if the denominator polynomial matrix $D(s)$ is singular, that is $\det(D(s)) = 0$, at $s = p$. We may thus identify the open-loop characteristic polynomial as $\phi_o(s) = \det(D(s))$, which has P_o zeros at the open-loop poles (including multiplicity) of the MIMO system.

The closed-loop sensitivity function from input r to error e is given in Eq. (3.7). Since $N(s)$ and $D(s)$ are coprime, $D(s)$ and $D(s) - N(s)$ are also coprime, and the closed-loop characteristic polynomial is thus given by $\phi_c(s) = \det(D(s) - N(s))$.

$$S(s) = [I + L(s)]^{-1} = [D(s)D^{-1} - N(s)D^{-1}]^{-1} = D(s)[D(s) - N(s)]^{-1} \tag{3.7}$$

We note that $L(s)$, $N(s)$, and $D(s)$ are all square matrices of equal size. Using the fact that $\det(AB) = \det(A)\det(B)$ for square matrices and $\det(A^{-1}) = \det(A)^{-1}$ for non-singular square matrices, we may take the determinant of the inverse of Eq. (3.7) yielding Eq. (3.8). Thus the zero and pole polynomials of $\det(I + L(s))$ are simply the closed-loop and open-loop characteristic polynomials, respectively, of the MIMO system.

$$\det(I + L(s)) = \det([D(s) - N(s)]D(s)^{-1}) = \frac{\det(D(s) - N(s))}{\det(D(s))} = \frac{\phi_c(s)}{\phi_o(s)} \tag{3.8}$$

We now parallel the SISO Nyquist stability arguments directly, by considering the image of the function $\det(I + L(s))$ as s traverses the standard Nyquist $\mathcal{D}$ contour, i.e. a clockwise encirclement of the entire closed right half-plane (CRHP) along the imaginary axis and at an infinite radius. The usual caveats for poles on the imaginary axis apply.

By Cauchy's argument principle, $N = Z - P$, where N is the number of clockwise encirclements of the origin by $\det(I + L(s))$, $Z = P_c$ is the number of CRHP zeros of $\det(I + L(s))$ (i.e. unstable closed-loop poles), and $P = P_o$ is the number of CRHP poles of $\det(I + L(s))$ (i.e. unstable open-loop poles). Closed-loop stability requires no closed-loop CRHP poles, $Z = 0 \Rightarrow N = -P$. Therefore, for closed loop (input/output) stability, $\det(I + L(s))$ must encircle the origin exactly P_o times in a counter-clockwise (negative) direction, proving Part (1) of Theorem 3.6.

The stability of $S(s) = [I + L(s)]^{-1}$ alone is a necessary but not sufficient condition for the *internal stability* of the feed-back loop. For internal stability, we require that all internal signals are stable for disturbances injected at any point in the loop. Consider, in particular, the transfer function from disturbance d to output, $y(s)/d(s) = [I + P(s)K(s)]^{-1}P(s) = S(s)P(s)$. In order for this transfer function to be stable, all unstable poles of $P(s)$ must be canceled by zeros of $[I + L(s)]^{-1} = D(s)[D(s) - N(s)]^{-1}$. Therefore, any unstable poles of $P(s)$ which are canceled by unstable zeros of $K(s)$ do not appear (are "hidden") in the coprime factor $D(s)$, and are not available to cancel the unstable poles of $S(s)P(s)$. This proves Part (2) of Theorem 3.6.

This internal stability requirement leads to the well known design rule that unstable zeros/poles should never be introduced into the controller to cancel unstable plant poles/zeros. For manual controller design techniques, such as those using the Robust Bode plots, this general rule suffices. However, for automated synthesis methods, additional means of enforcing these constraints must be introduced, the Youla parametrization being one approach. It should also be noted that for most physical systems,it is practically impossible to cancel unstable poles, since due to model uncertainty the exact location of these poles is unknown, in which case even $S(s)$ is unstable.

We may also gain further insight by expanding the determinant in terms of the product of eigenvalues, as in Eq. (3.9). The graphs of $\lambda_i(L(s))$ (i.e. the ith eigenvalue of the open-loop transfer function matrix $L(s)$) as s traverses the Nyquist $\mathcal{D}$ contour are called the *characteristic loci* of the system.

$$\det(I + L(s)) = \prod \lambda_i(I + L(s)) = \prod [1 + \lambda_i(L(s))] \tag{3.9}$$

The MIMO Nyquist stability theorem may now be alternatively stated as: For closed-loop stability, the characteristic loci when taken together must encircle the point -1 exactly P_o times in a counter-clockwise direction. Again, of course, we also require that there are no unstable pole/zero cancellations. As in the SISO case, this interpretation is appealing since the "distance" from the characteristic loci to the -1 point indicates system robustness, and as such, many of the loop-shaping controller design principles may be also generalized to MIMO systems.

3.4 General Uncertain Feed-Back Representation

The uncertain feed-back structure provided in Fig. 3.2 is representative of the general robust control problem, where $P(s)$ is the augmented plant transfer function matrix which includes the nominal plant model and any problem specific weighting functions. Δ is the bounded uncertainty perturbation block, and K is the feed-back controller. w are the *exogenous* input signals, e.g. reference commands and disturbances, z represents the outputs that should be minimized, e.g. error signals, y are the measured plant output variables available to the controller, and u is the control output signal. y_Δ and u_Δ are fictitious signals which arise when the system uncertainty is "pulled out" into the Δ structure. All signals may be vector valued with the blocks being transfer function matrices of compatible dimensions.
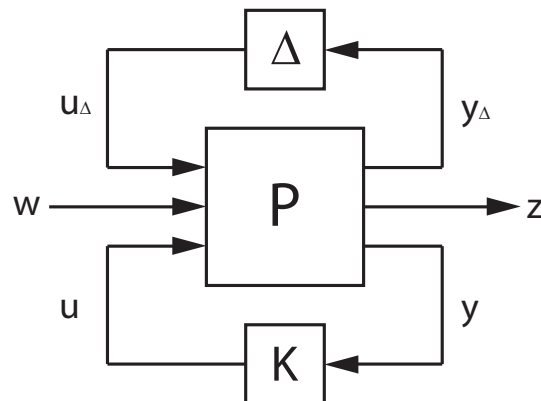
Figure 3.2: General feed-back interconnection structure for robustness analysis.

The generalized feed-back system may first be decomposed into a nominal system with no uncertainty, $\Delta = 0$, shown Fig. 3.3(a). The nominal transfer function from w to z is therefore given by the *lower linear fractional transformation* (lower LFT), Eq. (3.10).
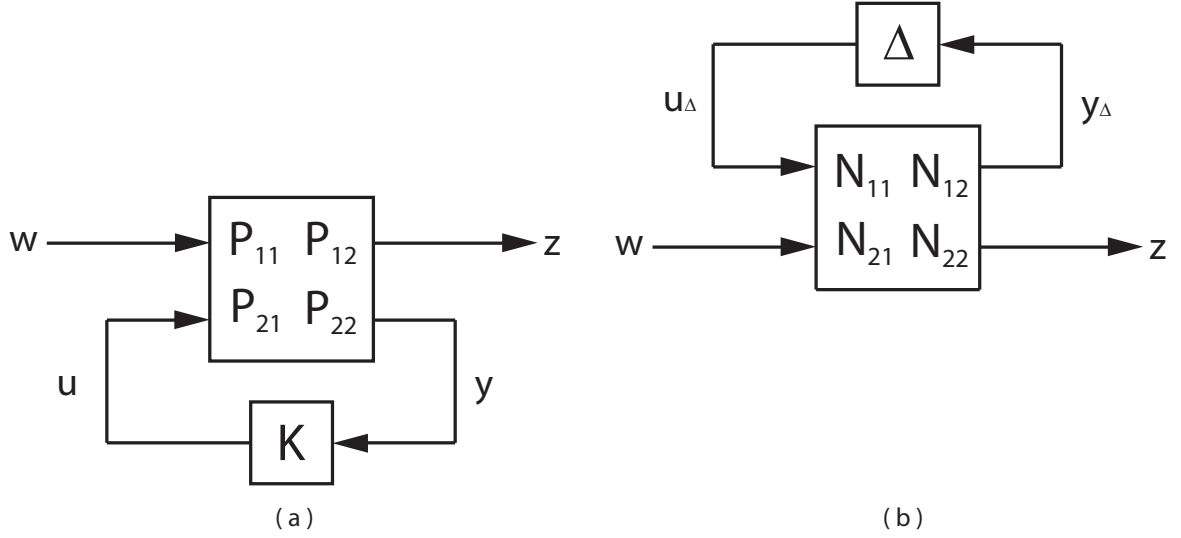
Figure 3.3: (a) Nominal feed-back system (lower LFT). (b) Uncertain $N\Delta$-structure for robust performance analysis (upper LFT).

$$N_{22}(s) = F_l(P, K) \stackrel{\text{def}}{=} P_{11} + P_{12}K(I - P_{22}K)^{-1}P_{21} \tag{3.10}$$

The uncertain closed-loop system may then represented by the $N\Delta$-structure, as shown in Fig. 3.3(b), where N is the nominal closed-loop compensated system. The overall transfer function mapping from exogenous inputs w to outputs z of the uncertain system is then given by the upper linear fractional transformation (upper LFT), Eq. (3.11).

$$H(s) = F_u(\Delta, N) \stackrel{\text{def}}{=} N_{22} + N_{21}\Delta(I - N_{11}\Delta)^{-1}N_{12} \tag{3.11}$$

The robust control problem may then be simply stated as follows: Find a controller $K(s)$ which internally stabilizes the nominal system, robustly stabilizes the uncertain system, and minimizes the error norm $\|H(s)\|_\infty$.

It is useful to introduce another generic uncertain feed-back structure as shown in Fig. 3.4. Here we assume that $M(s)$ and $\Delta(s)$ are both open-loop stable transfer function matrices. If we identify $M(s)$ with, $N(s)$ in Fig. 3.3(b), this implies that the nominal system with $\Delta = 0$ has been stabilized by a suitable choice of controller. The stability of the perturbation structure $\Delta(s)$ implies that the uncertainty does not alter the number of unstable right half plane poles of the open-loop plant. This may seem somewhat restrictive, but in fact, using combinations of feed-forward and feed-back (inverse) representations, stable perturbation matrices can typically been found[1] [18].
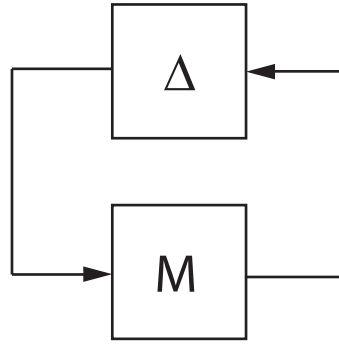
Figure 3.4: Standard $M\Delta$-structure for robust stability and performance analysis.

We now prove a specific result regarding the stability of the $M\Delta$-structure which is essential to the definition of the structured singular value.

Theorem 3.12 (Determinant Robust Stability Condition) − Assuming that $M(s)$ and $\Delta(s)$ are stable and that the allowable perturbations form a convex set, i.e. if Δ is allowed then so is $\epsilon\Delta$ where ϵ is any real scalar with $|\epsilon| \leq 1$, then the $M\Delta$-structure is robustly stable if and only if:

(1)   The Nyquist plot of $\det(I + M(s)\Delta(s))$ does not encircle the origin $\forall \, \Delta$

(2) $\Leftrightarrow$ $\det(I + M(j\omega)\Delta(j\omega)) \neq 0$ $\forall \, \omega, \, \forall \, \Delta$

(3) $\Leftrightarrow$ $\lambda_i(M(j\omega)\Delta(j\omega)) \neq 0$ $\forall \, i, \, \forall \, \omega, \, \forall \, \Delta$

---

[1]More generally, coprime matrix fractional descriptions (MFD) may be used.

Part (1) of the theorem results directly from the generalized Nyquist Theorem 3.6. Since $M(s)$ and $\Delta(s)$ are both assumed open-loop stable, there are clearly no unstable poles or pole/zero cancellations in the product $M\Delta$, so the closed-loop system is internally stable if and only if $\det(I + M(s)\Delta(s))$ does not encircle the origin for any allowable Δ.

Part (2) By contradiction: Assume that the Nyquist plot of $\det(I + M(s)\Delta(s))$ does encircle the origin for some Δ. Then by continuity of the determinant, there would exist an $|\epsilon| \leq 1$ such that $\det(I + M(s)\epsilon\Delta(s)) = 0$, but $\det(I + M(s)\Delta(s))$ must not encircle the origin for internal stability.

Part (3) follows directly from the definition of the determinant as the product of eigenvalues.

3.5 Robust Stability and the Small-Gain Theorem

The basic perturbation model shown in Fig. 5.1 can represent a wide variety of structured (parametric) and unstructured (norm bounded) uncertainties [29].
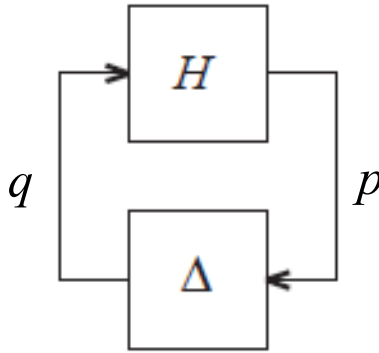
Figure 3.5: Basic perturbation model.

where H represents a generalized (or augmented) plant transfer function matrix whose stability robustness is to be analyzed, and Δ is a perturbation matrix. This general structure can represent many different particular perturbations. For instance, we are often interested in multiplicative perturbations representing relative uncertainty, i.e. the model is known with 10% accuracy. A block diagram showing an output multiplicative uncertainty is shown in Fig. 3.6.
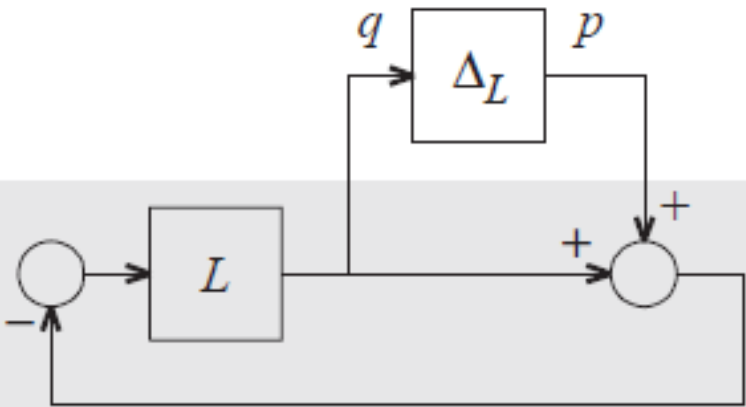
Figure 3.6: Block diagram showing output multiplicative uncertainty.

In this case, $q = -L(p + q)$, therefore the generalized plant is $H = q/p = -L(1 + L)^{-1} = -T$, i.e. the negative nominal closed-loop complementary sensitivity function. As in the SISO case, the generalized (MIMO) Nyquist criteria provides a direct test for robust stability; however, there is a simpler and more conservative alternative based on the *small gain theorem*, Eq. (5.1), which provides a sufficient condition for the stability of the general feedback configuration shown in Fig. 5.1 if H and Δ are both nominally stable:

$$\|H\|_\infty \cdot \|\Delta\|_\infty < 1 \qquad \Leftrightarrow \qquad \overline{\sigma}(H(j\omega)) \cdot \overline{\sigma}(\Delta(j\omega)) < 1 \quad \forall \quad \omega \in \mathbb{R} \qquad (3.13)$$

If scaling factors are introduced to the plant, H, so that the potential perturbations are norm bounded, $\|\Delta\|_\infty < 1$, the small gain condition takes on the particularly simple form, $\|WHV\|_\infty < 1$, where W and V are appropriately chosen output and input weighting matrices respectively. Thus we see that robust stability criteria are naturally formulated as bounds on the weighted nominal closed-loop sensitivity function matrices.

The small gain theorem is extremely useful in robust control due to its simplicity, mathematical tractability, and applicability to not only LTI systems but also nonlinear and time-varying systems. For instance, the well known Popov (circle) criteria for sector bounded static nonlinearities can be derived easily from the small gain theorem. If all perturbations $\|\Delta\|_\infty < 1$ are allowed, that is if the uncertainty is *completely unstructured* then the small gain theorem is both a sufficient and

necessary condition for stability. However, if there is some structure to the perturbation, as is often the case, then the small gain theorem can be excessively conservative.

3.6 Structured Singular Values

The *structured singular value*, developed by Doyle [30] to account for the structure of allowable perturbations, is based on the generalized Nyquist stability criteria, and consequently is a less conservative approach than the small gain theorem. In general the structured perturbations take on a block diagonal form as shown in Eq. (3.14) with each block having dimensions compatible with the pertinent uncertain signals.

(a)

(b)
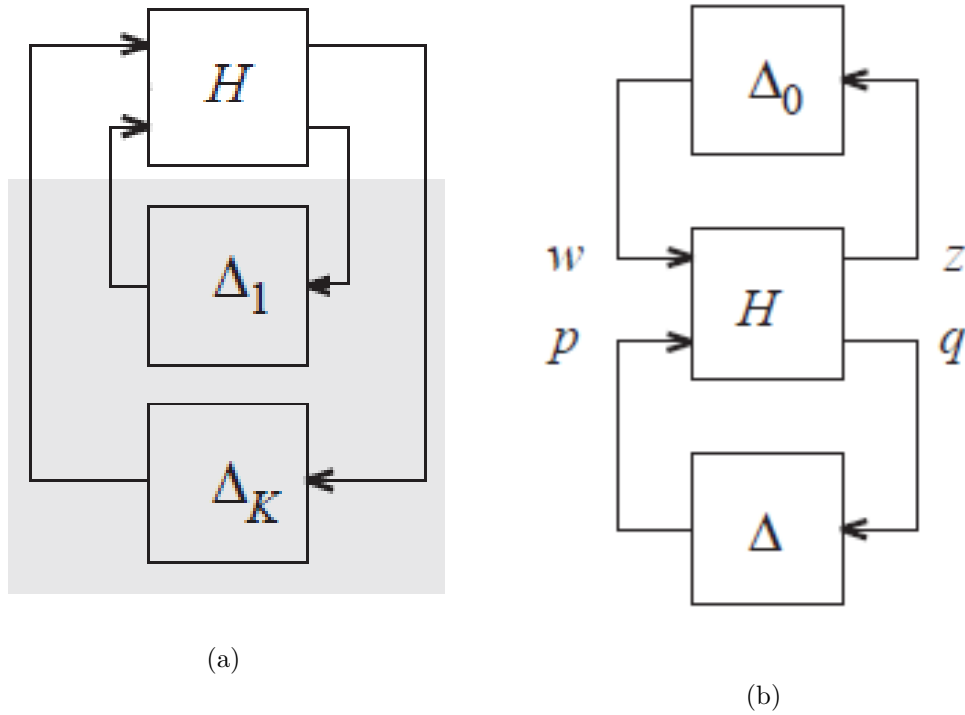
Figure 3.7: (a) shows the block diagram of a system with diagonal structured uncertainty. This uncertainty representation can be used to express combined stability and performance conditions as in (b) with uncertainty perturbation Δ and a hypothetical performance perturbation, Δ_0.

$$\Delta = \begin{bmatrix} \Delta_1 & 0 & 0 \\ 0 & \ddots & 0 \\ 0 & 0 & \Delta_K \end{bmatrix} \qquad (3.14)$$

The generalized Nyquist stability criterion for a MIMO system states that the nominally stable system H is closed-loop stable if and only if the function $\det(I - H\Delta)$ mapped through the standard Nyquist contour does not encircle the origin. The structured singular value at a particular frequency, $\mu(H(j\omega))$, is thus defined as the inverse of the smallest perturbation contained in the allowable set which destabilizes the system, Eq. (3.15), which clearly follows from Part (2) of Theorem 3.12.

$$\frac{1}{\mu(H)} = \inf\{\overline{\sigma}(\Delta) : \det(I - H\Delta) = 0\} \tag{3.15}$$

Therefore, the system remains robustly stable if and only if

$$\mu(H(j\omega)) \cdot \overline{\sigma}(\Delta(j\omega)) < 1 \quad \forall \quad \omega \in \mathbb{R} \tag{3.16}$$

Furthermore, for scaled perturbations, $\|\Delta\|_\infty < 1$, the robust stability condition is simply, $\|\mu(H)\|_\infty < 1$. If the perturbation is unstructured, this reduces to the standard small gain theorem, Eq. (5.1). The structured singular value is used in the following section to derive an important result concerning the combined robust stability and performance of the mixed sensitivity problem.

3.6.1 General Mixed Sensitivity Problem

The mixed sensitivity problem is a standard robust control problem concerned with minimizing the H_∞-norm of a particular matrix of weighted sensitivity transfer functions [31], motivated by the general feedback block diagram, Fig.3.8.

The augmented plant transfer function matrix from disturbance input, u_1, to regulated outputs, y_1, is $H = [W_1S \quad W_2KS \quad W_3T]^T$. The general mixed sensitivity problem is therefore to find a stabilizing controller, K, which minimizes, γ, the H_∞-norm of the combined sensitivity function matrix

$$\|H\|_\infty = \left\| \begin{matrix} W_1S \\ W_2KS \\ W_3T \end{matrix} \right\|_\infty = \gamma \tag{3.17}$$
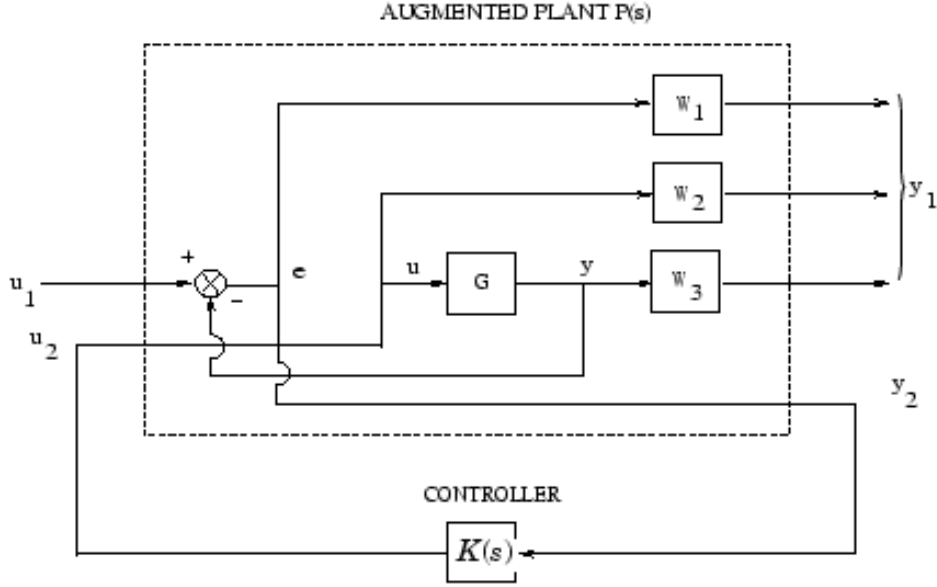
Figure 3.8: Feedback block diagram for standard mixed sensitivity problem. (Figure from MATLAB documentation for `mixsyn` algorithm)

3.6.2 Conservativeness of Mixed Sensitivity Metrics

The structured singular value, by definition, is the least conservative means of accessing the robust stability of a particular perturbation structure, and consequently $\mu(H) < 1$ is the best choice for a robustness criteria. The general mixed sensitivity problem, Eq. (5.2), however, minimizes $\|H\|_\infty = \gamma$. For a SISO system (i.e. P and C are complex scalars), the singular value can be evaluated directly using $\sigma_i(H) = \sqrt{\lambda_i(H'H)}$ giving:

$$\|H\|_\infty = \max\{\sqrt{|W_1(j\omega)S(j\omega)|^2 + |W_2(j\omega)K(j\omega)S(j\omega)|^2 + |W_3(j\omega)T(j\omega)|^2} : \omega \in \mathbb{R}\} = \gamma \quad (3.18)$$

To derive a less conservative robust stability and performance criteria using the structured singular value, we consider the following feedback block diagram which explicitly includes the output multiplicative uncertainty perturbation block, Δ, and in so doing gain insight into the relationship between Γ_{SISO} and Γ_{MIMO}.
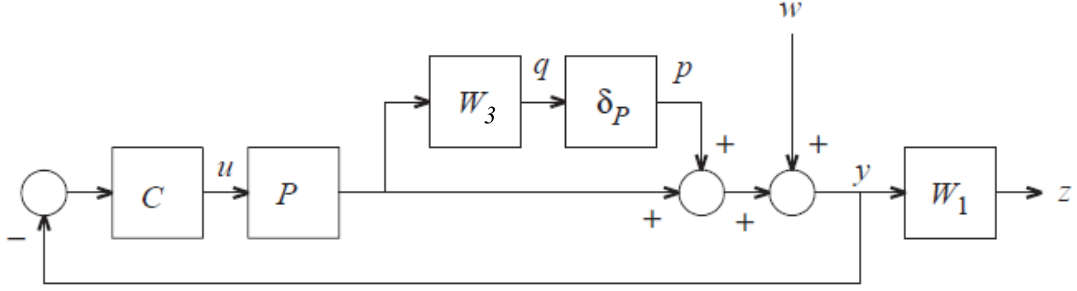
Figure 3.9: Block diagram showing uncertainty and performance weighting functions.

The transfer function matrix, H, from disturbance inputs to the regulated outputs, $[q\ z]^T = H\ [p\ w]^T$ is given by

$$
\begin{bmatrix} q \\ z \end{bmatrix} = \begin{bmatrix} -W_3 T & -W_3 T \\ W_1 S & W_1 S \end{bmatrix} \begin{bmatrix} p \\ w \end{bmatrix} = \begin{bmatrix} W_3 T \\ W_1 S \end{bmatrix} \begin{bmatrix} -1 & 1 \end{bmatrix} \begin{bmatrix} p \\ w \end{bmatrix} \tag{3.19}
$$

Now note that the eigenvalues, $\lambda([1\ -1; -1\ 1]) = \{2,\ 0\}$, so the maximum singular value, $\bar{\sigma}(H)$ is given by

$$
\|H\|_\infty = \max\{\sqrt{2}\sqrt{|W_1(j\omega)S(j\omega)|^2 + |W_3(j\omega)T(j\omega)|^2} : \omega \in \mathbb{R}\} \tag{3.20}
$$

In this case, H is a dyadic matrix (product of column and row vector). For dyadic matrices, it can be shown (See Appendix) that the structured singular value is

$$
\|\mu(H)\|_\infty = \||W_1 S| + |W_3 T|\|_\infty = \max\{|W_1(j\omega)S(j\omega)| + |W_3(j\omega)T(j\omega)| : \omega \in \mathbb{R}\} \tag{3.21}
$$

For SISO systems, we have shown using both graphical Nyquist and structured singular arguments that the best robust performance and stability criteria is $\||W_1 S| + |W_3 T|\|_\infty < 1$. However, the standard mixed sensitivity problem instead minimizes $\gamma = \|\sqrt{|W_1 S|^2 + |W_3 T|^2}\|_\infty$. To compare these two metrics, we present a brief proof of the equivalence of vector space p-norms. For any n-dimensional vector $\mathbf{x} = \sum_{i=1}^n \alpha_i \phi_i$ with standard basis ϕ_i and any arbitrary norm, $\|\cdot\|$. By the positive scalability and triangle inequality properties of a norm, $\|x\| = \|\sum_{i=1}^n \alpha_i \phi_i\| \leq \sum_{i=1}^n |\alpha_i|\|\phi_i\|$, and by Cauchy's inequality, $\sum_{i=1}^n |\alpha_i|\|\phi_i\| \leq \sqrt{\sum_{i=1}^n |\alpha_i|^2}\sqrt{\sum_{i=1}^n \|\phi_i\|^2} = \sqrt{n}\|\mathbf{x}\|_2$. So for a SISO system with $\mathbf{x} = [W_1 S\ W_3 T]^T$ and $n=2$, it follows that

$$
|W_1 S| + |W_3 T| \leq \sqrt{2}\sqrt{|W_1 S|^2 + |W_3 T|^2} \tag{3.22}
$$

Thus in the SISO case, **the structured singular value approach is less conservative** since the general mixed sensitivity metric, γ, must be minimized to $\gamma \leq 1/\sqrt{2} = 0.707$, to ensure robust stability and performance which may not be possible even if $\Gamma_{\text{SISO}} = \||W_1 S| + |W_3 T|\|_\infty < 1$ can be achieved, see for instance Fig. 2.26.

The same argument applies to more general MIMO systems; unfortunately, since the structured singular values can no longer easily be evaluated, the necessary minimum γ is not evident. Therefore, we must resort to the more conservative metric, $\Gamma_{\text{MIMO}} = \|W_1 S \quad W_3 T\|_\infty$, and recognize that $\Gamma_{\text{MIMO}} < 1$ may not be sufficient. Instead, in the MIMO modified Bode approach, an attempt must be made to minimize Γ_{MIMO} as much as possible below unity, and stability should be verified independently using other means. This is similar to the procedure used in standard automated H_∞ synthesis algorithms (c.f. Youla parametrizations [10]).

Chapter 4

Robust Bode Methods for SISO Unstable and Non-Minimum Phase Systems

4.1 Introduction

In Chapter 2, we investigated the problem of flow-rate control of a butterfly valve based liquid cooling system. This system was non-trivial, containing significant nonlinearities, unmodeled dynamics, and large magnitude disturbances (turbulence), but despite these complications, a controller meeting the required robust stability and performance objectives was obtained simply using loop-shaping techniques and the Contoured Robust Controller Bode (CRCBode) plots. As we shall see, the tractability of this controller design problem was primarily due to the the valve system being both open-loop stable (only left half-plane poles) and minimum phase (only left half-plane zeros).

Stable minimum-phase systems are the easiest type of system to control. If there were no model uncertainty and infinite control authority, any desired performance characteristics could be achieved in a straightforward fashion. For instance, if $L = \omega_c/s$ is identified as the target loop shape providing 90° phase margin, infinite gain margin, and a cross-over frequency of ω_c, then a controller generating this loop-shape may be found from $K(s) = L(s)P^{-1}(s)$. In Chapter 3 we showed that internal stability is possible only if there are no right half-plane pole/zero cancellations between the plant and controller. Clearly then this "dynamic inversion" based controller is only feasible when the plant itself is both stable and minimum phase.

There are additional issues, however, with this inverse based control strategy. In particular, $K = LP^{-1}$ will not be proper and thus not realizable if the relative degree of the plant is greater than that of the desired loop shape. In theory, this may be overcome by adding high-frequency dynamics to the controller, but this requires very large control bandwidth which is impractical. Also due to uncertainty in the system, the model based plant inverse, P^{-1}, will likely not be in agreement with that of the real system, possibly leading to greatly degraded performance.

In fact, right half-plane poles and zeros lead to additional analytic constraints on the system which fundamentally limit the achievable closed-loop performance even if there were no uncertainty and infinite control authority. We will show that unstable poles impose a lower limit on the required bandwidth and non-minimum phase zeros an upper limit on achievable bandwidth and thus speed of response of the system. If there are both right half-plane zeros and poles, then these constraints may conflict with increasingly poor results as the poles and zeros move closer together.

How often then should we expect to encounter problems such as these, or rather how common are unstable and non-minimum phase systems in practice? We know that engineers generally prefer stable systems for obvious safety reasons; however, there are certain applications where open-loop instability or marginal stability is essential to the basic functionality of the system, for example bipedal walking robots [32]. Non-minimum phase zeros are perhaps more common and often arise due to time-delays in the system, which we may see by considering the first-order Padè approximation: $e^{\tau s} \approx (1 - k_1 s)/(1 + k_2 s)$, where τ is the time delay in seconds.

Another characteristic of non-minimum phase systems is the so-called "inverse response" in which for a step disturbance the system initially moves in the opposite direction to the desired steady-state value. This effect is commonly encountered in aircraft in which tail mounted elevators are used to control altitude. The downward force at the rear of the aircraft initially moves the center of mass downward before the lift increase on the wings due to the increased angle of attack begins to accelerate the back upward. Thus inputs having competing effects on the system dynamics output generally exhibit non-minimum phase behavior.

In this chapter, we extend the Robust Bode methods to open-loop unstable and non-minimum phase single-input/single-output systems. We begin by reviewing the algebraic and analytical constraints affecting these systems and discuss how these constraints limit achievable performance. We then proceed with a simple non-minimum phase example, and along the way introduce the celebrated Youla parametrization of all internally stabilizing controllers which greatly facilitates

robust controller design process. In particular, we show how loop-shaping controller design may be performed directly on the controller. i.e. using the CRCBode plots, or on the Youla parameter, $Q(s)$, using a new robust bode plot called QBode, comparing the advantages and disadvantages of each method [33].

We then move on to unstable plants, the Youla parametrization of which requires the introduction of state-space methods for coprime factorization. These methods lead naturally to an elegant connection between linear-quadratic Gaussian (LQG) optimal control theory and Robust Bode loop-shaping controller design. Finally we pursue this connection by conducting an in depth case study of an inverted pendulum system and in so doing demonstrate many of the difficulties associated with combined unstable and non-minimum phase plants.

4.2 SISO Robust Performance Levels

As in Chapter 2, for SISO systems, we consider the following robust performance metric:

$$\Gamma_{\mathrm{SISO}}(\omega) \triangleq |W_1(j\omega)S_n(j\omega)| + |W_3(j\omega)T_n(j\omega)| \tag{4.1}$$

where W_1 is the performance function weighting the nominal sensitivity, S_n, and W_3 is the uncertainty function weighting the complementary sensitivity, T_n.

Robust performance, $|W_1S| < 1$, implies robust stability, $W_3T| < 1$. Therefore, to ensure that the closed-loop system is both robustly stable and exhibits robust performance, we need only verify $\Gamma(\omega) < 1$ (0 dB) is satisfied at all frequencies.

4.3 Design Constraints

The sensitivity, S, and complementary sensitivity, T, functions cannot both be made arbitrarily small at the same frequency due to the relation $S + T = 1$. This leads to primary "design constraint". Assuming $|W_3| > |W_1| > 1$ then $1 < |W_1| = |W_1(S + T)| < |W_1S| + |W_3T|$, so a necessary condition for the robust performance and stability condition, Eq. (2.6), to be satisfied is that the weighting functions W_1 and W_2 not both be greater than 1 at any frequency. This provides a clear *a priori* means of determining the conservativeness of a given design problem, i.e. whether there exists any controller which satisfies the constraints of the problem.

For internal stability, neither right half plane (RHP) poles nor zeros may be canceled by the compensator; therefore, the sensitivity functions are constrained at the locations of RHP zeros (z_i) and RHP poles (p_i), Eq. (4.2).

$$S(z_i) = (1 + L(z_i))^{-1} = 1 \quad T(z_i) = 1 - S(z_i) = 0$$

$$S(p_i) = (1 + L(p_i))^{-1} = 0 \quad T(p_i) = 1 - S(p_i) = 1 \tag{4.2}$$

These conditions are known as "interpolation constraints" and the designer must be careful when performing loop-shaping directly with closed-loop functions that these constraints are satisfied by the proposed loop shape; otherwise, RHP pole/zero cancellations will be introduced. Additional interpolation constraints may also result from the performance requirements of the system; such as allowable error at a specified frequency.

Other important design constraints may be derived from the maximum modulus theorem which states that a function, $F(s)$, which is analytic in some connected open region of the complex plane, $s \in \Omega$, does not attain its maximum at an interior point of that region. Taking this region to be the entire RHP, a condition on W_1 is given by Eq. (4.3).

$$|W_1(z)| = |W_1(z)S(z)| \leq \sup_{\text{Re}(s) \geq 0} |W_1(s)S(s)| = ||W_1 S||_\infty \tag{4.3}$$

So a necessary condition for robust performance is $|W_1(z)| < 1$. In other words, the sensitivity weighting function, W_1, which is typically monotonically decreasing due to low frequency performance requirements, must roll-off before the additional phase lag contributed by any RHP zeros becomes significant. This implies that RHP zeros impose an *upper limit* on achievable closed-loop bandwidth. A similar condition holds for RHP poles, Eq. (4.4).

$$|W_3(p)| = |W_3(z)T(p)| \leq \sup_{\text{Re}(s) \geq 0} |W_3(s)T(s)| = ||W_3 T||_\infty \tag{4.4}$$

In this case, in order to achieve robust stability, $W_3(p) < 1$, and since W_3 typically increases with frequency, this condition implies that RHP poles impose a *lower limit* on the required bandwidth of the system.

It will be demonstrated that a very useful feature of the CRCBode approach is that all of these interpolation constraints appear automatically in the forbidden regions if the performance

and uncertainty weighting functions are chosen appropriately.

4.4 Non-Minimum Phase Systems: Example

Consider the following simple non-minimum phase plant with a single RHP zero:

$$P(s) = \frac{s - 2}{(s + 2)(s + 4)} \tag{4.5}$$

The performance specifications for this example design problem are:

1. Bandwidth = 1 Hz

2. Maximum allowable sensitivity, $S_{\text{max dB}} = 10$ dB (i.e. max disturbance amplification at any frequency)

3. Multiplicative uncertainty at DC, $\Delta_{DC} = 0.1$

4. Desired system type = 1 (i.e. can track step disturbance with zero steady-state error)

5. Desired roll off rate = 2 ($\times 20$ dB/dec)

Eqs. (4.6) and (4.7) provide simple general formulae for the performance, W_1, and uncertainty, W_3, weighting functions. Fig. 4.1 shows a plot of these weighting functions based on the requirements as stated above. Care must always be taken to verify that the selected weights are indeed sufficient for the particular application.
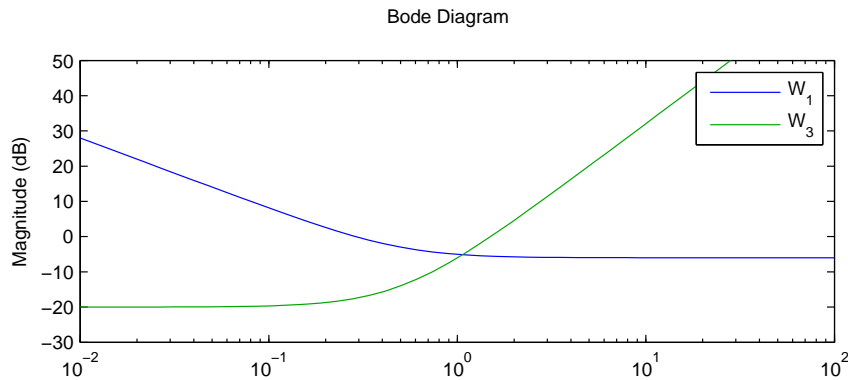
Figure 4.1: Performance, $W_1 = (0.5s+1.6)/s$, and uncertainty, $W_3 = (0.1s^2+0.8s+1)/40$, weighting functions.

$$W_1(s) = 10^{-S_{\text{max dB}}/20} \left(\frac{s + bw}{s} \right)^{type} \tag{4.6}$$

$$W_3(s) = \Delta_{DC} \left(\frac{s + bw}{bw} \right)^{rate} \tag{4.7}$$

We first consider the requirement of zero steady-state error for a step disturbance. Applying the final value theorem to the transfer function from disturbance to error yields, $S(0) = (1 + P(0)C(0))^{-1} = 0$, and thus the interpolation constraint on the controller is $C(0) = \infty$, i.e. it must include a pure integrator. We therefore select the initial proposed controller, $C_1 = 1/s$, the CRCBode diagram for this choice is shown in Fig. 4.3. Unfortunately, this controller destabilizes the nominal closed-loop system since the roots of $1 + C_1(s)P(s)$ are approximately $\{0.2, -3 \pm 0.8j\}$.

It is well known that the root-locus diagram provides a convenient method for determining the correct gain for a given controller structure. Fig. 4.2 shows the root-locus diagram for $kC_1(s)P(s)$ for both positive and negative controller gains. The branch corresponding to the RHP zero is trapped in the RHP for negative feedback ($k > 0$ solid), but can be brought into the LHP with positive feedback ($k < 0$ dashed).
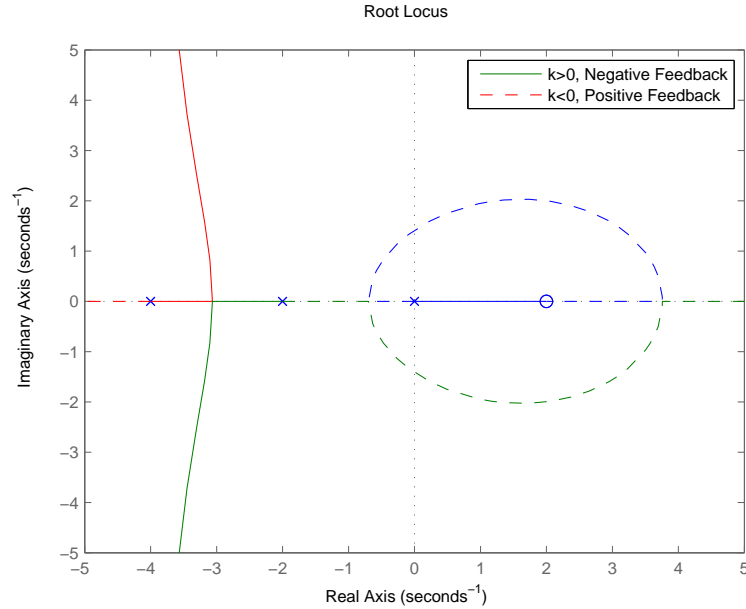
Figure 4.2: Root-locus diagram showing both positive and negative values of controller gain ($k > 0$ dashed, $k < 0$ solid) for a non-minimum phase plant.

For this system, nominal closed-loop stability may be achieved simply by changing the sign of the controller gain. Comparing the CRCBode plots for $C_1 = 1/s$, Fig. 4.3, and $C_2 = -1/s$, Fig. 4.4, illustrates a common difficulty of CRCBode and other robust H_∞ design methods: the robust stability metrics, e.g. $|W_3 T|$, indicate only the "distance" to the critical -1 point without regard to any encirclements thereof, and therefore, the forbidden regions may be misleading if the nominal closed-loop system is not stable. To address this problem, we introduce an alternative approach based on the Youla parametrization.
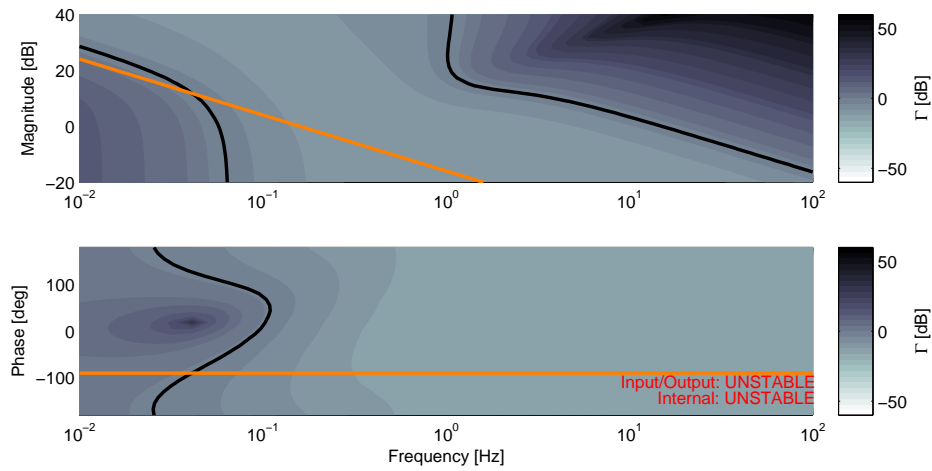
Figure 4.3: CRCBode plot for $C_1 = \frac{1}{s}$.
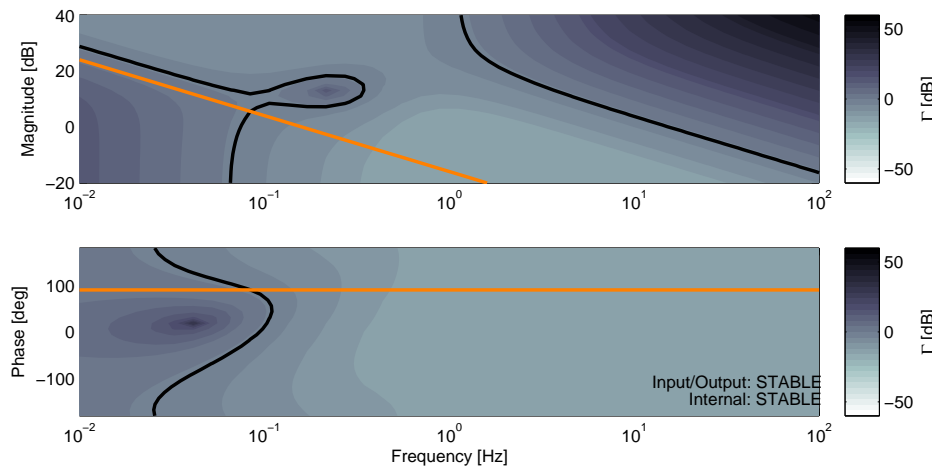
Figure 4.4: CRCBode plot for $C_2 = -\frac{1}{s}$.

66

4.5 CRCBode Approach and Comparison

For this reason, the (input/output and internal) stability of the nominal system is always computed explicitly and displayed on the CRCBode diagrams. In any case, a stabilizing controller for the nominal system must be obtained prior to the robust optimization steps, either manually, e.g. using root-locus or Nyquist considerations, or automatically using the Youla parametrization, as in standard H_∞ theory.

Once nominal internal stability has been achieved, the CRCBode iterative loop-shaping design process may continue. Generally, we proceed from low to high frequencies, cascading compensators to eliminate any intersections of the controller's frequency response with the forbidden regions on the CRCBode magnitude and phase diagrams.

We note here that since we are designing directly on C, if all forbidden regions are avoided and no RHP pole/zero cancellations are introduced, then the system will maintain internal stability and the other interpolation constraints $S(z) = 1$ and $T(z) = 0$ will automatically be satisfied.

In Fig 4.4, there is a large intersection of the controller frequency response with the low frequency forbidden region due to inadequate loop gain. We may directly read off the required gain increase on the CRCBode magnitude plot to avoid this low frequency constraint, i.e. $k = 10^{(29-24)/20} \approx 2$. The CRCBode plot for $C_3 = -2/s$ is given in Fig. 4.5.
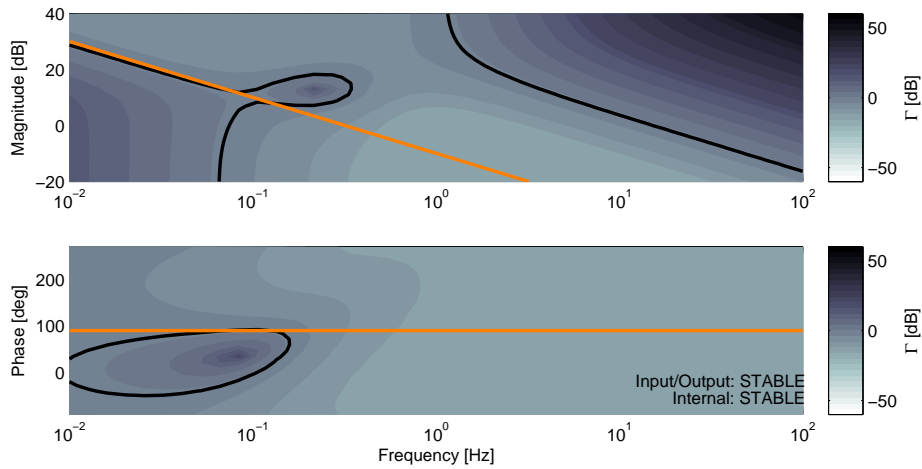
Figure 4.5: CRCBode plot for $C_3 = -\frac{2}{s}$.

There are now intersections near the cross-over frequency, indicative of an insufficient phase margin. As with minimum phase systems, a lead compensator with unity DC gain (to preserve the performance bounds) typically can be used to alleviate this problem. Here we find success with an asymmetric lead compensator structure [28], Eq. (4.5), with $2\phi_c = 80°$ at $\omega_c = 2\pi$ rad/s, $\zeta_z = 1$, $\zeta_p = 0.7$, and $\delta = 0$.

$$C_{aclead}(s) = \frac{\omega_p^2}{\omega_z^2} \frac{s^2 + 2\zeta_z\omega_z s + \omega_z^2}{s^2 + 2\zeta_p\omega_p s + \omega_p^2} \tag{4.8}$$

$$\omega_z = \omega_c \left(-\zeta_z \tan(\phi_c - \delta) + \sqrt{\zeta_z^2 \tan^2(\phi_c - \delta) + 1} \right)$$

$$\omega_p = \omega_c \left(\zeta_p \tan(\phi_c + \delta) + \sqrt{\zeta_p^2 \tan^2(\phi_c - \delta) + 1} \right)$$

where ω_c is the frequency (not necessary of maximum phase) where the phase contribution is $2\phi_c$, and $|\delta| < 90° - |\phi_c|$ is the altering skew angle.
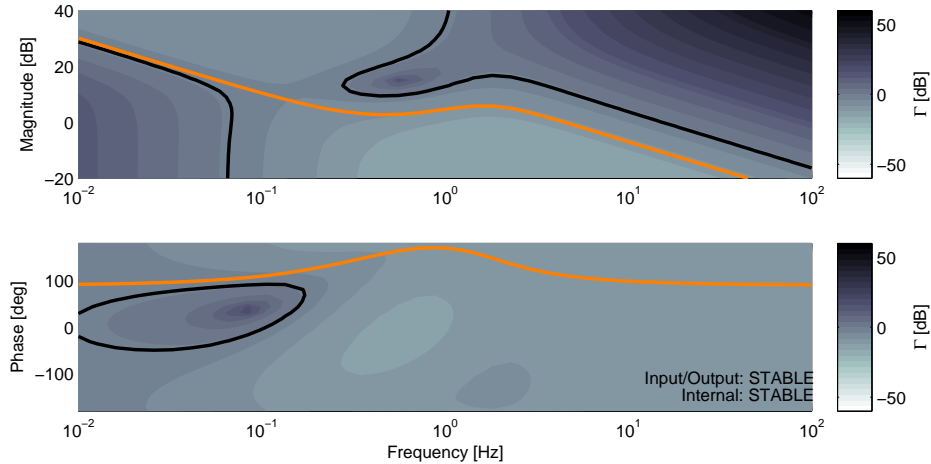
Figure 4.6: CRCBode plot for $C_4 = -\frac{2}{s} \frac{14.04s^2 + 82.26s + 120.5}{s^2 + 15.37s + 120.5}$.

Since the system is stable and all forbidden regions are avoided, the loop-shaping process could be stopped at this point; however, Fig. 4.6, suggests that the robustness can be further optimized. Increasing the controller gain from 2 to 3 lowers the maximum Γ (i.e. $||PC||_\infty$) from -1.06 dB to -3.10 dB and yields a gain margin of $G_m = 8.3$ dB and phase margin $P_m = 60°$, Fig. 4.7. This concludes the CRCBode design process for this non-minimum phase plant.
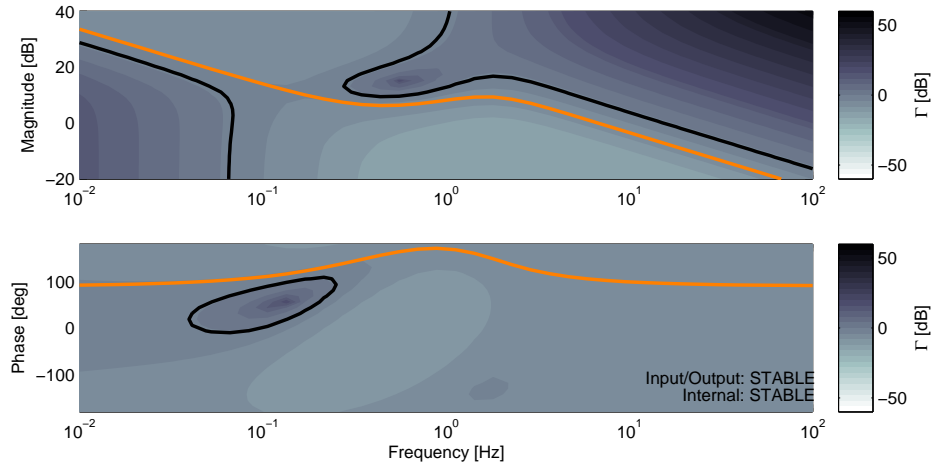
Figure 4.7: CRCBode plot for $C_5 = -\frac{3}{s}\frac{14.04s^2+82.26s+120.5}{s^2+15.37s+120.5}$.

4.6 Youla Parametrization for Stable Non-Minimum Phase Systems

This idea is based on the internal model control (IMC) principle in which a controller $Q(s)$ is designed to act on the error between the plant output and the output of an internal nominal plant model, cf. Fig. 4.8. For open-loop stable systems, the Youla parameter is defined as in Eq. (4.9).
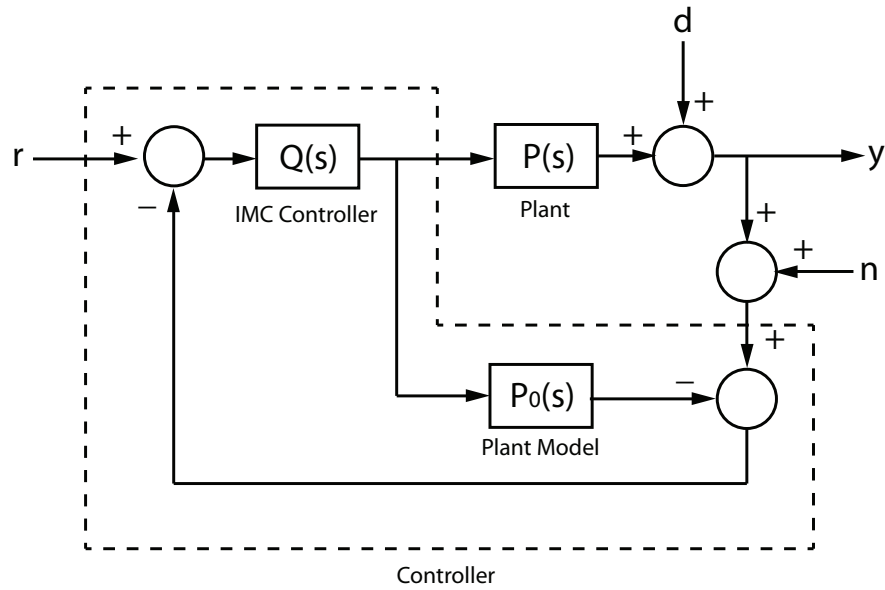
Figure 4.8: Internal model control structure. Q(s) is equivalent to the Youla parameterization of all stabilizing controllers for this system.

$$Q(s) \overset{\text{def}}{=} \frac{C(s)}{1 + P(s)C(s)} \qquad (4.9)$$

It is straightforward to show that $C = Q/(1 - PQ)$, $S = 1/(1 + PC) = 1 - PQ$, and $T = 1 - S = PQ$. Since all three sensitivity functions are linear functions of Q, any stable rational Q ensures *internal* stability (i.e. for all input/ouput signals) in the loop. Q is said to parameterize all stabilizing controllers for this system.

Loop-shaping design is much simpler using Q since closed-loop stability is automatically obtained if a stable Q is selected. There is no need to consider 0 dB cross-over, and so on. Unfortunately this potentially comes at the expense of increased controller complexity. Here, we introduce a new augmented Bode plot known as the QBode which facilitates this direct Q loop-shaping process by showing the $Q(j\omega)$ frequency response and corresponding forbidden regions, but which is otherwise exactly analogous to the CRCBode approach. Returning now to the non-minimum phase example, Eq.(4.5), since in general, any stable proper function may be selected, we choose for the first proposed Youla iteration, $Q_1 = 1/(s + 1)$.
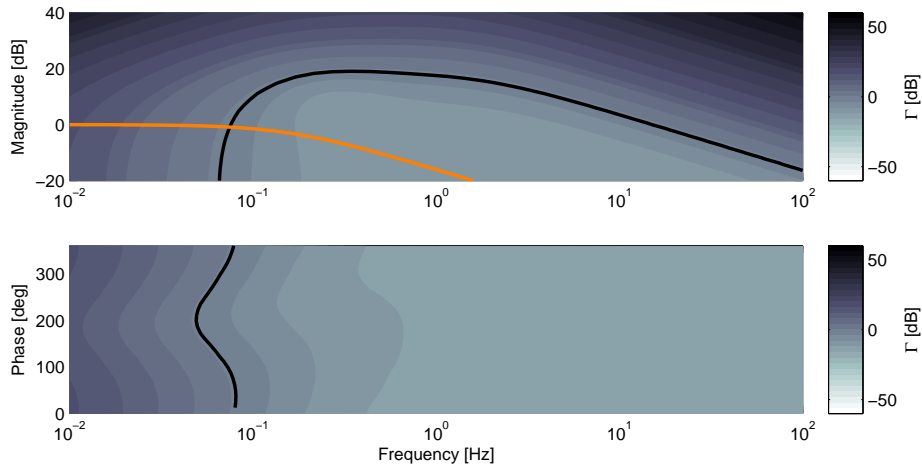
Figure 4.9: QBode plot with positive DC gain, $Q_1 = \frac{1}{s+1}$.
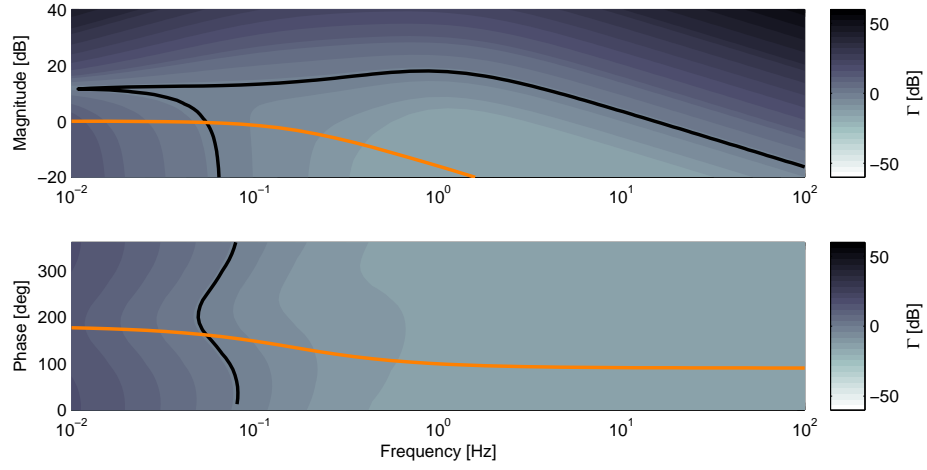
Figure 4.10: QBode plot with negative DC gain, $Q_1 = \frac{-1}{s+1}$.
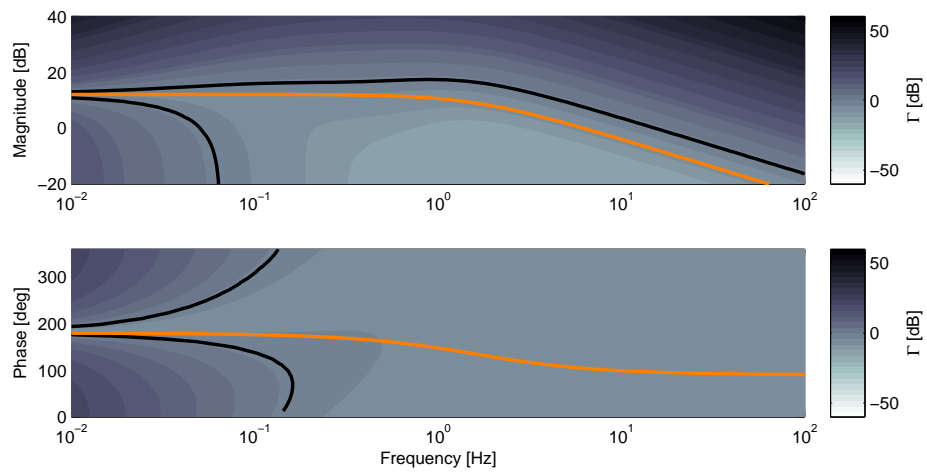
Figure 4.11: QBode plot for $Q_2 = \frac{-40}{s+10}$.

As with C, there are certain interpolation constraints on Q due to the specifications of the problem. In this case the requirement of zero steady-state error for a step disturbances means that $S(0) = 1 - P(0)Q(0) = 0$ and since $P(0) = -1/4$, we have the constraint that $Q(0) = -4$.

The low-frequency forbidden region on the QBode plot for Q_1, Fig. 4.9, covers the entire magnitude and phase axes, strongly suggesting that no Q with this sign will satisfy the constraints. However the QBode plot for $-Q_1$, Fig. 4.10 shows clearly that a DC Gain of $4 \approx 12$ dB is the only choice that satisfies the requirements.

This example illustrates a principal advantage of the Robust Bode approaches. The interpolation constraints appear automatically in the forbidden regions without the need for explicit evaluation by the designer if the weighting functions have been chosen to accurately represent the performance and uncertainty requirements of the system. However, just as it is important to get the correct sign of the controller prior to the loop-shaping process, it is equally important to get the correct sign of Q (not necessarily the same as C). Unfortunately phase perturbations of +/-180 deg on the robust bode plots do not yield the desired information since phase and magnitude perturbations are independently evaluated, so for instance since a controller gain of $k = 1$ is used to construct Fig. 4.9, $k = -1$ is available but not $k = -4$. The simplest approach is to just evaluate CRCBode plots for both positive and negative gains as done here.

To further optimize robustness, we may increase the cut-off frequency to $Q_2 = -40/(s + 10)$ making sure to keep the DC gain at -4. This reduces the maximum Γ from -0.2 dB for Q_1 to -3.3 dB for Q_2, Fig. 4.11.

We note here that though the cut-off frequency of Q has been increased by a factor of 10 to decrease Γ and improve robustness, the 0 dB cross-over frequency of the loop $L = PC$ and the closed-loop bandwidth, do not change appreciably. This is a result of the upper bandwidth limit imposed by the RHP zero. Any attempt to increase the cross-over frequency beyond the RHP zero, causes a peaking of the sensitivity functions which leads to instability. The Q parameterization prevents this instability, and thus constrains the controller bandwidth. The related constraint on the sensitivity weighting function $|W_1(z)| < 1$, is investigated in Figs. 4.13-4.16, for weighting functions intended to provide increasing closed loop bandwidth to the system.

The controller corresponding to the final optimized Youla parameterization may be computed directly, Eq. (4.10).
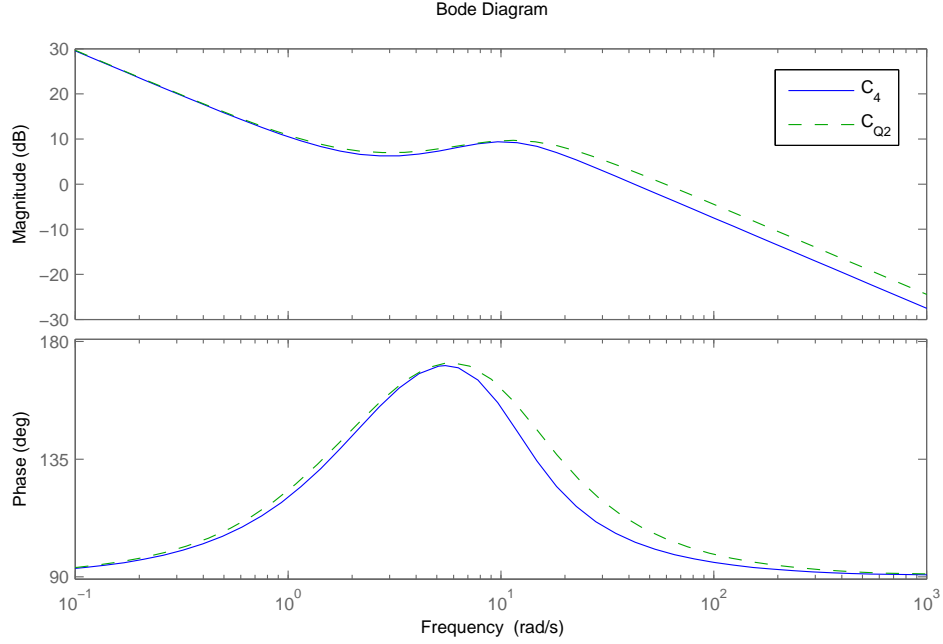
Figure 4.12: Comparison of controllers designed using CRCBode and QBode approaches.

$$C_Q(s) = \frac{Q(s)}{1 - P(s)Q(s)} = \frac{-40}{s} \frac{s^2 + 6s + 8}{s^2 + 16s^2 + 108s} \tag{4.10}$$

The weighting functions in Fig. 4.15 and Fig. 4.16 both violate the design constraint of this non-minimum phase plant, $|W_1(2)| < 1$. As a result, we observe that the forbidden regions span the entire magnitude and phase axes indicating that no controller exists satisfying these requirements. However, within the forbidden regions, the contours are similar and suggest how one may scale the weighting functions to yield a feasible problem. This additional information is notably absent in automated H_∞ controller synthesis methods, and often when the algorithm fails, it is not at all clear how to resolve the issue.
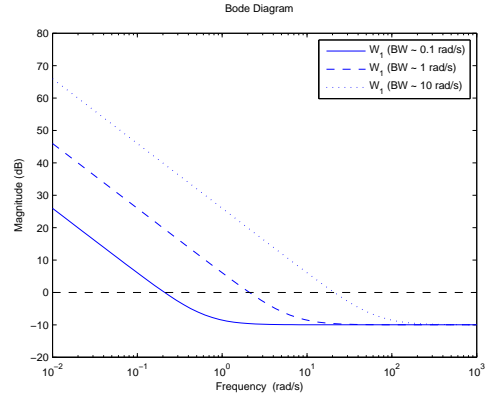
Figure 4.13: Performance (sensitivity) weighting functions with different bandwidths.
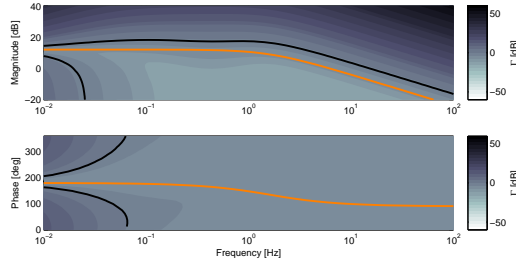
Figure 4.14: QBode for W_1 (BW= 0.1 rad/s) and $Q = \frac{-40}{s+10}$.
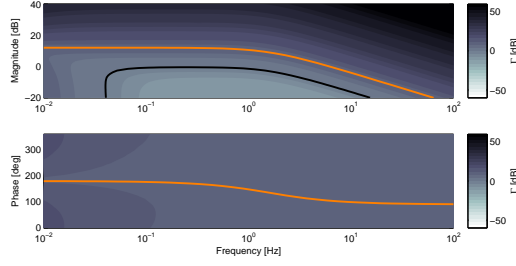
Figure 4.15: QBode for W_1 (BW= 1 rad/s) and $Q = \frac{-40}{s+10}$
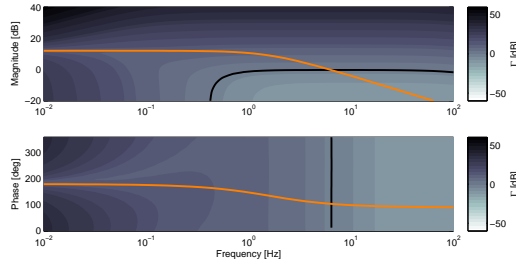
Figure 4.16: QBode for W_1 (BW= 10 rad/s) and $Q = \frac{-40}{s+10}$

The CRCBode plot for C_Q is shown in Fig. 4.17. Since all forbidden regions are avoided by the Youla parameter $Q(s)$ on the QBode plots, it must be the case that $C_Q(s)$ also avoids the forbidden regions on the CRCBode plots.

Interestingly, for this simple example, C_Q consists of the cascade of a pure integrator and an asymmetric complex lead compensator [28], which is a quite typical choice when loop-shaping design is performed directly on C. In general, however, controllers generated from the Q parameterization are significantly more complex than compensators determined through direct C loop-shaping[1].
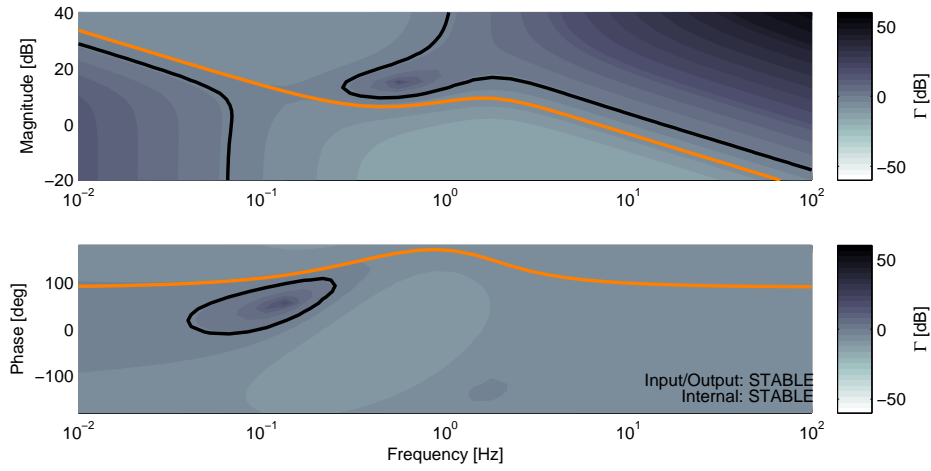
Figure 4.17: CRCBode plot for $C_Q = \frac{-40}{s} \frac{s^2+6s+8}{s^2+16s^2+108s}$.

4.7   3DQBode

Though Q design simplifies stability considerations, it introduces an additional complication due to the sensitivity interpolation constraint. Specifically for open-loop stable systems the Youla parameter is given by, $Q = C(1 + PC)^{-1}$, and consequently the sensitivity function equals, $S = (1 + PC)^{-1} = 1PQ$. Therefore, in order for the performance interpolation constraint $S(0) = 0$, to be met the Youla parameter must exactly satisfy $Q(0) = 1/P(0) = -4$.

---

[1]When there are no pole/zero cancellations, the order of C_Q is the sum of the orders of P and Q.

Since generally, any stable proper transfer function may be chosen, it is reasonable to select, $Q_0 = 1/(s + 1)$. We see immediately, however, that not only does this choice not satisfy the interpolation constraint $Q_0(0) = 1/ = -4$, but also that the perturbation to Q_0 to reach this value requires a simultaneous magnitude and phase perturbation. In particular the phase perturbation must be $(n + 1)180^o$ with n any integer.

Now this presents a problem for the standard robust bode approaches since they only show two particular slices of the perturbation space, and in this case neither slice contains the required combined of magnitude and phase perturbations. As a result the forbidden regions occupy the entire magnitude and phase axes, as shown in Fig. 4.9, suggesting (erroneously) that no simple controller can be selected to meet the performance requirements.

In the original investigation of this problem, the root-locus plot was employed to quickly ascertain the fact that the sign of the controller simply needed to be reversed and the gain adjusted to meet the performance constraint; however, it would be useful if this auxiliary step was not required, and in fact, the 3DQBode plot provides exactly this insight. As can be seen in Fig. 4.18, the forbidden boundary surface now exactly constrains $Q(0)$ to a magnitude of $4 = 12$dB and phase of -180° as needed.
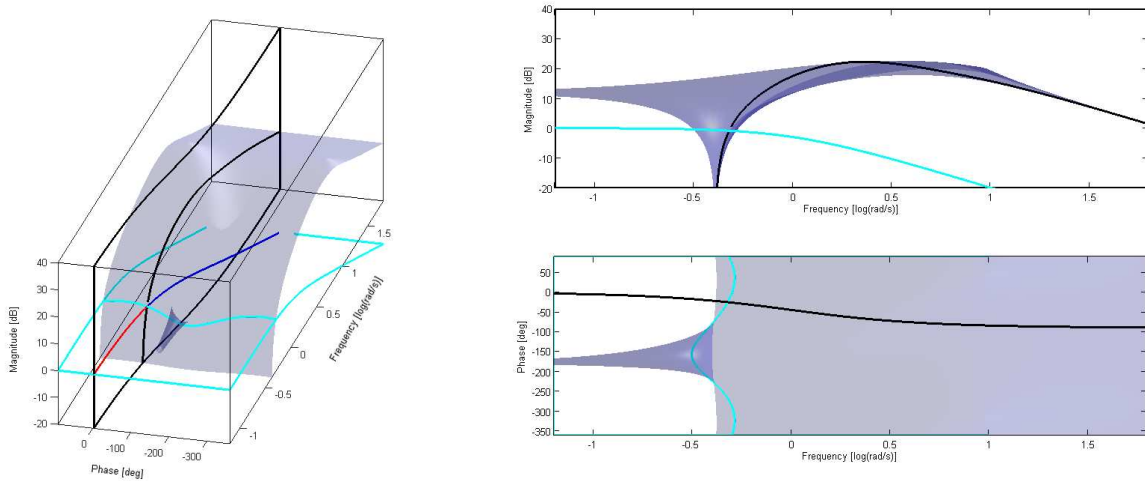
Figure 4.18: 3DQBode plot showing forbidden boundary surface resulting from sensitivity interpolation constraint.

4.8 Youla Parametrization for Unstable and Non-Minimum Phase Systems

In the previous sections we examined the Youla parametrization for open-loop stable plants, in which case all internally stabilizing controllers are given by $K(s) = Q/(1 - PQ)$ with $Q(s)$ any stable transfer function. As we shall show, this result is actually a specific instance of a more general parametrization applicable to both stable and unstable plants. This general formulation is somewhat more complicated and requires the use of so called matrix coprime factorizations as discussed in the following.

For SISO stable or unstable plants, the Youla parametrization of all stabilizing controllers is provided in (4.11).

$$K(s) = \frac{X(s) + M(s)Q(s)}{Y(s) - N(s)Q(s)} \tag{4.11}$$

where $Q(s)$ is again any stable transfer function, and $N(s)$ and $M(s)$ are stable transfer functions representing a *right coprime factorization* of the plant, $P(s)$, as given in (4.12). The stability of $N(s)$ and $M(s)$ requires that all unstable zeros of $P(s)$ must be contained in the zeros of $N(s)$ and all the unstable poles of $P(s)$ must be in the zeros of $M(s)$.

$$P(s) = N(s)M(s)^{-1} \tag{4.12}$$

The transfer functions $N(s)$ and $M(s)$ are said to be *coprime* if and only if they are stable and have no common finite or infinite zeros in the CRHP. Equivalently, it can be shown that $N(s)$ and $M(s)$ are coprime if and only if there exists two other stable rational functions, $X(s)$ and $Y(s)$, which satisfy the Bezout identity (4.13) [10].

$$NX + MY = I \tag{4.13}$$

Recalling the generalized Nyquist Stability Theorem, the closed-loop system with $P(s) = N(s)/M(s)$ and $K(s) = X(s)/Y(s)$ is internally stable if and only if:

(i) The characteristic polynomial has no zeros in the closed right half-plane (CRHP).

(ii) There are no CRHP pole/zero cancellations between the plant and controller.

Using the controller parametrization (4.11), and the plant factorization (4.12), the characteristic polynomial, assuming negative feed-back, is given by (4.14).

$$NX + MY = N(X + QM) + M(Y - NQ) = NX + MY = I \qquad (4.14)$$

This characteristic polynomial, equal to identity by (4.13), clearly has no CRHP zeros; therefore, part (i) of the Nyquist Theorem is satisfied.

In order for the controller to cancel an unstable pole of the plant $M(s)$ and $X(s)$ would need a common zero, z_0. Likewise, in order for the controller to cancel a non-minimum phase zero of the plant, $N(s)$ and $Y(s)$ would need a common zero. Neither of these are allowed since it would violate the Bezout identity (4.13) as shown in (4.15).

$$N(z_0)X(z_0) + M(z_0)Y(z_0) = 0 \neq I. \qquad (4.15)$$

Therefore, part (ii) of the Nyquist Theorem is also satisfied, and the controller parametrization given in (4.11) is indeed sufficient to generate an internally stabilizing controller for the plant. The fact that all internally stabilizing controllers may be expressed in this form for some stable $Q(s)$ (i.e. the necessity of the parametrization) may also be proven, but for this we refer the reader to [17].

Again using the controller parametrization, (4.11), with negative feed-back, the sensitivity and complementary sensitivity functions may be expressed as, (4.16) and (4.17) respectively, which are both affine functions of the Youla parameter, $Q(s)$.

$$S = M(Y - NQ) \qquad (4.16)$$

$$T = N(X + MQ) \qquad (4.17)$$

Finally, note that if the plant is open-loop stable, then we may choose $N(s) = P(s)$, $M(s) = I$, $X(s) = 0$, and $Y(s) = I$ which satisfies the identity (4.13). In this case, (4.11) reduces to (4.18), which is exactly the parametrization introduced previously for stable plants, and the sensitivity

functions reduce to the simple forms in (4.19).

$$K(s) = \frac{X + MQ}{Y - NQ} = \frac{Q}{I - PQ} \tag{4.18}$$

$$S = M(Y - NQ) = I - PQ, \qquad T = N(X + MQ) = PQ \tag{4.19}$$

4.8.1 Computing Coprime Factorizations

Obtaining a coprime factorization of the plant itself is not too challenging: simply divide the numerator and denominators by a common stable polynomial, e.g. $(s + 1)^k$ where k is selected equal to the relative degree of the plant. For example, $P(s) = 1/(s - 1) = N(s)M(s)^{-1} \Rightarrow N(s) = 1/(s + 1)$, $M(s) = (s - 1)/(s + 1)$. However, finding $X(s)$ and $Y(s)$ to satisfy (4.13) is more difficult. A manual polynomial method based on Euclid's algorithm is presented in [17]; however, it is cumbersome and not generalizable to MIMO systems.

Somewhat surprisingly, MATLAB offers no functionality to compute coprime factorizations directly. Fortunately, coprime factorizations may be generated using straightforward state-space operations as described in the following section. As we shall see, the structure of this state-space formulation actually yields significant insights which will be essential to our subsequent development of the Robust Bode design methods.

A stabilizable and detectable state-space realization of the plant, P(s), is given in (4.20)-(4.21).

$$\dot{x} = Ax + Bu \tag{4.20}$$

$$y = Cx + Du \tag{4.21}$$

A convenient and compact notation for state-space realizations is introduced in (4.22).

$$P(s) = \left[\begin{array}{c|c} A & B \\ \hline C & D \end{array} \right] \stackrel{\text{def}}{=} C(sI - A)^{-1}B + D \tag{4.22}$$

Now consider any real matrix, F, such that $A + BF$ is stable[2], that is F is the solution of any

---

[2]Note that we adopt a positive feedback sign convention here.

state feedback problem, then the closed-loop system dynamics are given by (4.23)-(4.25).

$$\dot{x} = (A + BF)x + Bv \tag{4.23}$$

$$u = Fx + v \tag{4.24}$$

$$y = (C + DF)x + Dv \tag{4.25}$$

Now identify the transfer functions from v to u, and from v to y, given by $M(s)$, (4.27), and $N(s)$, (4.26), respectively.

$$M(s) = \left[\begin{array}{c|c} A + BF & B \\ \hline F & I \end{array} \right] \tag{4.26}$$

$$N(s) = \left[\begin{array}{c|c} A + BF & B \\ \hline C + DF & D \end{array} \right] \tag{4.27}$$

The transfer function for the plant from input, u, to output, y, is thus $P(s) = N(s)M(s)^{-1}$, (4.28).

$$u = M(s)v, \ y = N(s)v \quad \Rightarrow \quad y = P(s)u = N(s)M(s)^{-1}u \tag{4.28}$$

$N(s)$ and $M(s)$ are proper since they have state-space realizations, and they are stable by construction since F is selected so that $A + BF$ has all its eigenvalues in the closed left half-plane. Therefore, $P(s) = N(s)M(s)^{-1}$, in fact represents a right coprime factorization for the plant.

Now choose any real matrix H such that $A + CH$ is stable, that is *solve any state observer problem.* The estimator dynamics are then given by (4.29)-(4.30).

$$\dot{\tilde{x}} = A\tilde{x} + Bu + H(\tilde{y} - y) \tag{4.29}$$

$$\tilde{y} = C\tilde{x} + Du \tag{4.30}$$

where $\tilde{x}$ and $\tilde{y}$ are the state and output estimates respectively. Selecting the input as $u = F\tilde{x} + \mu$,

and identifying μ as the new output, the observer dynamics become (4.31)-(4.32).

$$\dot{\tilde{x}} = (A + HC)\tilde{x} + (B + HD)u - Hy \tag{4.31}$$

$$\mu = u - F\tilde{x} \tag{4.32}$$

Now the transfer function from u to μ (with $y = 0$), $Y(s)$, and from y to μ (with $u = 0$), $X(s)$, may be found to be (4.33) and (4.34) respectively.

$$Y(s) = \left[\begin{array}{c|c} A + HC & B + HD \\ \hline -F & I \end{array} \right] \tag{4.33}$$

$$X(s) = \left[\begin{array}{c|c} A + HC & -H \\ \hline -F & 0 \end{array} \right] \tag{4.34}$$

Therefore, the transfer function of the controller, i.e. the mapping from measured output y to control input u, is given by $K(s) = Y(s)^{-1}X(s)$, (4.35).

$$\mu = X(s)y, \ \mu = Y(s)u \quad \Rightarrow \quad u = K(s)y = Y(s)^{-1}X(s)y \tag{4.35}$$

$X(s)$ and $Y(s)$ are proper and stable by construction. It is easy to verify numerically that a minimal realization of $N(s)X(s) + M(s)Y(s)$ as defined by (4.26),(4.27),(4.34), and (4.33) for any choice of F and H reduces to a static unit gain, thus the Bezout identity, (4.13) is satisfied.

4.8.2 Interpretation of Coprime Parametrizations

It can be shown that all controllers parametrized by (4.11) can be expressed in the form of a linear fractional transformation (LFT), introduced in Ch. 3, in which the Youla parameter, $Q(s)$ is "pulled out" from an observer/state-feedback control structure [10]. A block diagram representation of this configuration is shown in Fig. 4.19.

The observer dynamics (4.31) and the control law (4.32) used in deriving the coprime factorization are restated in (4.36) and (4.37) respectively. The control law is full state feed-back based on the state estimate, $F\tilde{x}$, plus an additional arbitrary input signal μ. Likewise, the observer dynamics are standard, but with an additional term $(B + HD)\mu$ to ensure the observer is driven by the same input as the plant. Controllers having this state feed-back/state observer structure
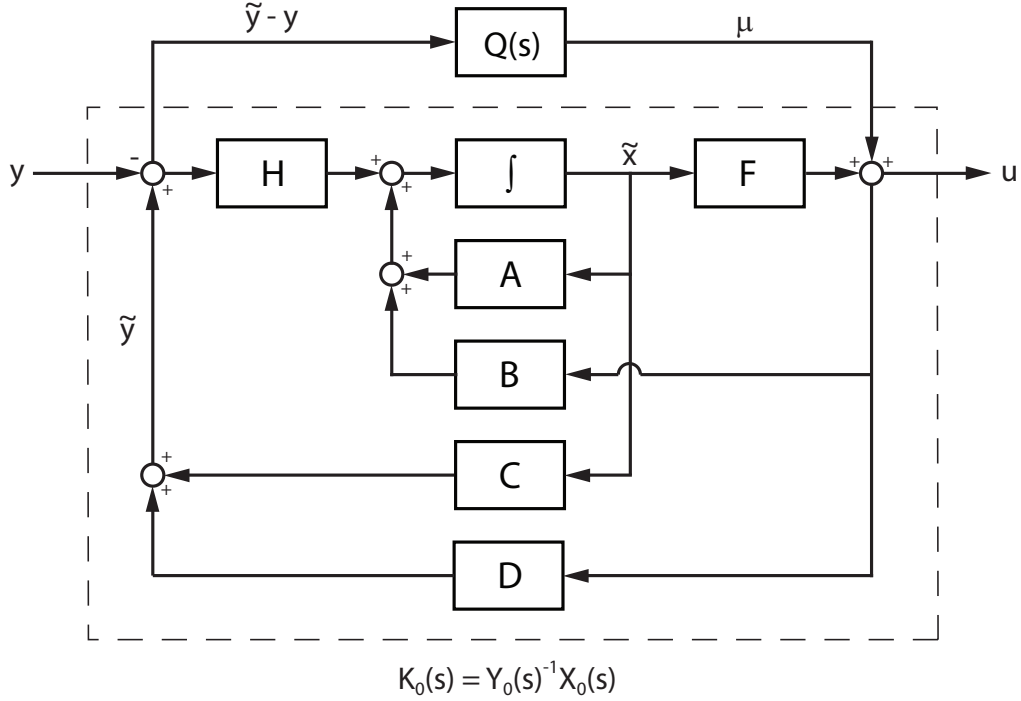
Figure 4.19: Observer based structure of all stabilizing controllers.

are called *observer based controllers*.

$$\dot{\tilde{x}} = (A + BF + HC + HDF)\tilde{x} - Hy + (B + HD)\mu \qquad (4.36)$$

$$u = F\tilde{x} + \mu \qquad (4.37)$$

Comparing the controller structure in Fig. 4.19 with the dynamics in (4.36)-(4.37), it is clear that the additional control input signal must equal $\mu = Q(\tilde{y} - y)$. The Youla parameter acts on the error between the output estimate, $\tilde{y}$, and the measured output, y, just as it did in the "internal model control" representation introduced for stable plants, c.f. Fig. 4.8.

All internally stabilizing controllers, must therefore have the form of an observer/state feedback controller augmented by an arbitrary proper stable transfer function $Q(s)$, as shown in Fig. 4.19. We thus arrive at the conclusion that **all stabilizing controllers are "observer based"** [10].

The results presented in this section were essential to the development of robust control theory. In particular, the state-space formulae for coprime parametrizations allowed the robust frequency-

domain $\|H\|_\infty$-norm minimization objectives to be converted into matrix (Riccati) equation problems, similar to those found in time-domain optimal control theory, for which efficient numerical solutions were available. In fact, there are many interesting connections between robust ($\|H\|_\infty$) control theory and linear-quadratic Gaussian (LQG) optimal control, which for this reason came to be known as H_2 theory. We will only briefly scratch the surface here, but a thorough discussion on this topic may be found in [13].

These results are also quite significant for our own purposes since they provide a framework with which to formalize the Robust Bode design process to general plants, either stable or unstable, minimum or non-minimum phase. Specifically, we may use state-space design techniques, e.g. pole placement or LQG, to design stabilizing controller and observer gain matrices, from which we may compute a coprime factorization and Youla parametrization of the system. The frequency response of this nominal observer based controller is then used to initiate the Robust Bode design process. Loop-shaping design iterations may then be carried out directly on the controller or Youla Robust Bode plot as discussed in the next several sections.

4.8.3 Connection to Optimal LQG Control

In the coprime factorization formulae, (4.26)-(4.27), we are free to choose any controller gain matrix, F, and observer gain matrix, H, which stabilize the closed-loop system, i.e. which place all eigenvalues of $A + BF$ and $A + HC$ in the left half-plane. This same ambiguity was encountered when performing the factorization manually as in $P(s) = 1/(s - 1) = N(s)M(s)^{-1} \Rightarrow N(s) = 1/(s + 1)$, $M(s) = (s - 1)/(s + 1)$, since the common denominator polynomial was arbitrarily selected as $(s + 1)$.

We may formalize this by noting that N and M may share any common stable factor Z as long as Z^{-1} is also stable (i.e. Z must have all its zeros in the CLHP). In fact, this is often used as an alternate definition of coprimeness.

Stabilizing F and H gain matrices may be determined using pole-placement techniques; however, in this case selection of the pole locations is arbitrary. In MATLAB pole-placement may be accomplished using the commands `F = -place(A,B,pc)` and `H = -place(A',C',po)'` where `pc` and `po` are the desired closed-loop system and observer pole vectors respectively.

Though manual selection of the pole locations may sometimes be warranted, poor selection

may lead to adverse effects. For instance, selecting controller poles which are too fast (i.e. too far into the left half-plane) can result in excessively large control signals which saturate actuators. Similarly, choosing observer poles which are too fast can lead to issues with noise sensitivity and/or to unstable controllers [34].

An alternative approach, and the one we will pursue here, is to use linear-quadratic Gaussian (LQG) optimal control theory to generate the controller and observer gains systematically. In particular, a linear-quadratic regulator (LQR) or servo design problem is formulated to select the state feed-back controller gain matrix, F, which minimizes a time-domain integral quadratic cost function via the solution of an algebraic Riccati equation. A Kalman filter design is then used to identify the observer gain matrix, H, which minimizes the variance of the state estimate to white (Gaussian) process and measurement noise.

After obtaining the LQG optimal gains, we then compute the corresponding coprime factorization using (4.26),(4.27),(4.33),(4.34) and LQG controller, $K_{LQG}(s) = Y(s)^{-1}X(s)$. The transfer function of the LQG controller is then used to construct initial Controller (CRCBode) or Youla (QBode) Robust Bode plots. An iterative loop-shaping design procedure may then be performed in order to "robustify" the initial controller by attempting to minimize the robust performance metric, Γ, over all frequencies.

In general, the Robust Bode design process is easier when loop-shaping directly with the Youla parameter (QBode); however, higher-order controllers are typically generated. Loop-shaping directly on the controller (CRCBode), allows for manual controller order reduction, but care must be taken not to destabilize the system. In either case, since the LQG design ensures that the nominal closed-loop system is stable, any ambiguity in the robust metric is avoided, c.f. the non-minimum phase case study.

Therefore, minimizing the robust metric while avoiding the "forbidden regions" on the Robust Bode diagrams, allows us to definitively obtain internally stabilizing controllers which achieve the given robust stability and performance objectives. Furthermore, since we begin the design process with an already "good" (LQG) controller, the difficulty of the loop-shaping is reduced, especially for complicated or unstable/non-minimum phase plants.

Finally, we note that the procedure described here for Robust Bode design is very closely related (in essence identical) to the H_∞ robust controller numerical synthesis algorithms currently

available. To see why this is so, consider the standard "2-Ricatti" state-space solution introduced by Glover and Doyle [13], which is the default method in the MATLAB robust controller synthesis procedure, `hinfsyn( )`, used throughout this work.

In this method, all stabilizing (admissible) controllers are sought such that the $\|H\|_\infty$-norm of the closed-loop sensitivity function from exogenous inputs to regulated outputs is strictly less than some value, $\|T_{zw}\|_\infty < \gamma$. The main result of the Glover-Doyle algorithm is that an admissible controller exists if and only if the unique stabilizing solutions of two Ricatti equations are positive definite $X_\infty \geq 0$ and $Y_\infty \geq 0$, and the spectral radius of the product satisfys the inequality, $\rho(X_\infty Y_\infty) < \gamma^2$. The exact form of these Riccati equations is omitted here for brevity; however, it is sufficient to note that they include terms proportional to γ^{-2}.

It can be shown, that in the limit as $\gamma \to \infty$, the problem reduces to the same Riccati equations arising in LQG optimal control, in other words as $\gamma \to \infty$, $H_\infty \to H_2$, and $K_\infty \to K_{LQG}$ [13]. The automated synthesis routine begins with a very large value of γ which is reduced using a bisection technique until an admissible controller no longer exists, thus generating a (sub-optimal) robust controller.

In essence, **numerical robust synthesis algorithms mirror the manual robust controller design procedure introduced here: linear-quadratic Gaussian initiated iterative loop-shaping using the Robust Bode diagrams.** We now demonstrate this general LQG based Robust Bode approach to controller design by examining an open-loop unstable and non-minimum phase case study: The inverted pendulum.

4.9   Case Study: Inverted Pendulum

The inverted pendulum is a classic example used when introducing control concepts for open-loop unstable plants. The popularity of the inverted pendulum system may be attributed to its intuitive familiarity (consider balancing a broomstick in one's hand), the relative simplicity of its mathematical model, and the ease with which stabilizing controllers may be designed and implemented in a classroom or laboratory setting. Rather than simply a "toy" problem, many challenging real world engineering problems exhibit inverted pendulum like behavior, including attitude control of rockets at take-off [35] and the walking dynamics of bipedal robots [32].
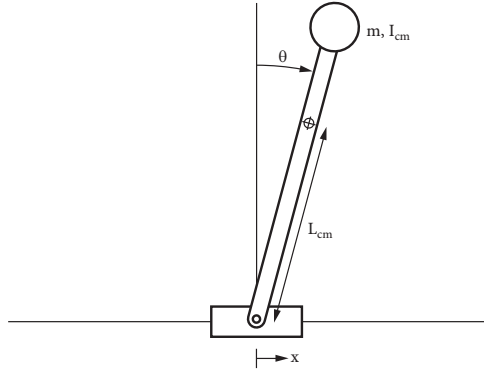
Figure 4.20: Schematic of inverted pendulum system.

4.9.1   Inverted Pendulum: Modeling Dynamics

The standard inverted pendulum system considered here, shown in Fig. 4.20, consists of a rigid link with total mass m and moment of inertia, I_{cm}. The length from the pendulum pivot point to the center of mass is L_{cm}. The pivot point is allowed to move along the horizontal axis, x. The objective is to design a feed-back control law such that the link remains balanced in a upright position, $\theta = 0$.

The governing equations of motion for the inverted pendulum may be obtained from the Euler-Lagrange equations for conservative force systems, (4.38).

$$\frac{d}{dt}\left(\frac{\partial \mathcal{L}}{\partial \dot{q}_j}\right) - \frac{\partial \mathcal{L}}{\partial q_j} = 0 \tag{4.38}$$

where $\mathcal{L} = T - V$ is the Lagrangian function with T and V the kinetic and potential energies respectively. The kinetic energy for this system consists of translational and rotational terms, as shown in (4.39).

$$T = \frac{1}{2}m\dot{\bar{x}}_{cm}^2 + \frac{1}{2}I_{cm}\dot{\theta}^2 \tag{4.39}$$

The 2D position of the pendulum center of mass is given in (4.40) and its velocity found through explicit differentiation as in (4.41).

$$\bar{x}_{cm} = [x + L\sin\theta, \quad L\cos\theta] \tag{4.40}$$

$$\dot{\bar{x}}_{cm} = [\dot{x} + L\cos\theta\dot{\theta}, \quad -L\sin\theta\dot{\theta}] \tag{4.41}$$

Substituting (4.41) into (4.39)

$$T = \frac{1}{2}m\left[(\dot{x} + L\cos\theta\dot{\theta})^2 + (L\sin\theta\dot{\theta})^2\right] + \frac{1}{2}I_{cm}\dot{\theta}^2 \tag{4.42}$$

The potential energy is determined simply by the height of the center of mass, as in (4.43).

$$V = mgy_{cm} = mgL\cos\theta \tag{4.43}$$

where g is of course the acceleration due to gravity. The Lagrangian is thus given by (4.44).

$$\mathcal{L} = \frac{1}{2}m\left[(\dot{x} + L\cos\theta\dot{\theta})^2 + (L\sin\theta\dot{\theta})^2\right] + \frac{1}{2}I_{cm}\dot{\theta}^2 - mgL\cos\theta \tag{4.44}$$

We may now apply the Euler-Lagrange equation (4.38) in which the q_j are generalized coordinates representing the degrees of freedom in the system. In this case, the only free coordinate is $q = \theta$, since the position of the pendulum base, $x(t)$, is determined via the feed-back control law.

Taking the partial derivative of the Lagrangian (4.44) with respect to $\dot{\theta}$ and simplifying using the identify $\sin^2\theta + \cos^2\theta = 1$ we obtain (4.45).

$$\frac{\partial\mathcal{L}}{\partial\dot{\theta}} = mL\cos\theta\dot{x} + (I_{cm} + mL^2)\dot{\theta} \tag{4.45}$$

Taking the time derivative of the result yields

$$\frac{d}{dt}\left(\frac{\partial\mathcal{L}}{\partial\dot{\theta}}\right) = mL\cos\theta\ddot{x} - mL\sin\theta\dot{\theta}\dot{x} + (I_{cm} + mL^2)\ddot{\theta} \tag{4.46}$$

Now the partial of $\mathcal{L}$ with respect to θ

$$\frac{\partial \mathcal{L}}{\partial \theta} = -mL \sin \theta \dot{\theta} \dot{x} + mgL \sin \theta \tag{4.47}$$

The equation of motion is then given by (4.48).

$$\frac{d}{dt}\left(\frac{\partial \mathcal{L}}{\partial \dot{\theta}}\right) - \frac{\partial \mathcal{L}}{\partial \theta} = mL \cos \theta \ddot{x} + (I_{cm} + mL^2)\ddot{\theta} - mgL \sin \theta = 0 \tag{4.48}$$

Applying the small angle approximations $\sin \theta \approx \theta$ and $\cos \theta \approx 1$ (or equivalently linearizing about $\theta = 0$) yields the linear differential equation of motion for the inverted pendulum system (4.49).

$$(I_{cm} + mL^2)\ddot{\theta} - mgL\theta = -mL\ddot{x} \tag{4.49}$$

Note that by the *parallel axis theorem* the term $I_{cm} + mL^2$ is the moment of inertia about the pendulum pivot point. Typically, the pendulum rod is assumed mass-less with a point mass located a distance L from the pivot point. In this case, the moment of inertia about the center of mass is $I_{cm} = 0$ and the equation of motion reduces to (4.50).

$$L\ddot{\theta} - g\theta = -\ddot{x} \tag{4.50}$$

Taking the Laplace transform of (4.50), yields the transfer function from pivot positional input to pendulum angle output, (4.51).

$$\frac{\Theta(s)}{X(s)} = \frac{-s^2}{Ls^2 - g} = \frac{-s^2/g}{(\tau s + 1)(\tau s - 1)} \tag{4.51}$$

where the time constant is given by $\tau = \sqrt{L/g}$, and the open-loop system poles by $p_{1,2} = \pm 1/\tau = \pm\sqrt{g/L}$. Note that this model agrees with the one presented in [36], derived using an alternate Newtonian mechanics approach.

Obtaining a state-space realization directly from the linearized system dynamics, (4.50), is rather difficult due to the derivatives of the input signal, x. Various state-space realizations may of course easily be computed, e.g. controllable/observable canonical forms, balanced, modal, etc., but unfortunately, in doing so, the physical meaning of the state variables is typically lost. It is useful, however, to have a realization based on physical states, which we will derive in the following.

Define a new state vector, q (4.52) and identify the input $u = x$ and output $y = \theta$. Now the

inverted pendulum dynamics (4.50) and output equations may be expressed in terms of these new state-variables as in (4.52)-(4.54)[3].

$$q = \begin{bmatrix} \iint \theta(t) dt dt' \\ \int \theta(t) dt \end{bmatrix} \Rightarrow \dot{q} = \begin{bmatrix} \int \theta(t) dt \\ \theta(t) \end{bmatrix} \tag{4.52}$$

$$L\ddot{\theta} - g\theta = -\ddot{x} \quad \Leftarrow \quad \theta = \frac{g}{L} \iint \theta dt dt' - \frac{1}{L} x = \dot{q}_2 = \frac{g}{L} q_1 - \frac{1}{L} u \tag{4.53}$$

$$y = \theta = \dot{q}_2 = \frac{g}{L} q_1 - \frac{1}{L} u \tag{4.54}$$

From these a state-state realization of the pendulum dynamics, similar to controllable canonical form, is obtained as (4.55). It easy to verify that this is a minimal realization since the order of both the state-space and transfer function is 2.

$$P(s) = \begin{bmatrix} A & B \\ \hline C & D \end{bmatrix} = \left[\begin{array}{c|c} \begin{bmatrix} 0 & 1 \\ g/L & 0 \end{bmatrix} & \begin{bmatrix} 0 \\ -1/L \end{bmatrix} \\ \hline \begin{bmatrix} g/L & 0 \end{bmatrix} & -1/L \end{array} \right] = C(sI - A)^{-1} B + D = \frac{-s^2}{Ls^2 - g} \tag{4.55}$$

It must be noted that much of the difficulty encountered here in obtaining a state space realization is due to the fact that the model used for the inverted pendulum system is not complete. In particular, it is assumed that the pendulum base trajectory, $x(t)$, is an arbitrary input to the plant. In reality, this motion would have to be driven by some actuator, for example a servomechanism possessing its own dynamics, which would almost certainly be strictly proper. If these dynamics were explicitly included in the model, then the overall input/output mapping would also be strictly proper, and the state-space realization would be trivial.

For the remaining analysis, we assume the following parameter values: $L = 9.8$ [m] and $g = 9.8$ [m/s^2]. The time constant is therefore given by $\tau = 1$ [s] and the plant transfer function by $P(s) = \Theta(s)/X(s) \approx -0.1s^2/[(s+1)(s-1)]$.

---

[3]Assume zero initial conditions.

4.9.2 Inverted Pendulum: Control Limitations

The linearized inverted pendulum system presented here, (4.55), is both unstable (due to the right half-plane pole) and non-minimum phase (due to the two zeros at the origin). As we have previously discussed, non-minimum phase zeros impose upper limits on achievable bandwidth, and unstable poles impose lower limits on required bandwidth for closed-loop stability. Clearly, these constraints may sometimes conflict, and indeed, it can be shown that as unstable poles and zeros approach each other, the system becomes increasingly difficult to control, i.e. the minimum achievable peak sensitivity increases [18].

If the non-minimum phase zeros are much faster than the unstable poles, then these constraints may not cause any problems. Unfortunately, for the inverted pendulum system, this is not the case, since though the unstable pole may be made arbitrarily slow by increasing the effective length of the rod, the unstable zeros are fixed at $s = 0$ and so continue to complicate the controller design process.

For these reasons, it may be said that the inverted pendulum system represents one of the more difficult classes of systems to control (unstable and non-minimum phase), and it is therefore a good choice to demonstrate the strength and versatility of the Robust Bode design methods.

4.9.3 Inverted Pendulum: Preliminary Frequency-Domain Controller

Before proceeding with the Robust Bode design process, it is instructive to consider an alternate frequency-domain control approach commonly used to stabilize inverted pendulum systems. The plant transfer function, (4.51), has a single unstable pole at $s = 1/\tau$ and two unstable zeros at the origin $s = 0$. If the control law is selected with two poles at the origin to cancel these plant zeros and a single left half plane zero, (4.56), then the closed-loop may be stabilized with appropriate choice of the zero and controller gain, $kz > 10$ with $k > 0$ and $z > 0$. This may be verified directly from the closed-loop sensitivity function, (4.57), or by examining the root-locus diagrams presented in Fig. 4.22 for both slow $z < 1/\tau$ and fast $z > 1/\tau$ controller zero locations.

$$K(s) = \frac{k(s+z)}{s^2} \tag{4.56}$$

$$S(s) = \frac{\Theta(s)}{\Theta_d(s)} = \frac{1}{1 - P(s)K(s)} = \frac{10(s^2 - 1)}{10s^2 + ks + (kz - 10)} \tag{4.57}$$
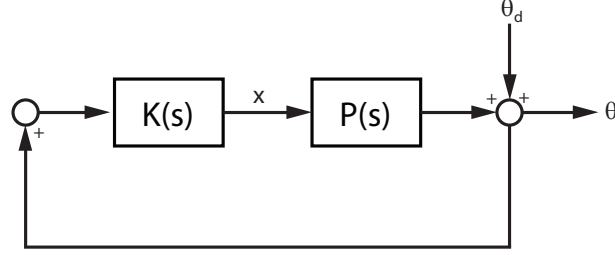
Figure 4.21: Block diagram of linearized inverted pendulum system.

It is often the case for unstable and/or non-minimum phase systems that the sign of the controller is initially unknown; therefore, we adopt the convention of always showing root-loci for both positive $k > 0$ (solid) and negative $k < 0$ (dashed) feed-back gains.

For this system, we find that positive feedback is required since some of the negative feedback loci are trapped in the right half-plane, which of course agrees with physical intuition that the pendulum base must accelerate in the $+x$ direction for positive angular deflections.

(a)   (b)
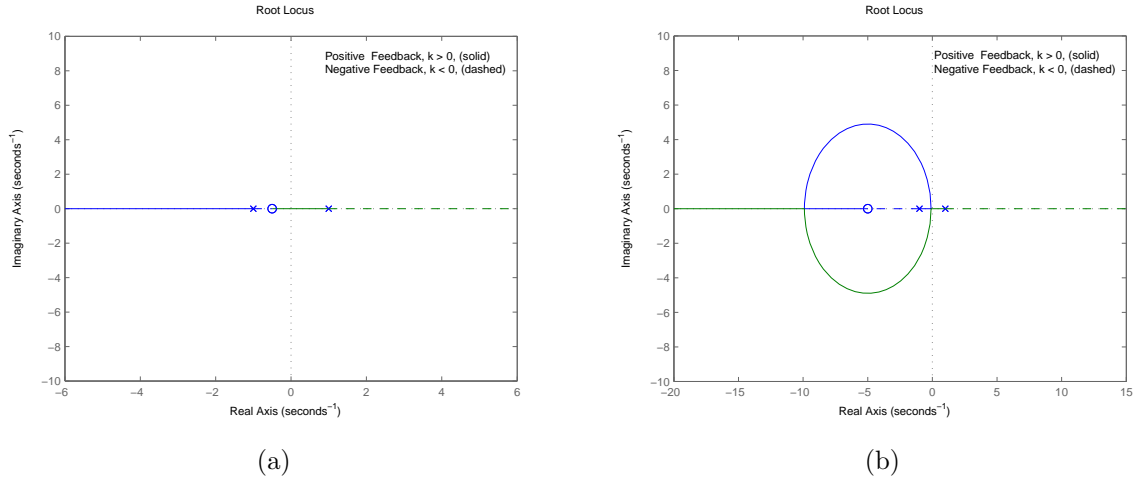
Figure 4.22: Root-locus diagrams for inverted pendulum with "zero-canceling" controller, $K(s) = k(s + z)/s^2$ for (a) slow $z = 0.5 < 1/\tau$ and (b) fast $z = 5 > 1/\tau$ controller zeros. Both may be stabilized with controller gains, $kz > 10$, $k > 0$, and $z > 0$.

This "zero-canceling" control scheme is frequently selected due to it's simplicity; however, inverting non-minimum phase plant dynamics is almost never advisable. As we have previously discussed, any unstable pole/zero cancellations between the plant and controller result in instability of some "internal" signals in the system. In this system, the instability appears at the output of the controller, i.e. the base position, $x(t)$.

The closed-loop transfer function from angular disturbance, θ_d, to base position, x, is given by (4.58), which is unstable independent of gain due to the poles at $s = 0$. The response of both $\theta(t)$ and $x(t)$ due to an impulse disturbance $\theta_d = -0.01\delta(t)$ with $K(s) = 50(s+5)/s^2$ is shown in Fig. 4.23. Though the pendulum angle is stabilized about $\theta = 0$, the base position is unbounded, $\lim_{t\to\infty} x(t) = \infty$ with the "zero-canceling" controller given in (4.56).

Note that if only the pendulum angle were perturbed, then the base position would reach a non-zero steady-state position; however, since the impulse disturbance also excites a non-zero initial angular velocity, the base also obtains a non-zero steady-state velocity carrying it away from the origin eventually "saturating" the actuator.

Figure 4.23: Inverted pendulum system response to impulse disturbance for $K(s) = 50(s+5)/s^2$. The closed-loop system with this controller is not internally stable (x is unbounded).

$$\frac{X(s)}{\Theta_d(s)} = \frac{K(s)}{1 - K(s)P(s)} = \frac{10k(s^3 + zs^2 - s - z)}{s^2(10s^2 + ks + kz - 10)} \tag{4.58}$$

Plants which can be internally stabilized by a stable controller are called *strongly stabilizable*. A stable control law is generally preferable for system integrity reasons, since if a feed-back loop is broken, the output of a stable controller will remain bounded. Not all systems, however, are strongly stabilizable. It is relatively straight-forward to show using the Youla parametrization in (4.11) that a plant is strongly stabilizable if and only if it has an even number of real poles between each pair of real zeros in the closed right half-plane [17].

We find then that the inverted pendulum is not strongly stabilizable, and an unstable controller is required in order to simultaneously stabilize both the pendulum angle, θ, and base position, x.

One choice of internally stabilizing controller is given by (4.59). Note that the stable plant pole is inverted by this controller, which is not necessary but simplifies the analysis a bit.

$$K(s) = \frac{100(s+1)}{(s+0.1)(s-3)} \tag{4.59}$$

The root-locus diagram corresponding to this controller is provided in Fig. 4.24. We see from this diagram that the unstable pole of the compensator is required in order for the root-locus branches in the right half-plane to break away from the real axis, so that they may then be drawn into the left half-plane with appropriate choice of gain, thereby stabilizing the system.
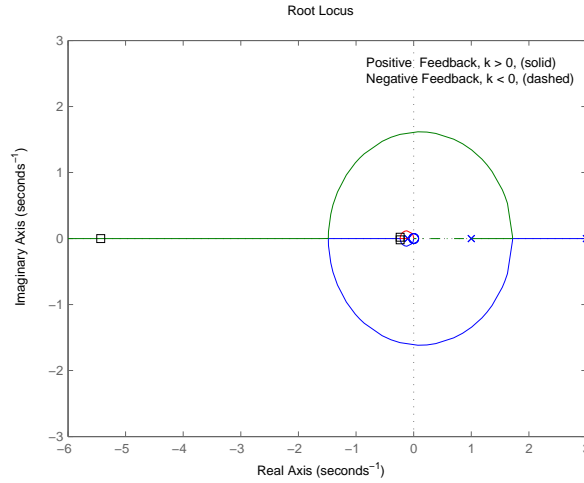
Figure 4.24: Root-locus diagram corresponding to an internally stabilizing controller for the inverted pendulum system, $K(s) = 100(s+1)/((s+0.1)(s-3))$. The squares indicate the location of the stable closed-loop poles for $k = 100$.
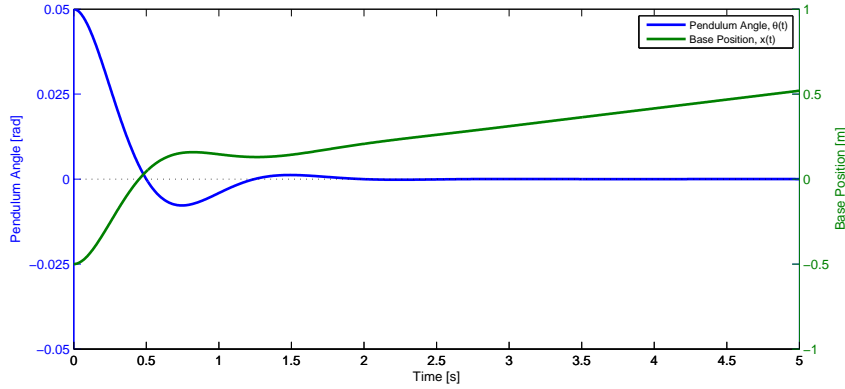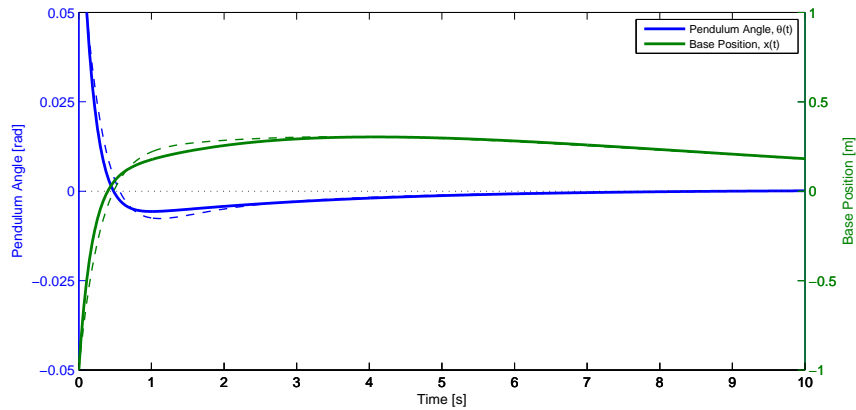

Figure 4.25: Inverted pendulum system response to impulse disturbance for $K(s) = k(s+1)/((s+0.1)(s-3))$. The closed-loop system with this controller is internally stable (both θ and x converge to zero). Dashed lines indicate system response with 20% error in the pendulum length parameter.

The time response of the closed-loop system with this internally stabilizing controller is provided in Fig. 4.25. We see that both $\theta(t)$ and $x(t)$ are now stabilized simultaneously. Note that with this controller, the pendulum stabilization is fast compared to the base position regulation.

The dashed curves in Fig. 4.25 represent the response of the system with the same controller but a 20% uncertainty in the modeled pendulum length, i.e. $L_{model} = 1$ [m], $L_{actual} = 1.2$ [m]. The two response curves are very similar, indicating that this controller is relatively robust to this type of parametric uncertainty.

The structure of the internally stabilizing controller in this case has an intuitive explanation. Consider the feed-back structure in Fig. 4.26, in which an additional feed-back control loop, K_x, is added to stabilize the pendulum base position. This loop acts always to lean the pendulum back towards the center of the track (hence the negative feed-back). In this way, both θ and x may be stabilized simultaneously.
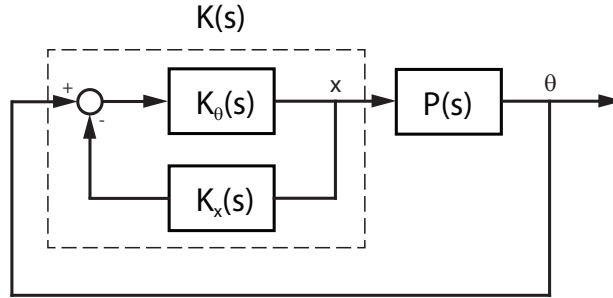
Figure 4.26: Controller structure with additional position feed-back loop.

Taking $K_\theta(s) = 100/(s - 3.9)$ and $K_x(s) = 0.036/(s + 1)$, the combined controller, $K(s) = K_\theta/(1 + K_\theta K_x) = 100(s + 1)/((s + 0.1)(s - 3))$ is identical to the internally stabilizing controller in (4.59). Thus an unstable controller in the forward path and a stable controller with a much lower gain and bandwidth in the feed-back path (responsible for the slow x response) are required to simultaneously stabilize the system.

4.9.4 Inverted Pendulum: LQG Controller/Observer Design

In order to parametrize all internally stabilizing controllers, it is first necessary to determine controller and observer gain matrices such that $A + BF$ and $A + HC$ are stable. To accomplish this,

we will use results from linear-quadratic Gaussian (LQG) optimal control theory. We may then initiate the Robust Bode design process with a LQG compensator that both stabilizes the nominal system and possesses good nominal performance characteristics. If needed, this LQG controller can be made more robust using manual loop-shaping techniques on the Robust Bode diagrams as we will show.

Linear-Quadratic Regulator (LQR)

We begin by considering the infinite horizon continuous-time linear-quadratic regulator (LQR) problem: For a linear system governed by $\dot{x} = Ax + Bu$, determine the full state feed-back control law $u = -K_c x$, which stabilizes the closed-loop, $A - BK_c$ and minimizes the quadratic cost function, (4.60).

$$J = \int_0^\infty \left(x^\top QX + u^\top Ru + 2x^\top Nu \right) dt \tag{4.60}$$

where Q, R, and N are matrices used to weight the relative importance of the error and control signals. The solution to the LQR problem is a fundamental result of optimal control theory. We will only state the results here, but the derivation may be found in any standard state-space control reference, for instance [34, 37].

The optimal control gain is given by (4.62) where $P_c > 0$ is the unique positive-definite solution of the continuous-time algebraic Riccati equation, (4.61). The LQR solution may be computed in MATLAB using the command `[Kc,Pc,e] = lqr(A,B,Q,R,N)`, where `e` is a vector of the closed-loop eigenvalues of $A - BK_c$.

$$A^\top P_c + P_c A - (P_c B + N)R^{-1}(B^\top P_c + N^\top) + Q = 0 \tag{4.61}$$

$$K_c = R^{-1}(B^\top P_c + N^\top) \tag{4.62}$$

The weighting matrices Q, R, and N should be chosen to represent the performance requirements of the system; however, as with the weighting functions in robust control, there is a general lack of formal guidelines for this selection, and an iterative guess-and-check procedure is typically employed. For our purposes, the selection is not so critical, since the controller can be improved upon in the subsequent Robust Bode loop-shaping steps.

Inverted Pendulum LQR

For regulator systems, we are interested in keeping the norm of the system output, given in (4.63), small. We choose to select the weighting matrices accordingly, $Q = C^\top C = [1, 0; 0, 0]$, $R = D^\top D = 0.01$, and $N = C^\top D = [\text{-0.1}, 0]^\top$. However, noting that the control weight, R, is two orders of magnitude smaller than the state weight, Q, we instead select $R = 1$ to limit excessive base motion (control effort).

$$\|y\| = (x^\top C^\top + u^\top D^\top)(Cx + Du) = x^\top C^\top C x + u^\top D^\top D u + 2x^\top C^\top D u \qquad (4.63)$$

Computing the LQR solution in MATLAB with these weight matrices, the state feed-back gain matrix is determined to be $K_c = [\text{-20.05}, \text{-20.05}]^\top$, which yields stable closed-loop system poles, eigenvalues of $(A - BK_c)$ at [-1, -1.005].

Kalman Filter

Kalman filters[4], provide an optimal state estimate for linear systems with additive white process and measurement noise, (4.64). In particular, the Kalman filter observer gain matrix, L_o, is selected to stabilize the observer dynamics, $A - L_c C$ and minimize the covariance of the state estimation error, $\|x - \tilde{x}\|$.

$$\dot{x} = Ax + Bu + w = (A - BK_c)x + w \qquad (4.64)$$

$$y = Cx + Du + v = (C - DK_c)x + v \qquad (4.65)$$

The process noise, w, and measurement noise, v, are assumed to be "white", namely zero-mean normally distributed (Gaussian) stochastic signals, uncorrelated in time with known covariances, i.e. $w \sim \mathcal{N}(0, W)$ and $v \sim \mathcal{N}(0, V)$. Here, we also assume that the process and measurement noises are uncorrelated with each other, and so have zero covariance, (4.66).

$$E(w) = E(v) = 0, \quad W = E(ww^\top) \geq 0, \quad V = E(vv^\top) \geq 0, \quad N = E(wv^\top) = 0 \qquad (4.66)$$

where $E(\cdot)$ denotes the statistical expectation value.

The Kalman filter dynamics are given in (4.67), in which the state estimate, $\tilde{x}$, is driven by

---

[4]Also known as linear-quadratic estimators (LQE)

the output estimate error, $(y - \tilde{y})$, via the observer gain matrix, L_o.

$$\dot{\tilde{x}} = A\tilde{x} + Bu + L_o(y - \tilde{y}) = (A - L_oC)\tilde{x} + Bu + L_oy \qquad (4.67)$$

$$\tilde{y} = C\tilde{x} + Du \qquad (4.68)$$

It can be shown that the optimal Kalman Filter observer gain, L_o, is given by (4.70), where $P_o > 0$ is the unique positive definite solution to the algebraic Riccati equation (4.69) [10,38]. Note the similarity in the state feed-back and observer gain formulae resulting from the "dual" structure of the controller and observer optimal control problems. The Kalman Filter may be computed in MATLAB using the command [Kss,Lo,Po] = kalman(sys,W,V,N), where Kss is a state-space object representing the Kalman filter dynamics, (4.67).

$$P_oA^\top + AP_o - P_oC^\top V^{-1}CP_o + W = 0 \qquad (4.69)$$

$$L_o = P_oC^\top V^{-1} \qquad (4.70)$$

Separation Principle

If we cast the controller/observer dynamics, (4.64)/(4.67), in terms of the state, x, and state estimation error $e = x - \tilde{x}$, (4.71), then we see immediately that the closed-loop eigenvalues of the LQG compensated plant is just the union of the eigenvalues of $A - BK_c$ and $A - L_oC$.

This demonstrates the well known "separation principle" of estimation and control which states that if the controller and observer systems are both independently stable, then the closed-loop system with this controller/observer combination is also stable. It is for this reason that LQG controller design problem can be divided into linear-quadratic regulator (LQR) and Kalman filter optimization sub-problems.

$$\begin{bmatrix} \dot{x} \\ \dot{e} \end{bmatrix} = \begin{bmatrix} A - BK_c & BK_c \\ 0 & A - L_oC \end{bmatrix} \begin{bmatrix} x \\ e \end{bmatrix} + \begin{bmatrix} w \\ w - L_ov \end{bmatrix} \qquad (4.71)$$

The controller and observer dynamics are not completely decoupled due to the non-zero term (BK_c) in the combined system matrix. They are typically made functionally independent, however, by ensuring that the observer poles are at least 10 times faster than the desired closed-loop system poles.

Inverted Pendulum Kalman Filter

We have not yet considered any explicit noise models in our inverted pendulum system. The process noise should represent the effects of both external disturbances and any parametric uncertainty in the model, and the measurement noise should represent any high frequency electronic noise or unmodeled dynamics. As previously noted, since we will modify the LQG compensator in subsequent Robust Bode loop-shaping steps, we must only roughly characterize the noises in this phase. We choose to weight each noise source equally, $W = [1, 0; 0 1]$ and $V = 1$. The optimal Kalman observer gain was computed in MATLAB with these covariance matrices and found to be $L_o = [2.41, 2.41]^{\top}$, which yields stable observer poles, eigenvalues of $(A - L_oC)$ at [-1.41, -1].

These observe poles do not appear to be fast enough relative to the closed-loop poles. This is indeed a limitation owing to the non-minimum phase zeros of the plant which may affect system robustness. We will attempt to mitigate these issues in the Robust Bode design process to follow.

Inverted Pendulum LQG Controller

We may now combine the LQR optimal state feed-back and the Kalman filter observer into an overall LQG compensator governed by the regulator state-space dynamics in (4.72), with a corresponding transfer function representation (4.74), and represented by the block diagram in Fig. 4.27. This may be accomplished using the MATLAB command `K_LQG = lqgreg(Lo,Kc)`. Note that we could also have performed the entire LQG design at once using the equivalent syntax `K_LQG = lqg(P,blkdiag(Q,R),blkdiag(W,V))`.
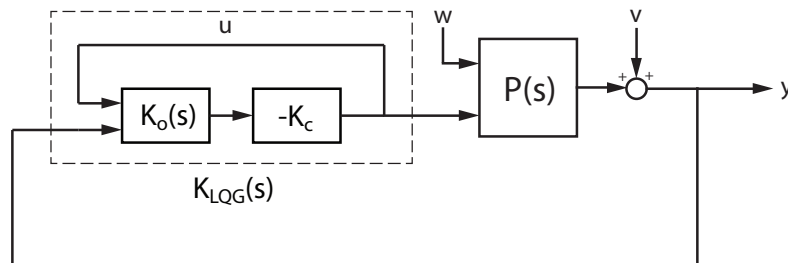
Figure 4.27: Linear-quadratic Gaussian (LQG) controller structure.

$$\dot{\tilde{x}} = (A - L_oC - (B - L_oD)K_c)\tilde{x} + L_oy \tag{4.72}$$

$$u = -K_c\tilde{x} \tag{4.73}$$

The root-locus diagram of the system with the LQG controller K_{LQG}, is shown in Fig. 4.28. Like the root-locus designed internally stabilizing compensator found previously, (4.59), the LQG compensator also has as a zero the stable plant pole $(s + 1)$, and one stable and one unstable pole. The root-loci generally have the same shape as the manually designed controller, but the optimization has moved the slower pole pair farther left (faster) and the faster pole more to the right (slower).
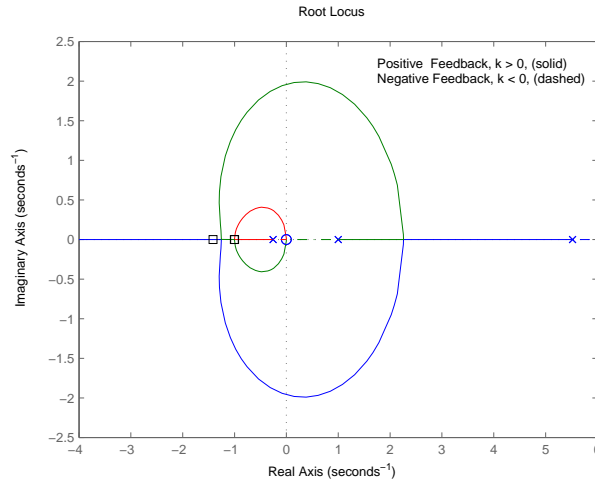
Figure 4.28: Root-locus diagram for inverted pendulum with LQG controller, $K_{LQG}(s) = k(s + 1)/(s + 0.2575)(s - 5.519)$. Again the closed-loop system poles corresponding to a controller gain $k = 96.81$ are shown as square markers.

The system response to an impulse disturbance with the LQG controller in place is provided in Fig. 4.29. The optimal LQG regulator places all closed-loop poles near $s = -1$, which results in the pendulum angle and base position converging at roughly the same rate, greatly improving the overall speed of response of the system relative to the root-locus manually designed controllers.

$$K_{LQG}(s) = \frac{U(s)}{Y(s)} = \frac{96.81(s + 1)}{(s + 0.2575)(s - 5.519)} \tag{4.74}$$

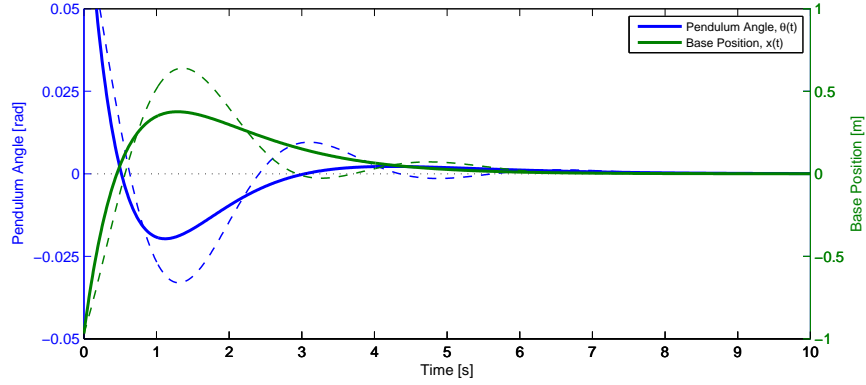Figure 4.29: Impulse response of inverted pendulum system with LQG controller, $K_{LQG}(s) = -96.81(s+1)/(s+0.2575)(s-5.519)$. Dashed lines indicate system response with 20% error in the pendulum length parameter.

If we again consider the impulse response when the model has 20% uncertainty in the pendulum length parameter (dashed lines in Fig. 4.29), we find that the errors in both θ and x have larger peak values and oscillate more than with the root-locus designed controller, cf. Fig. 4.25. This behavior is indicative of a fundamental problem with LQG methods.

It can be shown that the LQR optimal state feed-back system alone possesses excellent robustness properties, $60°$ phase margins and (-6 dB, $+\infty$) gain margins in each input channel [10]; however, when combined with a Kalman estimator in the form of an LQG controller, there are surprisingly no guaranteed robustness margins [11]. This realization was actually a primary motivation for the development of robust control theory in general.

In the following few sections, we will attempt to "robustify" the LQG compensator using loop-shaping techniques on the Robust Bode diagrams which should help minimize the peak sensitivities which give rise to large oscillatory responses in the presence of system uncertainties.

4.10 Inverted Pendulum: Robust Bode Methods

Robust Bode plots show contours of a robust metric, Γ, on the Bode magnitude and phase plots of either the controller (CRCBode) or Youla parameter (QBode). If the frequency response, $K(j\omega) or Q(j\omega)$, is designed such that it does not intersect the "forbidden regions" at any frequency, i.e. ($\Gamma_{\text{SISO}}(\omega) < 1 \ \forall \ \omega$), then a robust stability and performance criterion is satisfied.

$$\Gamma_{\text{SISO}}(\omega) = |W_1(j\omega)S_n(j\omega)| + |W_3(j\omega)T_n(j\omega)| \tag{4.75}$$

where W_1 is the performance function weighting the nominal sensitivity, S_n, and W_3 is the uncertainty function weighting the complementary sensitivity, T_n.

4.10.1 Uncertainty Weighting Function Selection

Assuming an unstructured multiplicative uncertainty representation, $P(j\omega) = P_n(j\omega)(1 + \Delta(j\omega))$, it can be shown that if the uncertainty is upper bounded by, $|\Delta(j\omega)| \leq |W_3(j\omega)|$, then the system is robustly stable if the inequality (4.76) is satisfied.

$$|W_3(j\omega)T_n(j\omega)| < 1 \tag{4.76}$$

Consequently, in order to identify the uncertainty weighting function we typically begin by investigating the effect of any known uncertainties on the plant frequency response. In this case, we are only concerned with uncertainty in the pendulum length parameter of $\pm 20\%$.

Fig. 4.30 shows upper and lower bounds on the plant frequency response computed from the plant state-space realization (4.55) with the length perturbed over the range, $L = L_0(1 \pm 0.2)$.
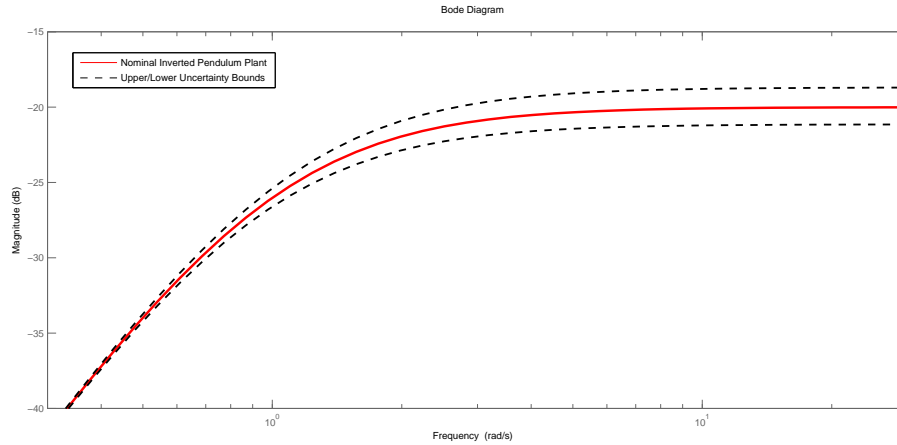
Figure 4.30: Uncertainty bounds on inverted pendulum frequency response due to parametric uncertainty in pendulum length, $L = L_0(1 \pm 0.2)$.

The frequency-dependent function corresponding to the relative error between the nominal plant model and the upper uncertainty bound is computed and shown in Fig. 4.31, (dashed green line). There are, however, additional constraints that must be included in the final uncertainty weight (solid green line). Since the complementary sensitivity function gives the mapping from noise input to system output, it is important to keep it small at frequencies where the noise is

significant. Generally, a high-frequency roll-off rate is required, which we include by selecting an improper uncertainty weight which increases at the desired rate, in this case 20 dB/decade.
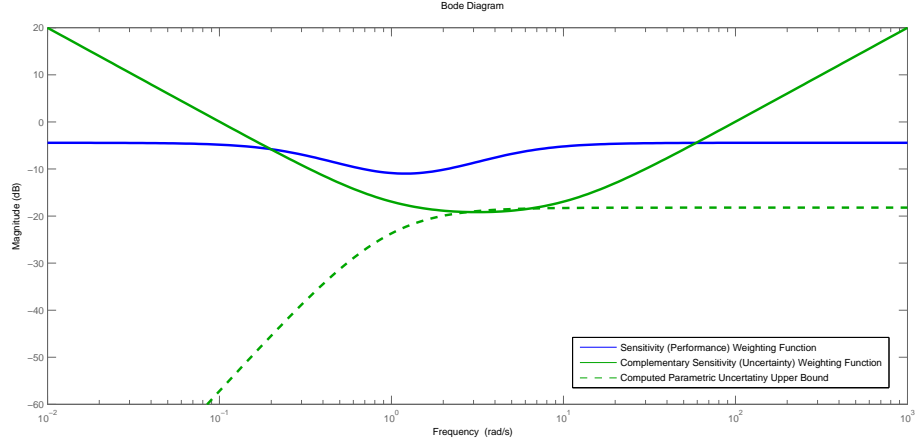
Figure 4.31: Performance and uncertainty weighting functions used in inverted pendulum Robust Bode design. The dashed line is the computed upper bound on the unstructured multiplicative error due to parametric length uncertainty.

$$W_1(s) = \frac{0.6(s+1.2)^2}{(s-4.8)(s+0.3)} \tag{4.77}$$

$$W_3(s) = \frac{0.01(s+1)(s+10)}{s} \tag{4.78}$$

Interpolation Constraints

Since there can be no unstable pole/zero cancellations between the plant and controller to achieve internal stability, all unstable poles and zeros of the plant must appear in the loop transfer function, $L(s) = K(s)P(s)$. Therefore, non-minimum phase systems are subject to the following "interpolation constraints" at any right half-plane zeros, z, (4.79).

$$P(z) = 0 \quad \Rightarrow \quad S(z) = (1+K(z)P(z))^{-1} = 1 \quad \Rightarrow \quad T(z) = 1 - S(z) = 0 \tag{4.79}$$

Likewise for unstable systems, the interpolation constraints at the location of the right half-plane poles, p, are (4.80).

$$P(p) = \infty \quad \Rightarrow \quad S(p) = (1+K(p)P(p))^{-1} = 0 \quad \Rightarrow \quad T(p) = 1 - S(p) = 1 \tag{4.80}$$

Therefore, in order to comply with internal stability requirements, we must select weights which are infinite whenever the corresponding sensitivity function is constrained to zero at any zeros/poles on the imaginary axis.

The inverted pendulum system has two zeros on the imaginary axis at $s = 0$, therefore, $T(0) = 0$, and we must ensure the complementary sensitivity weighting function, $W_3(0) = \infty$ is infinite here, which we accomplish by including an integrator. The final form of W_3 must over-bound the parametric uncertainty, increase at 20 dB/dec at high frequencies, and have a pole at zero. This corresponds to the PID form shown in (4.78).

4.10.2 Performance Weighting Function Selection

The performance weighting function is selected to satisfy the inequality, (4.81). Therefore, the performance weight should be high at any frequencies where tight disturbance rejection/reference tracking is required.

$$|W_1(j\omega)| < \frac{1}{S(j\omega)} \tag{4.81}$$

The inverted pendulum is a regulation (not servo) control system. It's primary purpose is to maintain stability and prevent excessive oscillations in the presence of impulse disturbances. An ideal impulse has an infinite bandwidth in the frequency domain. Finite width pulse disturbances, have large but not infinite frequency extent. It is therefore reasonable to begin with a constant sensitivity weighting function.

Analytic Constraints - Weighted Sensitivity Peaks

It can be shown using the maximum modulus theorem that for closed-loop internal stability, the weighted sensitivity function must satisfy for each RHP zero, z, (4.82) [18].

$$\|W_1 S\|_\infty \geq |W_1(z)| \prod_{i=1}^{N_p} \frac{|z + \bar{p}_i|}{|z + p_i|} \tag{4.82}$$

where p_i denotes the N_p RHP poles of the plant. If the plant is stable the constraint reduces to (4.83)

$$\|W_1 S\|_\infty \geq |W_1(z)| \tag{4.83}$$

This imposes an upper bound on the bandwidth of non-minimum phase plants since for robust performance, $\|W_1 S\|_\infty < 1$, it says that the sensitivity weighting function, W_1, must be less than 1 before the lowest frequency right half-plane zero. Furthermore, when there are both RHP zeros and poles, the sensitivity function peaks according to (4.82), and the weighting function must be even lower. Large sensitivity peaks correspond to highly oscillatory behavior and poor stability margins. This problem is made worse by RHP poles and zeros which are close together.

Likewise, for unstable plants the complementary sensitivity weighting function must satisfy for each RHP pole, p, (4.84).

$$\|W_3 T\|_\infty \geq |W_3(p)| \prod_{j=1}^{N_z} \frac{|\bar{z}_j + p|}{|z_j - p|} \tag{4.84}$$

where z_j are the N_j RHP zeros of the plant. If the plant is minimum phase, then $N_j = 0$, and we have

$$\|W_3 T\|_\infty \geq |W_3(p)| \tag{4.85}$$

The uncertainty weighting functions, W_3, typically increase with frequency, so (4.85) implies that in order to achieve robust stability, $\|W_3 T\|_\infty < 1$, the the complementary sensitivity should not decrease much until after the highest frequency unstable pole. Thus unstable poles present a lower limit on bandwidth to achieve for closed-loop stability.

For the inverted pendulum system, we have zeros at the origin, so we must have $W_1(0) < 1$, and since we have both CRHP zeros and poles we expect sensitivity peaking near the unstable pole frequencies, $s = 1$ [rad/s]. Therefore, we allow the sensitivity weighting function to dip here, but control the depth to prevent unwanted oscillations. The final uncertainty weighting function satisfying these requirements is given in (4.77).

4.10.3 Inverted Pendulum: CRCBode Loop-Shaping

As we have discussed thoroughly, we will initiate the CRCBode design process with the linear-quadratic Gaussian based controller designed in the previous sections. The CRCBode diagram corresponding to $K_0 = K_{LQG}$ is presented in Fig. 4.32. As we can see in Fig. 4.32, there are intersections with the forbidden regions only in the mid-frequency region near 2 [rad/s].
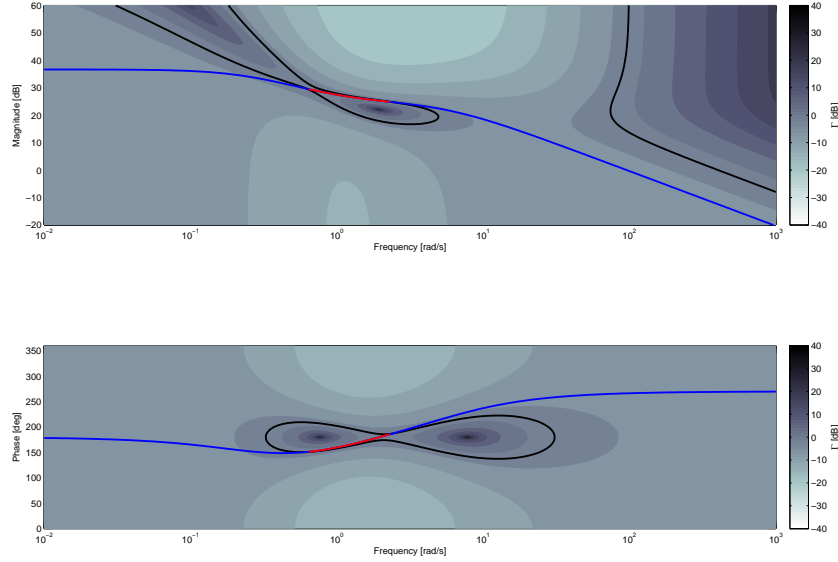
Figure 4.32: Loop-Shaping Iteration 0: CRCBode diagram corresponding to LQG based controller, K_0, (4.86).

$$K_0 = K_{LQG} = \frac{96.81(s+1)}{(s+0.2575)(s-5.519)} \qquad (4.86)$$

Previously in the robust loop-shaping process we have always cascaded low-order compensators, e.g. integrators, lead/lag, and so on, in an attempt to avoid the forbidden regions. Indeed, one of the primary advantages of using the CRCBode plots vs. automated synthesis routines or QBode approaches, is that the structure and order of the controller can directly be specified.

In this case, the LQG controller is already second-order, which may be sufficient to satisfy the robustness objectives. Robustness is almost always improved by using the lowest order compensator possible, so we continue with the loop-shaping by adjusting or tuning the parameters of the LQG controller without adding additional dynamics. As a first step, we simply round the controller parameters, resulting in the CRCBode plots shown in Fig. 4.33, and controller (4.87).

There is some improvement, indicating that these small changes are in the correct direction, but of course the intersection with the forbidden region still remains. Next we try altering the the stable pole by itself, as shown in Fig. 4.34 and (4.88).

With K_2, the robust objectives are satisfied since all forbidden regions are avoided. We may however, further optimize the controller robustness by trying to reduce the max Γ contour inter-
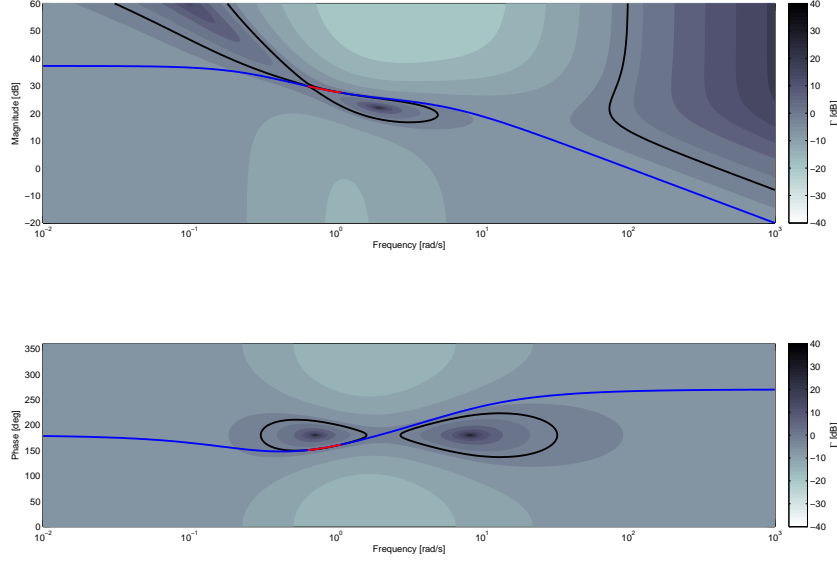
Figure 4.33: Loop-Shaping Iteration 1: CRCBode diagram corresponding to controller, K_1, (4.87).

$$K_1 = \frac{100(s+1)}{(s+0.25)(s-5.5)} \tag{4.87}$$

sected by the controller. To this end, we increase the gain slightly as shown in Fig. 4.35 and (4.89).

We select K_3 as the final controller, since all forbidden regions are avoided and Γ is minimized. To verify performance, we again compute the impulse response with this controller, given Fig. 4.36.

This impulse response is slightly slower to converge than the the original LQG design, Fig. 4.29; however, it also exhibits lower peak over-shoot and dramatically lower levels of oscillation. Thus we have demonstrated that the CRCBode robust loop-shaping procedure has successfully improved upon the linear-quadratic Gaussian design, making the system significantly more robust to higher levels of parametric uncertainty.

4.10.4   Inverted Pendulum: QBode Loop-Shaping

Since the LQG controller by design stabilizes the nominal system, we may initially interpret the forbidden regions on the CRCBode diagrams unambiguously. If we always act to decrease the robust metric and move away from the forbidden regions, then we are in fact maintaining
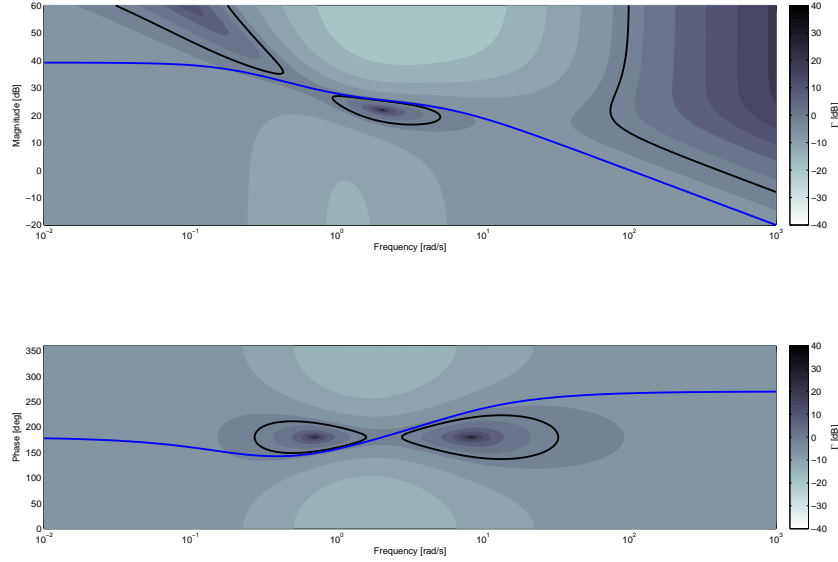
106

Figure 4.34: Loop-Shaping Iteration 2: CRCBode diagram corresponding to controller, K_2, (4.88).

$$K_2 = \frac{100(s+1)}{(s+0.2)(s-5.5)} \tag{4.88}$$

closed-loop stability and increasing the robustness margins.

However, it must be noted that for difficult systems such as this, even seemingly minor changes to the compensator may inadvertently destabilize the system by causing the frequency-response to "jump" over a small forbidden region, such as that seen in the center of the magnitude plot in Fig. 4.32, in a single step. For this reason, care must be taken to only make incremental changes and check internal stability with each compensator iteration. If a certain system continues to cause trouble, it is worthwhile pursuing the Youla based design presented in this section, since internal stability is guaranteed for stable $Q(s)$ at the expense of possibly high-order controllers.

The nominal LQG controller corresponds to setting $Q(s) = 0$ in the Youla parametrization, (4.11). We begin by investigating the QBode diagram corresponding to this choice, shown in Fig. 4.37 and (4.90). Due to the decibel scale, the $Q = 0$ magnitude response is not visible in Fig. 4.37. Nevertheless, we can see from the general shape of the magnitude forbidden region that a stable first-order $Q(s)$ may be a good choice for the next iteration, shown in Fig. 4.38 and (4.91).

The gain of Q_1 was adjusted to place the frequency response in the center of the allowable region
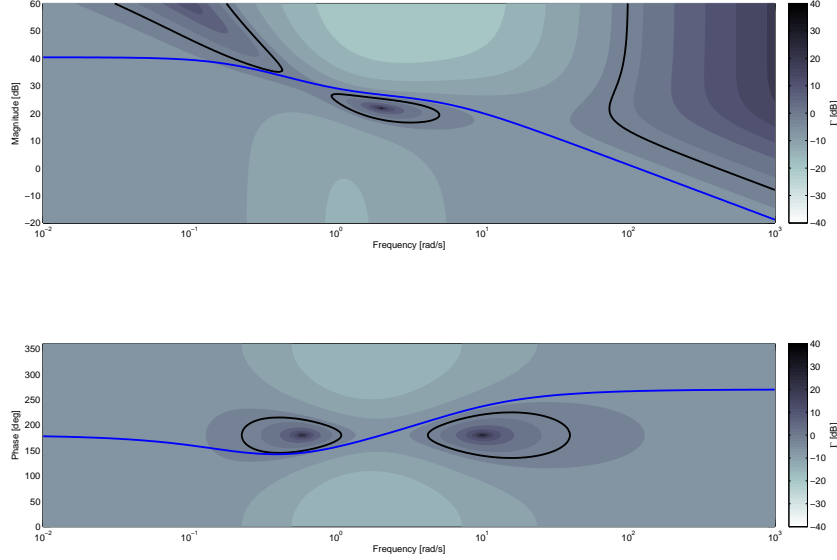
107

Figure 4.35: Loop-Shaping Iteration 3: CRCBode diagram corresponding to controller, K_3, (4.89).

$$K_3 = \frac{115(s+1)}{(s+0.2)(s-5.5)} \tag{4.89}$$

in Fig. 4.38. Even though $Q_1(s)$ is a simple first-order stable transfer function that was determined in a single design iteration, we see that all forbidden regions are avoided. This demonstrates that loop-shaping in terms of the Youla parameter $Q(s)$ is generally much simpler than the equivalent direct compensator design on the CRCBode plots.

The controller corresponding to Q_1 is provided in (4.92). We see that the Youla parametrization indeed generates higher-order controllers than necessary, but we obtain them with less design effort.

$$Q_1(s) = \frac{15}{s+0.2} \qquad \Leftrightarrow \qquad K_{Q_1}(s) = \frac{81.3265(s+1)(s^2+1.339s+0.4965)}{(s-4.025)(s+0.1373)(s^2+1.359s+0.5068)} \tag{4.92}$$

The CRCBode diagram for the Youla based controller, (4.92), is shown in Fig. 4.39. As it must, the controller frequency response does not intersect any forbidden regions, and also it may reach slightly lower Γ levels than the directly designed controller, (4.89).

To verify the robust performance of the Youla based controller, we compute the impulse response, shown in Fig. 4.40. The base position mode is slower than the manual designed controller, and the peak and oscillatory behavior between the two seems comparable. Therefore we conclude
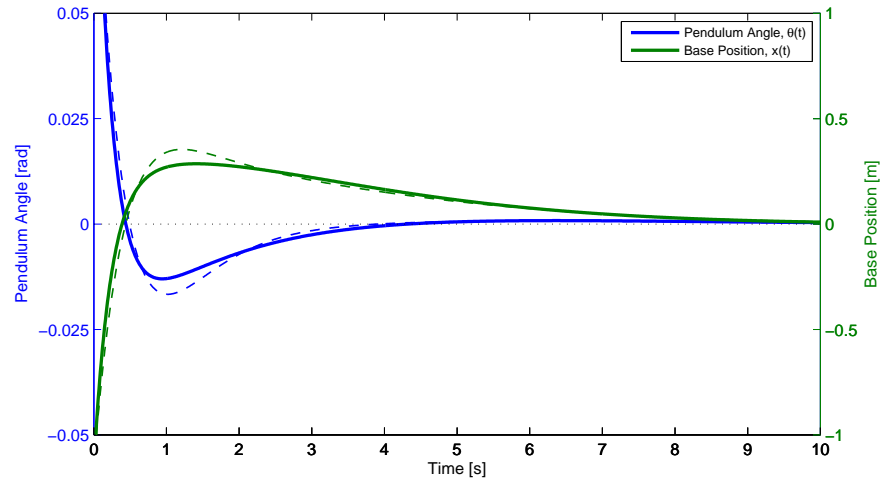
Figure 4.36: Response of inverted pendulum system to impulse disturbance with, K_3, (4.89). Dashed lines indicate system response with 20% error in the pendulum length parameter.
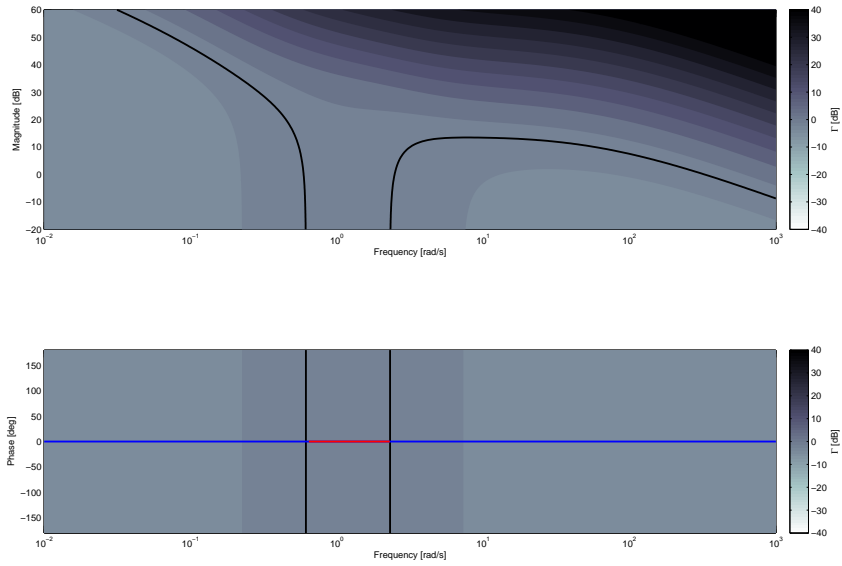
Figure 4.37: Loop-Shaping Iteration 0: QBode diagram corresponding to controller, $Q_0(s) = 0$, (4.90).

$$Q_0(s) = 0 \quad \Rightarrow K_0(s) = K_{LQG} = \frac{X(s)}{Y(s)} \tag{4.90}$$

that directly designed controller K_3, (4.89), is the best choice for a robust stabilizing controller for the inverted pendulum system.
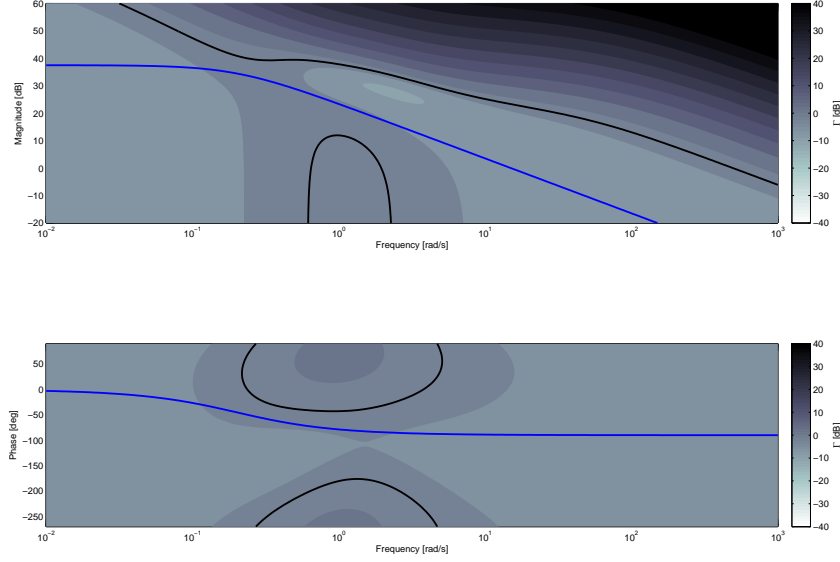
Figure 4.38: Loop-Shaping Iteration 1: QBode diagram corresponding to controller, $Q_1(s)$, (4.91).

$$Q_1(s) = \frac{15}{s + 0.02} \tag{4.91}$$

4.11 Conclusion

In this paper, the Contoured Robust Controller Bode (CRCBode) plot was applied to the loop-shaping controller design of a simple non-minimum phase SISO system (RHP zero). The robust performance and stability metric, Γ, was shown to be ambiguous in terms of closed-loop stability since it measures only the "distance" to the critical -1 point without regard to encirclements.

An alternative approach was introduced to avoid this limitation in which the Youla parameterization, $Q(j\omega)$, was shaped directly on the so-called QBode plots. The non-minimum phase algebraic and analytic design constraints were reviewed, and it was shown that if the weighting functions are appropriately selected, then the design constraints naturally appear in the forbidden regions without the need for direct evaluation.

It was demonstrated that nearly identical results may be obtained using either C or Q loop-shaping for the simple non-minimum phase system considered here. In general Q shaping is easier since stability does not have to be explicitly considered during the design process. Unfortunately
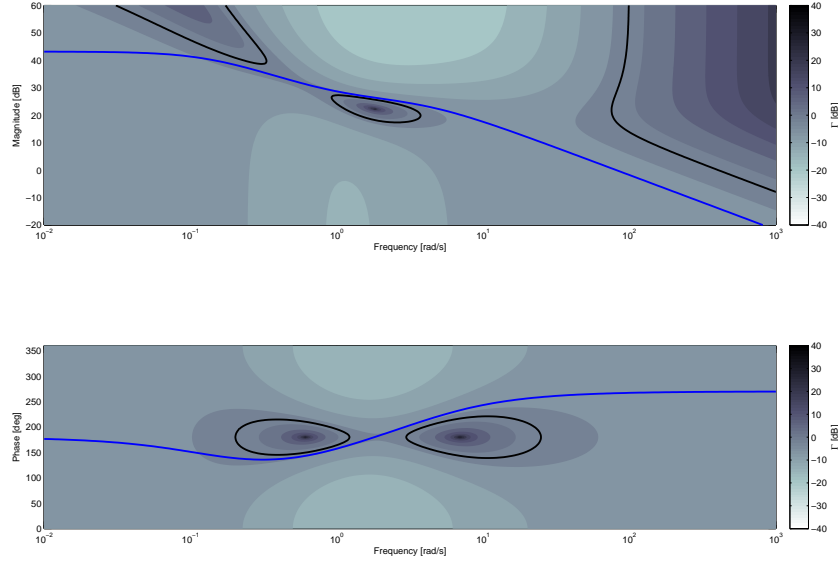
Figure 4.39: CRCBode diagram corresponding to Youla based controller, $Q_1(s) \Leftrightarrow K_{Q_1}(s)$, (4.92).

this design simplicity typically comes at the expense of controller complexity.

A reasonable design approach that we advocate for more complicated systems, including open-loop unstable plants, is to perform a preliminary control design iteration on the QBode plot. This generates an initial controller, C_1 which is guaranteed to be nominally stabilizing and which roughly satisfies the design constraints of the problem. Subsequent design iterations on C using the CRCBode plots can then be used to reduce the complexity of the initial controller as necessary, while also avoiding the forbidden regions thereby optimizing the robust performance and stability of the system.
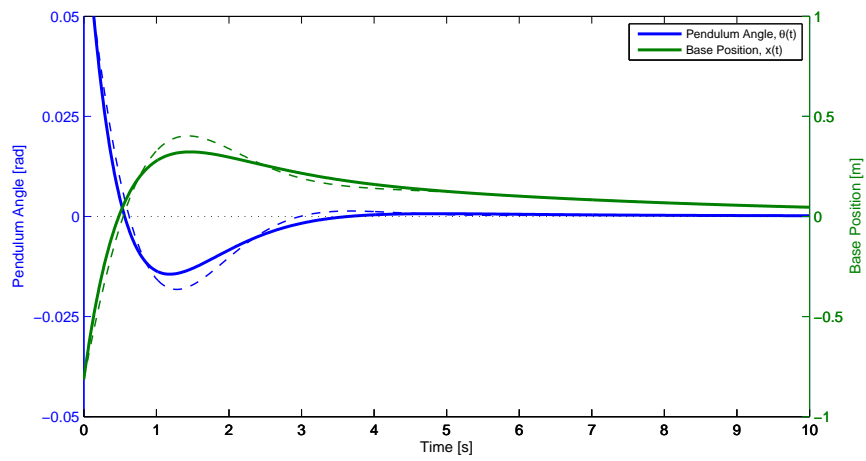
Figure 4.40: Response of inverted pendulum system to impulse disturbance with, $K_{Q_1}(s)$, (4.92). Dashed lines indicate system response with 20% error in the pendulum length parameter.

Chapter 5

Robust Bode Methods for Multi–Input/Multi–Output (MIMO) Systems

5.1   Introduction

Classical frequency–domain control design techniques often exhibit good robustness properties but are difficult to generalize to multi–input/multi–output MIMO systems. Optimal state–space approaches, e.g. the Linear–Quadratic–Gaussian (LQG) problem, on the other hand, apply directly to multi–dimensional systems, but can be sensitive to model uncertainty [2]. Modern H_∞ robust control theory addresses this issue, but like other numerical synthesis algorithms obscures the design process and often generates higher–order controllers than necessary.

The fundamental metric in robust control is the H_∞– norm which corresponds to the maximum 2–norm "system gain" from input to output [3]. Consequently, the basic design principles of classical frequency–domain loop–shaping control can be generalized naturally to a MIMO robust control framework. For example, increasing the system gain (minimum singular value) at low frequencies relative to the 0 dB cross–over, minimizes the H_∞– norm of the sensitivity function and improves disturbance rejection and tracking performance. Similarly, reducing the system gain (maximum singular value) at high frequencies minimizes the complementary sensitivity function, limiting noise transmission and improving stability margins. Various "robust loop–shaping" procedures have been proposed which attempt to satisfy more precise design boundaries on the open-loop singular value plots. [5, 17, 29].

In this chapter, we extend the robust loop–shaping concept and develop a new graphical control design technique for nonlinear multi–input/multi–output systems based on the Contoured Robust Controller Bode (CRCBode) plot which shows contours (level–sets) of a robust metric on the controller Bode magnitude and phase plots. The goal is to shape the controller frequency response of each input/output pair so that the robust metric is minimized and all intersections with certain "forbidden regions" are avoided, indicating that a robust stability and performance objective is satisfied.

To demonstrate this approach, we consider the design of a controller for a high–speed, low–tension MIMO magnetic tape drive memory system [39]. An approximate system inverse is first computed which effectively decouples the inputs and outputs and facilitates subsequent loop–shaping design iterations required to avoid all forbidden regions on the CRCBode plots. The nonlinear dynamics of the system are included as a structured (parametric) uncertainty set consisting of linearizations about several operating points and influencing the extent of the forbidden regions. Finally, the controller designed using the CRCBode approach is compared with one generated using a standard automated H_∞ synthesis algorithm.

5.2 Robust Stability and the Small–Gain Theorem
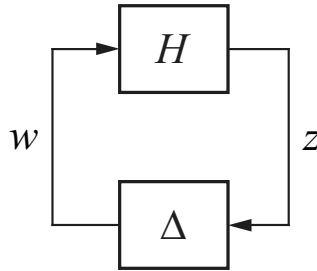
Figure 5.1: Basic perturbation model.

The small-gain theorem, introduced in Chapter 3, states that if H and Δ in are both stable, then Eq. (5.1) provides a sufficient condition for the *robust stability* of the general feed-back configuration shown in Fig. 5.1.

$$\|H\|_\infty \cdot \|\Delta\|_\infty < 1 \iff \overline{\sigma}(H(j\omega)) \cdot \overline{\sigma}(\Delta(j\omega)) < 1 \ \forall \ \omega \in \mathbb{R} \tag{5.1}$$

where $\|\cdot\|_\infty$ is the H_∞ norm defined as the maximum singular value, $\overline{\sigma}(\cdot)$, over all frequencies.
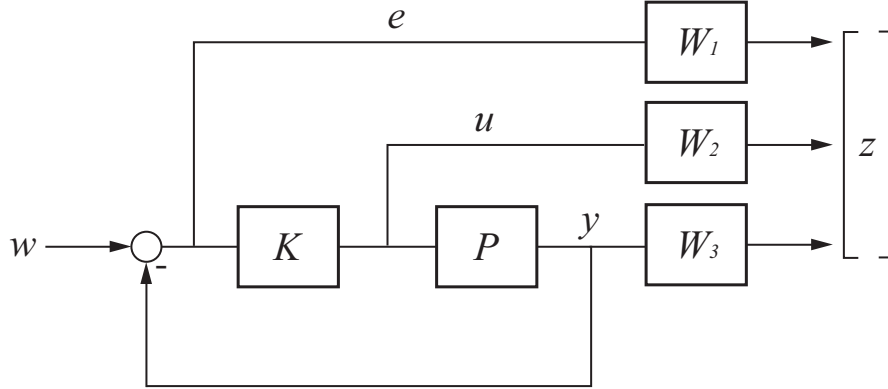
Figure 5.2: Feedback diagram for standard mixed sensitivity problem.

If all perturbations $\|\Delta\|_\infty < 1$ are allowed, that is if the uncertainty is *completely unstructured*, then the small–gain theorem is both a sufficient and necessary condition for robust stability; however, if there is any structure to the perturbation, for instance due to uncertainty in the physical parameters of the system, then the small–gain theorem can be excessively conservative. For this reason, the "structured singular value" and related "μ–synthesis" techniques were developed based on the generalized Nyquist stability theorem which are less conservative but also less mathematically tractable [30, 40]. The CRCBode approach, however, provides a new method of controller design based on the simpler H_∞ norm which also accounts for finite *structured* uncertainty sets without adding any significant complexity to the design process.

5.3   General Mixed Sensitivity Problem

The mixed sensitivity problem, Fig. 5.2, is a standard robust control problem concerned with finding a stabilizing controller, K, which minimizes the H_∞– norm, γ, of a combined sensitivity transfer function matrix, H, from disturbance inputs, w, to regulated outputs, z, Eq. (5.2) [31].

$$\|H\|_\infty = \left\| \begin{matrix} W_1 S \\ W_2 KS \\ W_3 T \end{matrix} \right\|_\infty = \gamma \tag{5.2}$$

where $S = (I + PK)^{-1}$ and $T = I - S$ are the (nominal) sensitivity and complementary sensitivity transfer function matrices respectively. W_1, W_2, and W_3 are frequency–dependent weighting functions chosen to express closed-loop robust performance and disturbance rejection through W_1S, control power limitations through W_2KS, and stability and noise rejection through W_3T. For example, if the error signal should have magnitude $|e| < \epsilon$ for a unit disturbance at frequency ω, then the weighting function should be selected as $|W_1(j\omega)| > 1/\epsilon$.

5.4 CRCBode Plots and the Robust Metric

In this chapter, we choose to construct CRCBode plots corresponding to the general mixed sensitivity problem; however, in general, any weighted transfer function matrix could be used. Referring to Eq. (5.2), we define the MIMO robust performance metric as:

$$\Gamma_{\text{MIMO}}(\omega) \triangleq \overline{\sigma}\left(\begin{bmatrix} W_1S \\ W_2KS \\ W_3T \end{bmatrix} \right) \tag{5.3}$$

From the small–gain theorem, Eq. (5.1), a sufficient condition for the robust stability and performance of the feed-back system is then: $\Gamma_{\text{MIMO}}(\omega) < 1$ (0 dB) for all ω. The general objective then of robust loop–shaping control is to select all elements of the controller transfer function matrix, $K_{ij}(s)$, such that this condition is satisfied at all frequencies. Unfortunately, due to the multi-dimensionality of the system and competing performance objectives, this process has traditionally proven very difficult to accomplish using classical techniques, since design decisions made in any one element of the controller can have unintended and undesirable effects on other loops.

CRCBode plots, an example of which is shown in Fig. 5.3, facilitate the loop–shaping controller design process by explicitly evaluating and visualizing the robust metric, $\Gamma(\omega)$, over a range of controller magnitudes and phases.[1] For any structured uncertainty, the maximum Γ over this set used. Any intersections of the proposed controller frequency response (orange) with the regions in which $\Gamma(\omega) \geq 1$, i.e. the "forbidden regions" (black border), indicate that the robust stability and performance criteria are violated.

---

[1]Specifically, for the magnitude CRCBode plots, fix the controller phase and evaluate $\Gamma(\omega)$ over a range of magnitudes. Vice versa for the phase plots.

The controller frequency response is shaped by combining basic dynamic compensators (e.g. integrators or lead compensators) to avoid all forbidden regions on the CRCBode plots thus generating a robust controller. The design process typically proceeds iteratively since each change to the proposed controller alters the shape and extent of the forbidden regions. Furthermore, any uncertainty or performance objectives which are unattainable will be manifest in forbidden regions which do not reduce in size and cannot be avoided. In these cases, either the weighting functions should be modified or pre-compensation should be added prior to the CRCBode loop–shaping process.

For MIMO systems, it is extremely advantageous for the open-loop system to have a high degree of diagonal dominance, since in this case each input affects only a single output with little cross–coupling, and controller design can be carried out in a more–or–less independent SISO fashion. An approximate inverse pre-compensation matrix, D, is typically required to accomplish this diagonalization, after which a diagonal dynamic compensator, C, may be sought using the CRCBode approach. In this case, the overall controller is the product, $K = DC$, but the only "free design variables" are the diagonal elements of C. For this reason, CRCBode plots for MIMO systems, cf. Fig. 5.3, are constructed only for the diagonal elements, C_{ii}, by evaluating $\Gamma(\omega)$ over a range of controller magnitudes $|C_{ii}(j\omega)|$ and phases $\angle C_{ii}(j\omega)$ keeping all other controller elements fixed. It is important to observe that since Γ is a matrix (system) norm and a function of the overall controller, K, that any adverse effects due to cross–coupling are immediately apparent from intersections with the forbidden regions which are themselves consistent across all CRCBode plot elements.

Finally, note that $\Gamma(\omega)$ is written instead of $\Gamma(j\omega)$ to emphasize that unlike standard automated robust synthesis algorithms, the weighting and sensitivity functions do not necessarily have to be realizable transfer functions but may also be defined only at a finite set of frequencies, e.g. experimental frequency response data, since in the CRCBode approach, $\Gamma(\omega)$ is explicitly evaluated at those frequencies. Also decibel units are typically adopted, $\Gamma \,[\text{dB}] = 20\log(\Gamma)$, since the scale of robust performance level variations is similar to that of $|S|$ and $|T|$ over the frequency range.
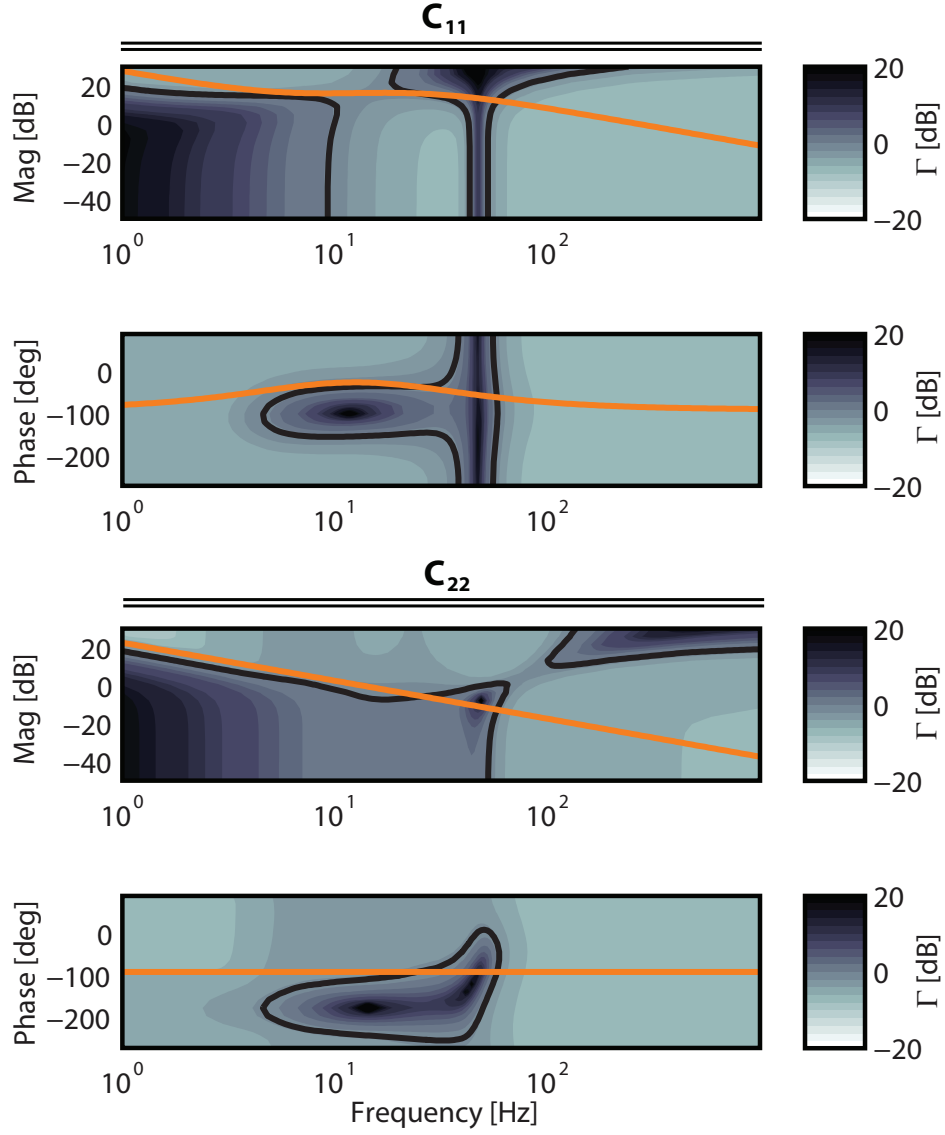
Figure 5.3: MIMO CRCBode plot showing fourth loop-shaping design iteration for the tape-drive case study: $K = C_4 D$. Intersections of the controller frequency responses (orange) with the forbidden regions, $\Gamma \geq 0$ dB (black border) indicate that a MIMO robust stability and performance criteria is violated.

5.5 Approximate Inverse and Decoupling

One way to achieve diagonal dominance is to choose the best input/output variable pairings (the so called loop assignment problem). From a mathematical perspective, this is equivalent to including a constant matrix of row and column permutations. More generally, we desire a realizable (real or rational) inverse pre-compensator matrix to accomplish this diagonalization

If the system is governed by, $y = G(s)u$, where $G(s)$ is a square transfer function matrix which is not diagonal, then a decoupling controller, D, should be chosen such that the product $G \cdot D$ is approximately diagonal. Obviously the choice $D = G^{-1}(s)$ would work; however, for most physical systems, the transfer functions elements are strictly proper (order of denominator greater than order of numerator), and thus the system inverse is in general improper and not realizable (improper filters are non-causal). The problem then is to somehow approximate the system inverse by a realizable transfer function matrix.

Kouvaritakis provides one solution to this problem using a least-squares approach known as the ALIGN algorithm [41], which is so named because it attempts to align the column vectors of the real valued approximate inverse, $\mathbf{d_i}$, with the row vectors of the system transfer function matrix evaluated at a selected frequency, $G = G(j\omega)$.

For a right system inverse, the product $G(j\omega)\mathbf{d_i}$ should approximate the i$^{\text{th}}$ standard basis vector, $\mathbf{e_i}$, within some phase factor, i.e. $G(j\omega)\mathbf{d_i} = \exp(j\delta_i)\mathbf{e_i} + \epsilon_\mathbf{i}$. This cannot be achieved exactly if $G(j\omega)$ is complex valued; however, by minimizing the squared error term $\|\epsilon_\mathbf{i}\|$ over $\mathbf{d_i}$ and the angle δ_i, it can be shown that the optimal real valued approximate inverse is given by Eq. (5.8) [41].

We wish to minimize the squared error term, ϕ_i. For notational simplicity we omit $(j\omega)$

$$\phi_i = \|\epsilon_\mathbf{i}\| = \epsilon_\mathbf{i}'\epsilon_\mathbf{i} \tag{5.4}$$

Substituting

$$\phi_i = \mathbf{d_i}^T G' G \mathbf{d_i} - \exp(-j\delta_i)\mathbf{g_i}^T \mathbf{d_i} - \exp(j\delta_i)\mathbf{d_i}^T \mathbf{g_i}^* + 1 \tag{5.5}$$

where $\mathbf{g_i}$ are the column vectors of $G(j\omega)$, ^{T} is the transpose, * is the complex conjugate, and $'$ is

the complex conjugate transpose. Now evaluate the partial derivatives of ϕ_i.

$$\frac{\partial \phi_i}{\partial \mathbf{d_i}} = [G'G + (G'G)^T]\mathbf{d_i} - \exp(-j\delta_i)\mathbf{g_i} - \exp(j\delta_i)\mathbf{g_i}^* = 0 \tag{5.6}$$

$$\frac{\partial \phi_i}{\partial \delta_i} = j\exp(-j\delta_i)\mathbf{g_i}^T\mathbf{d_i} - j\exp(j\delta_i)\mathbf{d_i}^T\mathbf{g_i}^* = 0 \tag{5.7}$$

Combining and simplifying these relations, it can be shown that the optimal real valued approximate inverse is given by

$$D = [\mathbf{d_1}, \mathbf{d_2}, ..., \mathbf{d_m}] = A^{-1}\Re[G'\exp(j\psi/2)]/2 \tag{5.8}$$

where $A = \Re[G'G]$ and $\psi = \text{diag}\{\psi_i\}$, with ψ_i the phase angle of the diagonal elements of $GA^{-1}G^T$, and $\Re[\cdot]$ the real part of a complex quantity. $G(0)$ is always real, so $G' = G^T$, and by Eq. (5.8), $D = G(0)^{-1}$, so a real valued system inverse can be obtained simply by calculating the matrix inverse at DC if $G(0)$ is square and full rank. This is a fairly common approach, since it does not require the ALIGN algorithm; however, it is typically not the best choice for several reasons.

Most properly designed feedback systems have large low-frequency gain $|L(j\omega)| >> 1 : \omega < \omega_{0\ \text{dB}}$, so at these frequencies, $T \approx LL^{-1} = I$ is inherently decoupled (i.e. approximates the identity matrix). At high frequencies, $|L|$ and $|T|$ are small to attenuate noise though not necessarily diagonal. Fortunately, since reference inputs are band-limited to lower frequencies, decoupling is usually not a priority here. System stability, on the other hand, is determined near the 0 dB crossover frequency at which the gain is neither large nor small, and it is near this frequency that significant loop-shaping is typically required. It is very advantageous, if possible, to decouple the system near this frequency using the ALIGN algorithm. If diagonal dominance can be achieved using a pre-compensator, a diagonal dynamic compensator may be designed using a straight–forward iterative loop–shaping process to avoid all intersections with the forbidden regions on the diagonal elements of the CRCBode diagrams, as demonstrated in the following case study.

5.6 Case Study: MIMO Tape Drive Memory System

Magnetic tape drive memory systems are cost effective alternatives to disc based storage for applications requiring mostly sequential data access. Tape based systems achieve high volumetric memory density by decreasing substrate and magnetic coating thickness to fit more tape per reel. Due to the reduced mechanical strength of this thin film media, low-tension tape transport drives are required. A competing objective, however, is to increase read/write speed by making the linear tape velocity as high as possible.

In this case study, we consider the design of a controller for a high-speed/low-tension prototype tape transport system. A direct-drive transport (DDT) approach is analyzed here which uses two independently driven reels. Consequently, the system is a coupled multi-input/multi-output (MIMO) system with two drive motor voltage control inputs and two outputs, tape tension and tape velocity.

The dynamics of the tape transport are in general both nonlinear and time-varying. A principle nonlinearity is due to the fact that the tape supports only tensile (not compressive) loads, and because of the low-tension objective, the system necessarily operates precariously close to this boundary. There are also several disturbance sources, notably the periodic reel eccentricity and the high-frequency dynamics of air entrainment. An effective controller for this system must account for each of these effects. In this case study, we focus particular attention on designing a controller which is robust to the parametric variations of the reel radii as tape is transfered from reel to reel during normal operation.
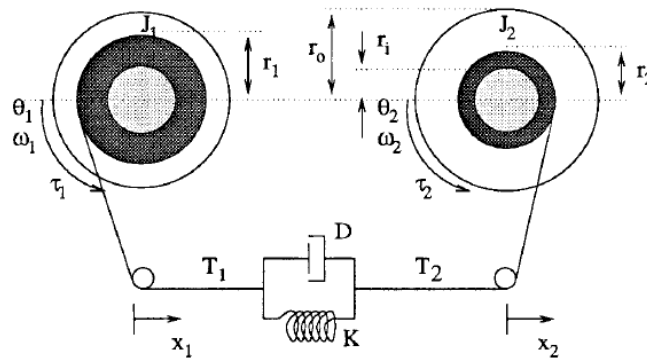

Figure 5.4: Schematic of direct-drive transport (DDT) tape drive system. The robust controller must account for the variation of the reel radii r_1 and r_2 during normal operation.

5.6.1 Tape Drive Dynamic Model

A schematic of the direct-drive tape transport system is provided in Fig. 5.4, and the nonlinear state equations for this system are given in Eq. (5.9).

$$
\begin{aligned}
\dot{T} &= K_T(\omega_2 r_2 - \omega_1 r_1) + D_T(\dot{\omega}_2 r_2 - \dot{\omega}_1 r_1 + \omega_2 \dot{r}_2 - \omega_1 \dot{r}_1) \\
\dot{r}_1 &= -\epsilon \omega_1 / 2\pi \\
\dot{r}_2 &= -\epsilon \omega_2 / 2\pi \\
\dot{\omega}_1 &= (K_{t1} u_1 - \beta_1 \omega_1 + T r_1 + 4\epsilon K_J r_1^3 \omega_1^2 / 2\pi) / J_1 \\
\dot{\omega}_2 &= (K_{t2} u_2 - \beta_2 \omega_2 + T r_2 - 4\epsilon K_J r_1^3 \omega_1^2 / 2\pi) / J_2
\end{aligned}
\tag{5.9}
$$

where T is the tape tension, r_1 and r_2 are the reel radii, and ω_1 and ω_2 the reel angular velocities. The control inputs are the two voltage inputs to the motor drivers, $[u_1 \ u_2]$. K_T and D_T are the tape stiffness and damping coefficient respectively, ϵ is the tape thickness, K_t is the motor driver gain (assumed constant in frequency range ≤ 100 Hz), β is the viscous friction coefficient of the motors, $J_1 = J_m + K_J(r_1^4 - r_i^4)$ and $J_2 = J_m + K_J(r_2^4 - r_i^4)$ are the rotational inertias of the motors plus reels, where $K_J = t_p t_w \pi / 2$ with t_p the tape density and t_w the tape width.
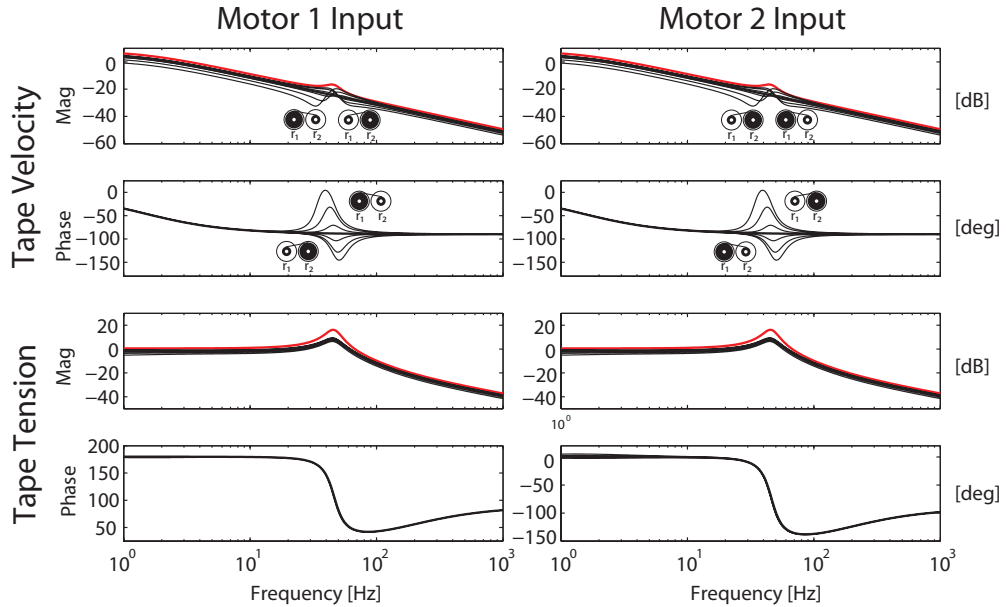

Figure 5.5: Frequency responses for sampled uncertain parameters (reel radii) of tape drive system. Nominal model, G_0 (thick solid black line), sampled systems (thin solid black lines), multiplicative uncertainty bound, $(I + W_3)G_0$.

122

We note that since ϵ is very small, the reel radii dynamics are much slower than the tension and velocity dynamics and thus may be considered static for purposes of linearization (singular perturbation analysis). These parameter variations are then accounted for in the subsequent robust controller design process. The linearized model of the reduced order system, $\dot{\mathbf{x}}(t) = \mathbf{A}\mathbf{x}(t) + \mathbf{B}\mathbf{u}(t)$, $\mathbf{y}(t) = \mathbf{C}\mathbf{x}(t)$, with state vector $\mathbf{x} = [T\ \omega_1\ \omega_2]^T$ is given by (5.10).

$$
\mathbf{A} = \begin{bmatrix} -D_T(r_2^2/J_2 + r_1^2/J_1) & -r_1 K_T + D_T\beta_1 r_1/J_1 & r_2 K_T - D\beta_2 r_2/J_2 \\ r_1/J_1 & -\beta_1/J_1 & 0 \\ -r_2/J_2 & 0 & -\beta_2/J_2 \end{bmatrix}
$$

$$
\mathbf{B} = \begin{bmatrix} -r_1 K_{t1} D_T/J_1 & r_2 K_{t2} D/J_2 \\ K_{t1}/J_1 & 0 \\ 0 & K_{t2}/J_2 \end{bmatrix} \tag{5.10}
$$

$$
\mathbf{C} = \begin{bmatrix} 0 & r_1/2 & r_2/2 \\ 1 & 0 & 0 \end{bmatrix}
$$

In order to continue with the CRCBode controller design, we need to obtain a set of frequency responses which cover the structured parametric uncertainty in the system. To this end, we determine the transfer function representations, $G(s) = C(sI - A)^{-1}B$ for several sampled parameter combinations, specifically the percentage of tape wound on each reel, $r_1(t)$ and $r_2(t)$ and evaluate the frequency responses as shown in Fig. 5.5.

The approximate real inverse of the nominal plant was evaluated at $\omega=10$ rad/s, using Eq. (5.8). Both the nominal and decoupled system frequency responses are shown in Fig. 5.6. It is clear that the approximate inverse effectively decouples this system not only at $\omega=10$ rad/s, but also over a wide range of frequencies since the off-diagonal magnitudes are greatly reduced, while having only negligible effects on the diagonal elements.
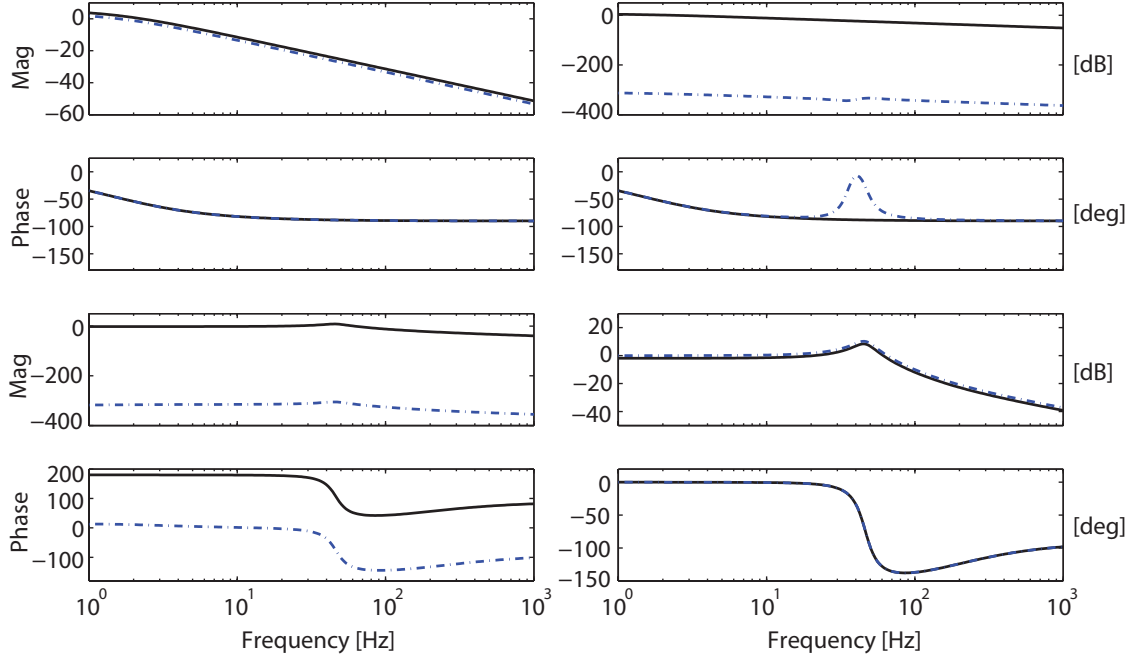
Figure 5.6: Frequency responses of nominal and decoupled open-loop system. Nominal model, G_0 (solid black line), Decoupled system, $G_0 D$ (dashed blue line).

$$\left| G(j10)D \right| = \left| \begin{bmatrix} 0.843 - j0.927 & 0.843 - j0.927 \\ -0.802 + j0.001 & -0.802 + j0.001 \end{bmatrix} \begin{bmatrix} 0.399 & -0.623 \\ 0.399 & 0.623 \end{bmatrix} \right| = \begin{bmatrix} 1.0003 & 0 \\ 0 & 1.0000 \end{bmatrix}$$

(5.11)

5.6.2 MIMO Weighting Functions

Weighting matrices are typically diagonal and represent weights on the output and input signals of the system via pre- (W) and post-multiplication (V) respectively (e.g. $\|WHV\|_\infty$). Rational performance W_1 and uncertainty W_3 weighting functions were chosen for this example given in Eqs. (5.12) and shown in Figs. 5.7. No control power weighting was included in this problem, $W_2 = 0$.
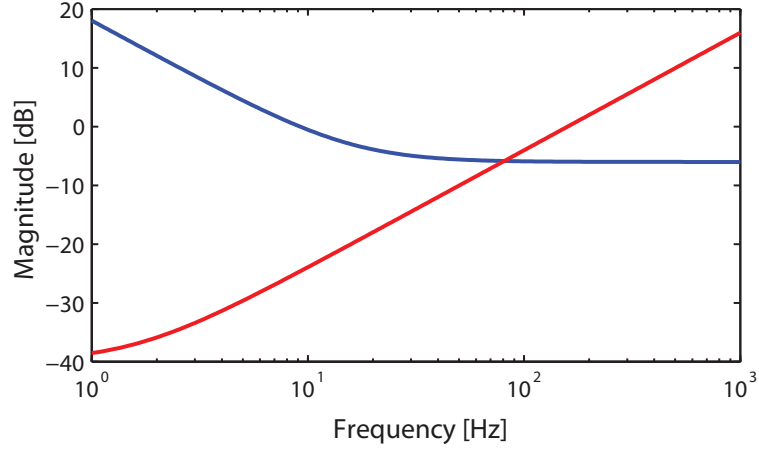
Figure 5.7: Magnitude of output multiplicative performance, W_1 (blue) and uncertainty, W_3 (red), weighting functions.

$$W_1 = 0.5\frac{(s+100)}{s}\begin{bmatrix} 1 & 0 \\ 0 & 1 \end{bmatrix} \tag{5.12}$$

$$W_3 = 0.001(s+10)\begin{bmatrix} 1 & 0 \\ 0 & 1 \end{bmatrix} \tag{5.13}$$

5.6.3 MIMO CRCBode Loop-Shaping Design Iterations

Since the approximate inverse compensator, D, effectively decouples the system over the frequency range of interest, it is possible to design independent dynamic compensators for each input/output pair using loop-shaping techniques on the CRCBode diagrams. The overall controller is then the product of the diagonal dynamic compensator, C, and the inverse compensator, D, i.e. $K = DC$.

Iteration 1

We begin by considering the CRCBode plots of the feedback system with $C_1 = I$, Fig. 5.8. There are large low frequency intersections with the forbidden regions in both the (1,1) and (2,2) elements that must be addressed.

$$C_1 = \begin{bmatrix} 1 & 0 \\ 0 & 1 \end{bmatrix} \tag{5.14}$$
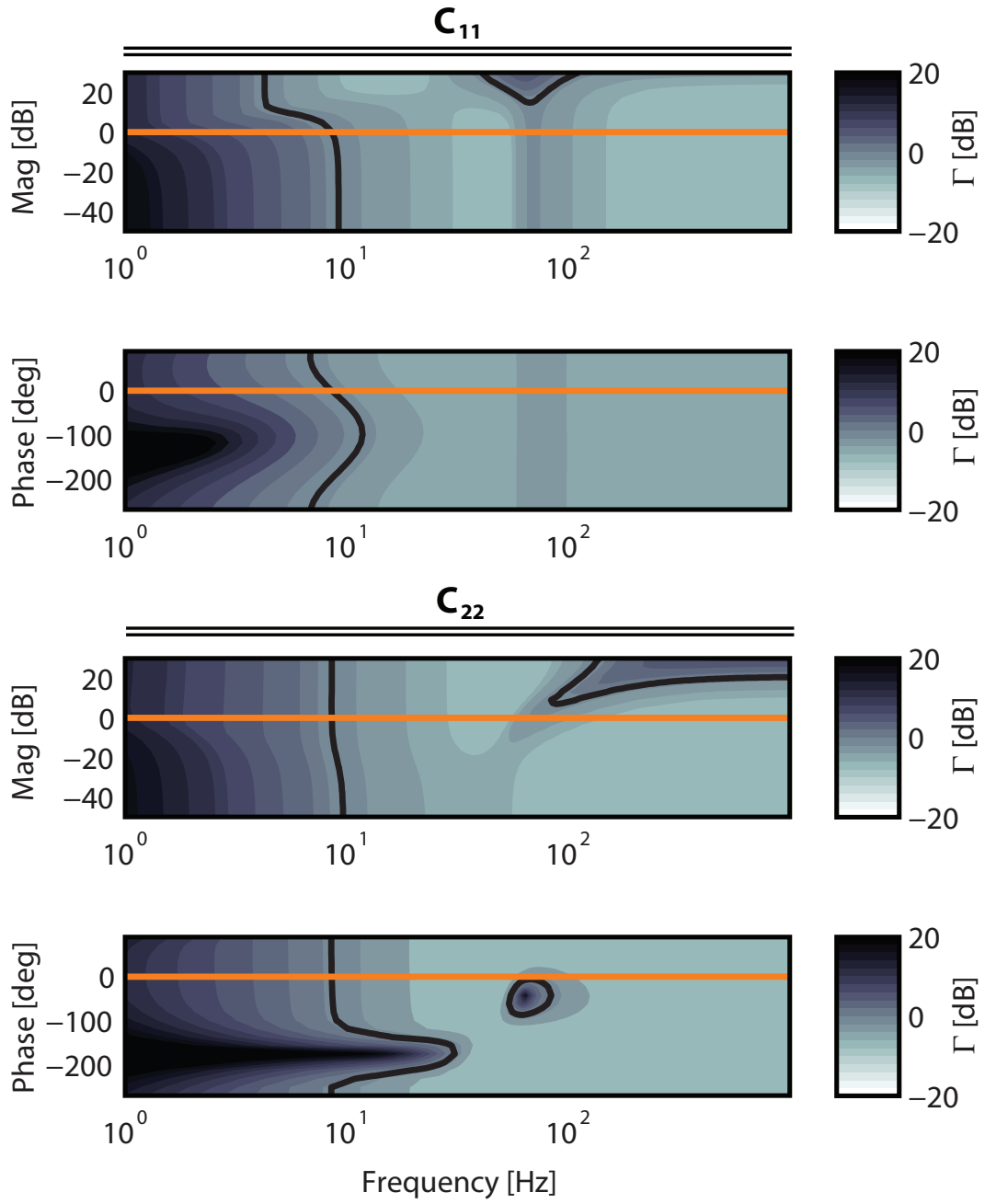
125

Figure 5.8: Controller Design Iteration 1: C_1

Iteration 2

Fig. 5.9 shows the CRCBode plots with an integrator added to the (1,1) position. There are still low frequency intersections in both positions, however, these will be eliminated in the following step.
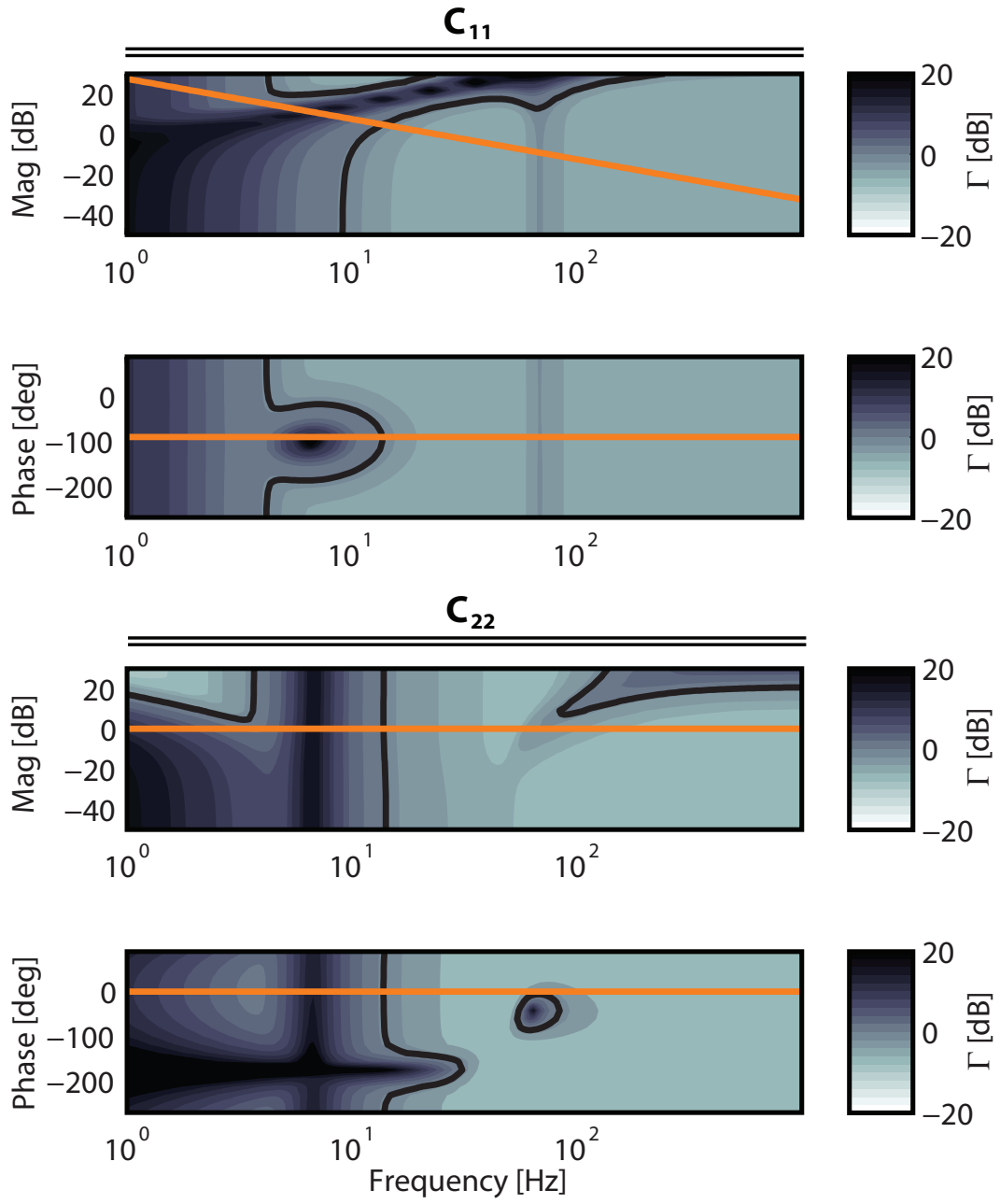
Figure 5.9: Controller Design Iteration 2: C_2

$$C_2 = \begin{bmatrix} 150/s & 0 \\ 0 & 1 \end{bmatrix} \qquad (5.15)$$

Iteration 3

Fig. 5.10 shows the CRCBode plots with another integrator added to the (2,2) position. The gains of both the (1,1) and (2,2) controllers were tuned iteratively and simultaneously in this step to avoid the lowest frequency intersections. Examination of the phase plots indicate that phase lead is necessary in both the (1,1) and (2,2) elements at two distinct frequencies near 10 Hz and 60 Hz. It is fairly evident that the larger vertical forbidden zone in (1,1) is due to the smaller zone in (2,2) and vice versa. This is a result of $\Gamma_{\text{MIMO}} = \|H\|_\infty$ being a matrix norm. It also demonstrates that all intersections are consistent in frequency over every CRCBode element.

$$C_3 = \begin{bmatrix} 150/s & 0 \\ 0 & 84/s \end{bmatrix} \tag{5.16}$$

Iteration 4

In Fig. 5.3, we attempt to eliminate the intersections near 10 Hz in both plots using a complex lead compensator. Some trial and error revealed that the best choice was a center frequency $\omega = 12.5$ Hz, max phase lead $\phi = 65°$, and damping ratio $\zeta = 1$.

$$C_4 = \begin{bmatrix} 150/s \cdot \text{clead}(65, 25\pi, 1) & 0 \\ 0 & 84/s \end{bmatrix} \tag{5.17}$$

Iteration 5

Finally in Fig. 5.11 we add another complex phase lead compensator to the (2,2) element with parameters $\omega = 65$ Hz, $\phi = 90°$, and $\zeta = 1$. In this case, all intersections were eliminated; however, from our discussion of the conservativeness of the MIMO norm, we must now verify the results using various other means including simulations.

$$C_5 = \begin{bmatrix} 150/s \cdot \text{clead}(65, 25\pi, 1) & 0 \\ 0 & 84/s \cdot \text{clead}(90, 122\pi, 1) \end{bmatrix} \tag{5.18}$$
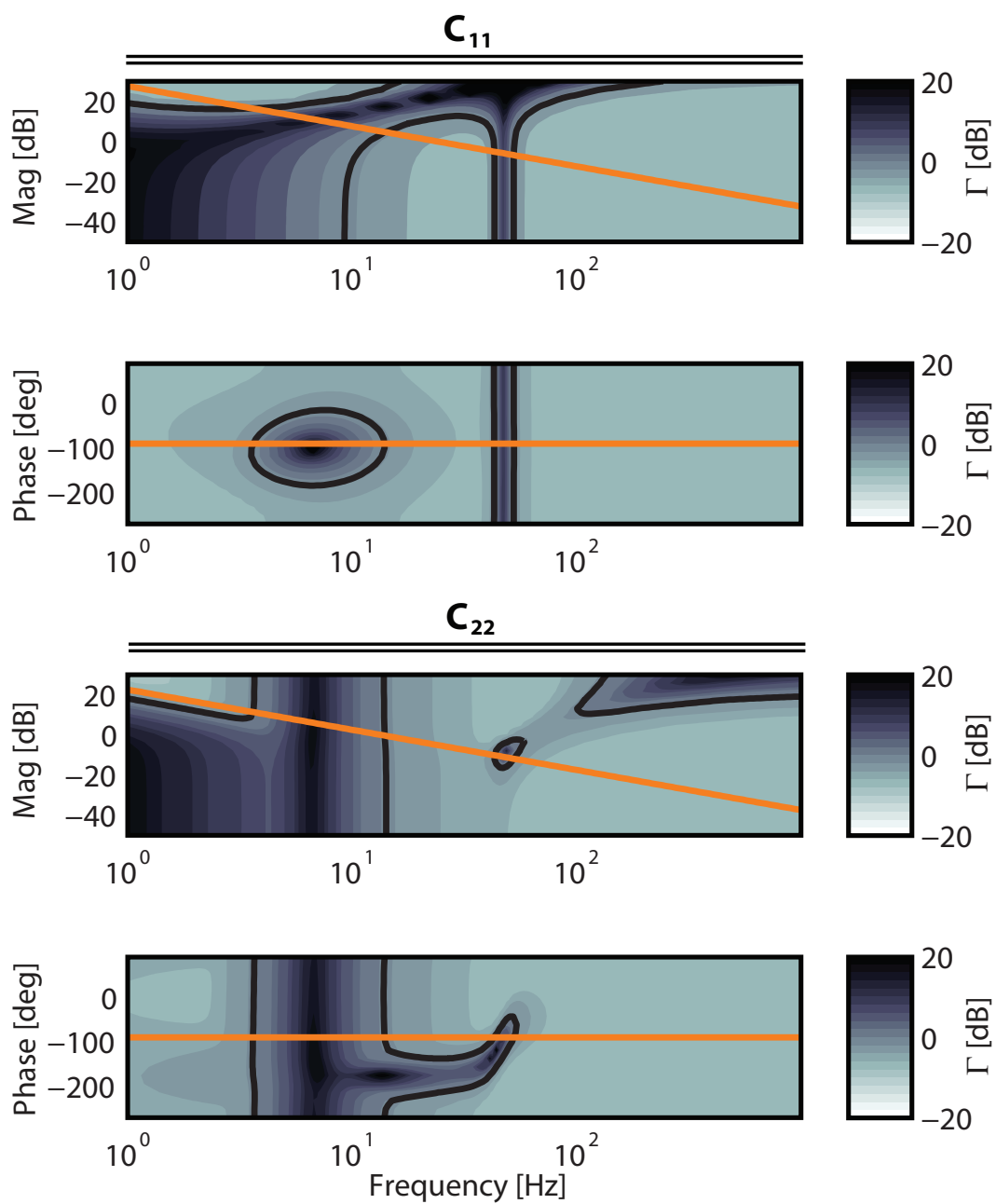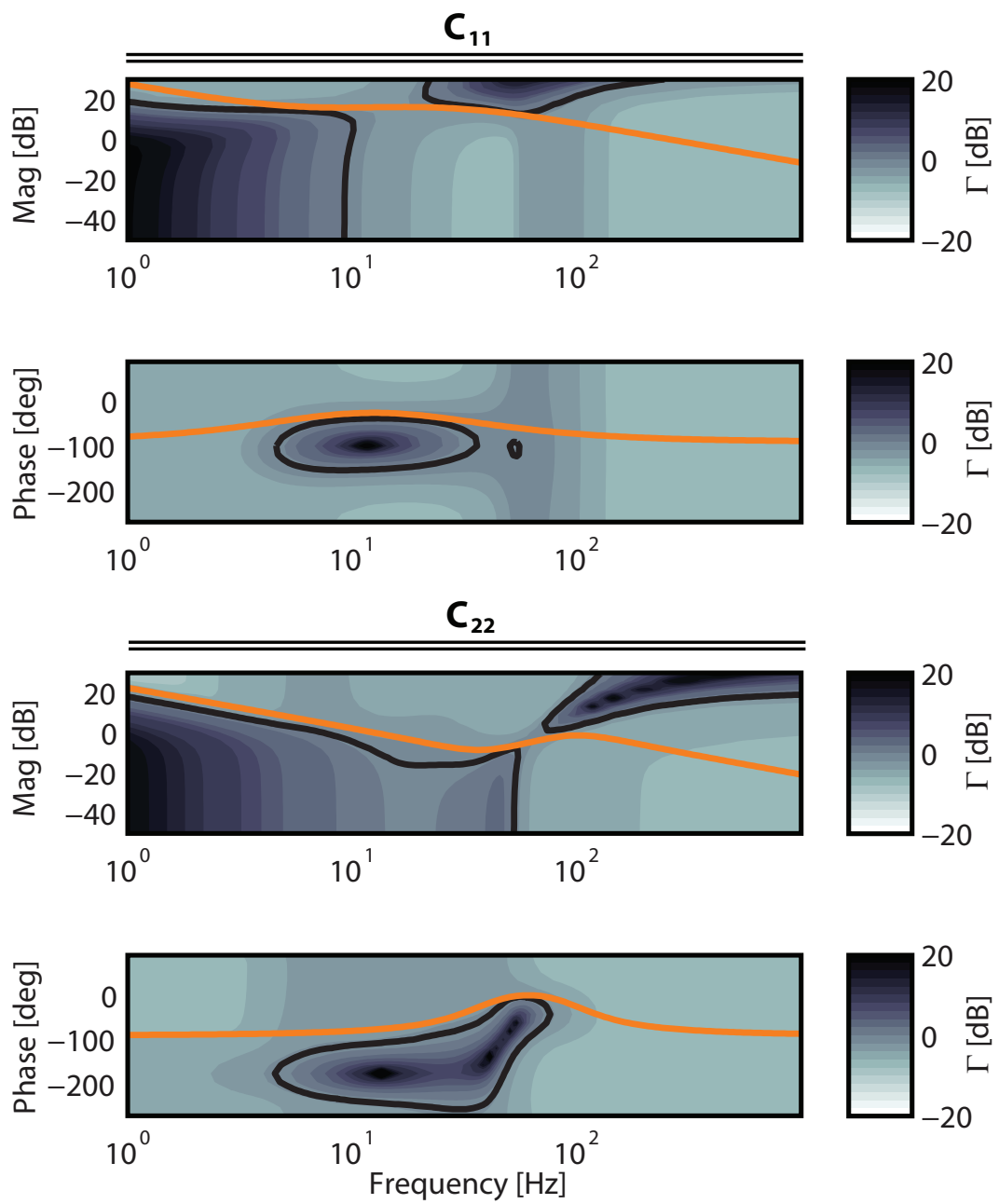
Figure 5.10: Controller Design Iteration 3: C_3

Figure 5.11: Controller Design Iteration 5 (Final): C_5

5.7 Comparison to Automated $\|H\|_\infty$ Synthesis

The details of the various H_∞ synthesis algorithms are covered extensively in the literature. The Glover-Doyle algorithm is of particular interest here since it is the default method in the MATLAB® function `hinfsyn` [42] used in this report. In this method, for a given $\gamma > 0$, a controller exists satisfying $\|\cdot\|_\infty < \gamma$ if and only if the unique stabilizing solutions to two algebraic Ricatti equations are positive definite and the spectral radius of their product is less than γ^2. An iterative bi-section technique is used to find the minimum such γ within some tolerance (therefore representing a sub-optimal solution). In the CRCBode approach, this minimization is performed approximately by the designer attempting to reach lower Γ contour levels.

The weights and plant used in this MIMO case study are modeled as realizable transfer function matrices, and so can be used directly with the H_∞ synthesis algorithm. To account for the structured uncertainty due to the parametric variations, we take the set of sampled plants used in the CRCBode design process and automatically fit a second order uncertainty weighting function matrix using the MATLAB function `ucover`, shown in Fig. 5.5. The manually designed controller, $K_{\mathrm{manual}} = D \cdot C_5$, (i.e. product of the ALIGN decoupling matrix and the CRCBode diagonal dynamic compensator) is shown with the automatically generated controller, K_{auto}, computed using the MATLAB function `hinfsyn` in Fig. 5.12.

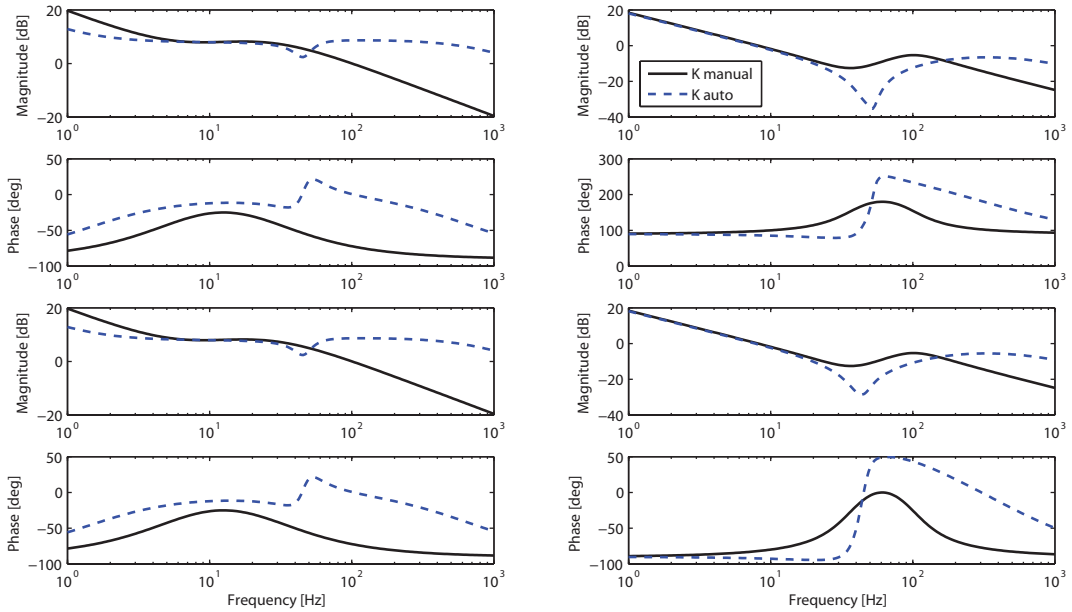
Figure 5.12: Frequency responses of manually designed and automatically synthesized controllers.

The sensitivity, $S = (I+GK)^{-1}$, and complementary sensitivity, $T = GK(I+GK)^{-1}$, transfer function matrices computed using the nominal plant model and both K_{manual} and K_{auto}, are shown in Fig. 5.13. Note that $S + T = I$, so only the diagonal entries exhibit the typical S T trade-off behavior.
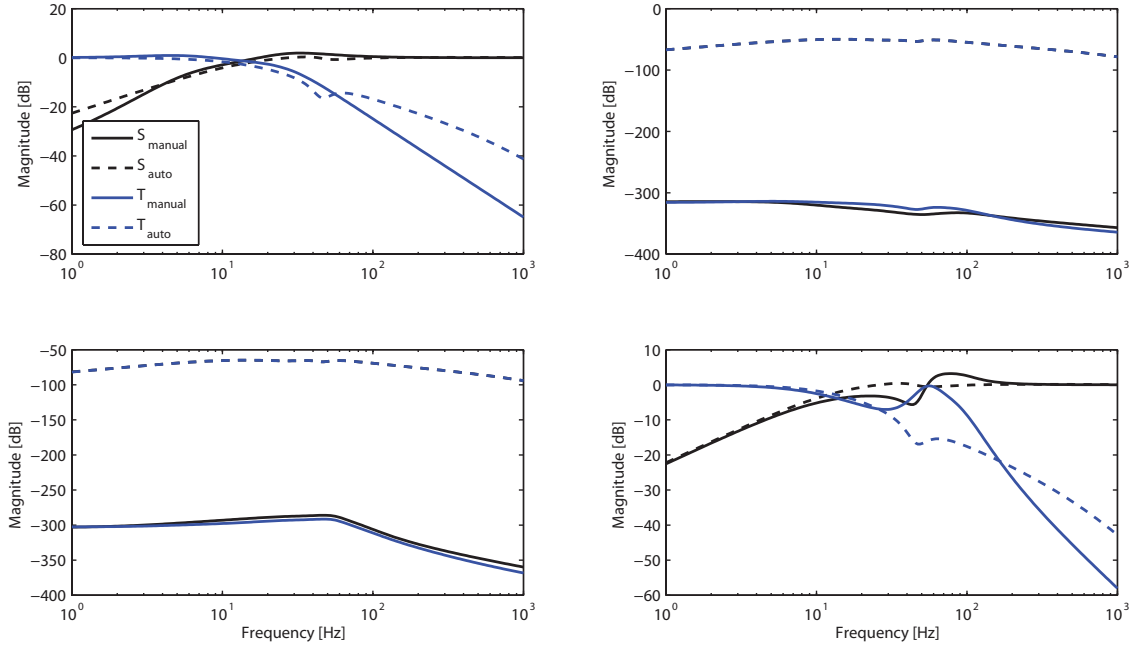

Figure 5.13: Sensitivity and complementary sensitivity functions for compensated systems.

Both methods achieve good closed-loop decoupling since the off-diagonal terms of both S and T are much less than unity; but the manual controller preforms significantly better in this respect. At low-frequencies, K_{manual} has greater gain and consequently S_{manual} is lower in magnitude, due to the free integrator, not present in K_{auto}, indicating that the manual controller should exhibit better reference tracking and disturbance rejection. Likewise, K_{manual} and therefore T_{manual} are approximately 20 dB lower in magnitude at high-frequencies, resulting in significantly better noise attenuation over K_{auto}. We examine these characteristics through simulation in the next section.

In the mid-frequency region near the 0 dB cross-over, both controllers utilize phase lead compensation to improve robust stability; however, K_{auto} does so in a more aggressive fashion requiring a higher-order controller and potentially increased control effort (note: we did not explicitly penalize this in the formulation of this problem). In particular order(K_{auto}) = 11 while order(K_{manual}) = 6. K_{auto} is consequently more complicated to both implement and analyze. Specifically, since the numerator and denominator coefficients of the automated controller include large floating point

values, the ratio is very sensitive to numerical computation errors. As a result, balanced order reduction was necessary before the following simulations could be performed.

5.7.1 Simulations

Fig. 5.14 shows the response of the tape drive velocity and tension outputs to step changes in the reference velocity and tension set-points. Both the nominal (thick) and sampled uncertain (thin) plants are shown. The tracking performance of both controllers in this case are very comparable with a slight advantage going to the automated controller which exhibits a shorter settling time and fewer oscillations. Both controllers are equally as effective at decoupling inputs and outputs, and though the off-diagonal sampled plants do show some large initial reaction, they very quickly settle to zero value in under 0.1 s. Fig. 5.15 shows the tape drive velocity and tension output response to band-limited white noise concentrated above 1kHz in both input channels. As predicted by the sensitivity functions in Fig. 5.13, K_{manual} exhibits a factor of 10 improvement in noise attenuation compared to K_{auto}.
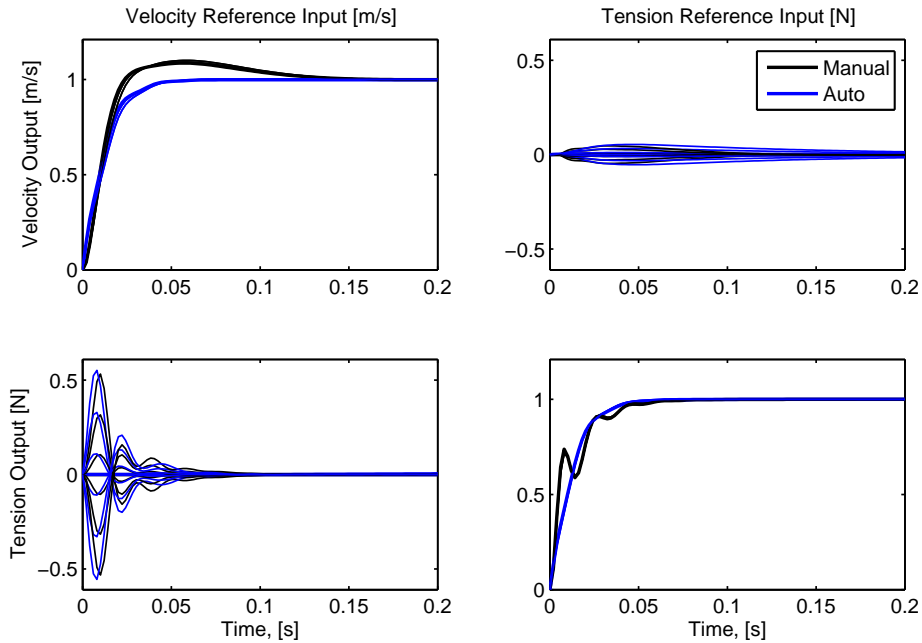

Figure 5.14: Tape velocity and tension output responses to reference input velocity and tension step change in set-points. Nominal plant shown as thick lines, and the sampled uncertain plants as thin with matching colors.
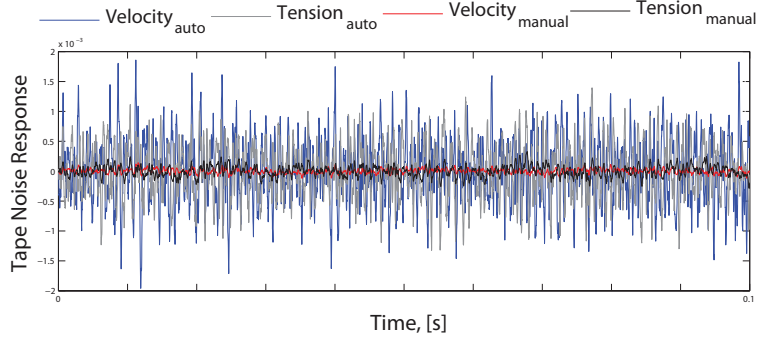
Figure 5.15: Tape velocity and tension output response to input band-limited white noise above 1kHz for systems compensated using K_{manual} and K_{auto}.

5.8   Conclusion

This chapter presented a new technique for manual MIMO frequency–domain robust controller design based on the so called Contoured Robust Controller (CRCBode) plots. First, a real valued approximate inverse to the MIMO transfer function was determined using the ALIGN algorithm in order to decouple the inputs and outputs of the system and facilitate the second loop-shaping step. In this step, individual dynamic compensators were designed for each input/output pair; however, unlike relatively ad-hoc methods such as sequential loop-closing, the effect of each dynamic element on the *overall system stability and performance* is immediately evaluated via the robust performance metric (a matrix norm). As demonstrated in the MIMO case study, changes in one diagonal compensator affect the forbidden regions in all other elements; thus once all forbidden regions are avoided in just the diagonal CRCBode plots, the entire MIMO closed-loop system will perform consistently with the problem specifications.

The CRCBode approach was shown to have certain advantages over standard automated $\|H\|_\infty$ controller synthesis algorithms. CRCBode plots naturally accommodate structured uncertainty, for instance, due to nonlinearities or parameter variations, whereas standard $\|H\|_\infty$ algorithms can only use unstructured uncertainty and consequently are less convenient and more conservative. The automated algorithms also require that the weighting functions and plant models be represented by realizable stable proper transfer functions, limiting achievable controller performance. The CRCBode method, however, can use either transfer function representations or discrete frequency response data, making it extremely useful practically. The designer can also impart other desirable properties to the controller such as pure integrators and higher roll-off directly.

The vast majority of control systems design is done using classical methods. These methods are relatively simple, visual and intuitive, and most of the time they work well. There is a strong argument to be made in favor of adapting these methods to reflect modern developments in the field of controls. We have shown already how basic loop–shaping design principles can be used on the CRCBode plots to design effective controllers for a MIMO, nonlinear, and time-varying system with both unstructured and structured uncertainty. Future work will focus on refining these methods, reducing the conservativeness of the robustness criteria, and extending the approach to more challenging cases, i.e. higher–order and unstable systems.

Bibliography

[1] K. Zhou, J. Doyle, K. Glover, *et al.*, *Robust and optimal control.* Prentice Hall Upper Saddle River, NJ, 1996, vol. 40.

[2] M. Green and D. Limebeer, *Linear robust control.* Prentice-Hall, Inc., 1994.

[3] O. H. Bosgra, H. Kwakernaak, and G. Meinsma, "Design methods for control systems," *Notes for a Course of the Dutch Institute of Systems and Control, Winter term*, vol. 2002, 2001.

[4] J. Doyle and G. Stein, "Multivariable feedback design: concepts for a classical/modern synthesis," *Automatic Control, IEEE Transactions on*, vol. 26, no. 1, pp. 4–16, 1981.

[5] D. McFarlane and K. Glover, "A loop-shaping design procedure using h synthesis," *Automatic Control, IEEE Transactions on*, vol. 37, no. 6, pp. 759–769, 1992.

[6] T. Atsumi and W. Messner, "Modified bode plots for head-positioning control in hard disk drives with structured and unstructured uncertainties," 2010, 13-15 Sep 2010, Boston, MA.

[7] ——, "Loop-shaping controller design with the rbode plot for hard disk drives," in *American Control Conference (ACC), 2010.* IEEE, 2010, pp. 2659–2664.

[8] H. Nyquist, "Regeneration theory," *Bell System Technical Journal*, vol. 11, no. 1, pp. 126–147, 1932.

[9] H. W. Bode, *Network analysis and feedback amplifier design.* van Nostrand New York, 1945, vol. 11.

[10] J. Maciejowski, "Multivariable feedback design," *Electronic Systems Engineering Series, Wokingham, England: Addison-Wesley,— c1989*, vol. 1, 1989.

[11] I. J. Conrr, "Guaranteed margins for lqg regulators," 1972.

[12] K. Zhou and J. C. Doyle, *Essentials of robust control.* Prentice hall Upper Saddle River, NJ, 1998, vol. 104.

[13] J. Doyle, K. Glover, P. Khargonekar, and B. Francis, "State-space solutions to standard h2 and h control problems," *Automatic Control, IEEE Transactions on*, vol. 34, no. 8, pp. 831–847, 1989.

[14] T. Iwasaki and R. E. Skelton, "All controllers for the general h¡ sub¿¡/sub¿ control problem: Lmi existence conditions and state space formulas," *Automatica*, vol. 30, no. 8, pp. 1307–1317, 1994.

[15] P. Gahinet and P. Apkarian, "A linear matrix inequality approach to h control," *International journal of robust and nonlinear control*, vol. 4, no. 4, pp. 421–448, 1994.

[16] I. Horowitz, "Survey of quantitative feedback theory (qft)," *International journal of robust and nonlinear control*, vol. 11, no. 10, pp. 887–921, 2001.

[17] J. Doyle, B. Francis, and A. Tannenbaum, *Feedback control theory.* Macmillan New York, 1992, vol. 134.

[18] S. Skogestad and I. Postlethwaite, "Multivariable feedback control: analysis and design," *New York*, 1996.

[19] R. D. Braatz, "Robust loopshaping for process control," Ph.D. dissertation, California Institute of Technology, 1993.

[20] P. Feyel, *Loop-shaping Robust Control.* John Wiley & Sons, 2013.

[21] D. Leith and W. Leithead, "Survey of gain-scheduling analysis and design," *International Journal of Control*, vol. 73, no. 11, pp. 1001–1025, 2000.

[22] J. Taylor and W. Messner, "Controller design for nonlinear systems using the robust controller bode (rcbode) plot," in *American Control Conference (ACC), 2011.* IEEE, 2011, pp. 1414–1419.

[23] J. Taylor, I. Gentilini, and W. Messner, "Loop-shaping controller design for nonlinear systems using the contoured robust controller bode (crcbode) plot," in *American Control Conference (ACC), 2012.* IEEE, 2012.

[24] J. Taylor and W. Messner, "Controller design for nonlinear systems using the contoured robust controller bode plot," *International Journal of Robust and Nonlinear Control*, 2013.

[25] T. Sarpkaya, "Torque and cavitation characteristics of butterfly valves," *Journal of Applied Mechanics*, vol. 28, p. 511, 1961.

[26] J. Park and M. Chung, "Study on hydrodynamic torque of a butterfly valve," *Journal of fluids engineering*, vol. 128, p. 190, 2006.

[27] J. Taylor, B. Sinopoli, and W. Messner, "Nonlinear modeling of butterfly valves and flow rate control using the circle criterion bode plot," in *American Control Conference (ACC), 2010*. IEEE, 2010, pp. 1967–1972.

[28] W. Messner, "Formulas for asymmetric lead and lag compensators," in *American Control Conference, 2009. ACC'09*. IEEE, 2009, pp. 3769–3774.

[29] D. McFarlane and K. Glover, *Robust Controller Design Using Normalized Coprime Factor Plant Descriptions*, ser. Lecture Notes in Control and Information Sciences, M. Thoma and A. Wyner, Eds. Springer Verlag, 1989, vol. 138.

[30] J. Doyle, "Analysis of feedback systems with structured uncertainties," in *IEE Proceedings D (Control Theory and Applications)*, vol. 129, no. 6. IET, 1982, pp. 242–250.

[31] M. Verma and E. Jonckheere, "L compensation with mixed sensitivity as a broadband matching problem," *Systems & control letters*, vol. 4, no. 3, pp. 125–129, 1984.

[32] E. R. Westervelt, J. W. Grizzle, C. Chevallereau, J. H. Choi, and B. Morris, *Feedback control of dynamic bipedal robot locomotion*. Citeseer, 2007.

[33] J. Taylor and W. Messner, "Loop-shaping for non-minimum phase systems using contoured robust controller bode plots," in *American Control Conference (ACC), 2014*. IEEE, 2014.

[34] K. Ogata and Y. Yang, "Modern control engineering," 1970.

[35] K. J. Aström and R. M. Murray, *Feedback systems: an introduction for scientists and engineers*. Princeton university press, 2010.

[36] J. K. Roberge, "The mechanical seal," Ph.D. dissertation, Massachusetts Institute of Technology., 1960.

[37] H. Kwakernaak and R. Sivan, *Linear optimal control systems.* Wiley-interscience New York, 1972, vol. 1.

[38] G. F. Franklin, M. L. Workman, and D. Powell, *Digital control of dynamic systems.* Addison-Wesley Longman Publishing Co., Inc., 1997.

[39] J. Taylor and W. Messner, "Controller design for nonlinear multi-input/multi-output systems using the contoured robust controller bode plot," in *American Society of Mechanical Engineers Dynamic Systems and Controls Conference (ASME DSCC), 2014.* IEEE, 2013.

[40] A. Packard and J. Doyle, "The complex structured singular value," *Automatica*, vol. 29, no. 1, pp. 71–109, 1993.

[41] J. Edmunds and B. Kouvaritakis, "Extensions of the frame alignment technique and their use in the characteristic locus design method," *International Journal of Control*, vol. 29, no. 5, pp. 787–796, 1979.

[42] G. Balas, R. Chiang, A. Packard, and M. Safonov, *Robust Control Toolbox®: User's Guide.* MathWorks, Incorporated, 2012.